Atmospheric Chemistry and Transport Modeling in the Outer Solar System

Thesis by
Yuan-Tai Lee
(Anthony Lee)

In Partial Fulfillment of the Requirements
For the Degree of
Doctor of Philosophy

California Institute of Technology
Pasadena, California

2001

(Defended August 9, 2000)

Dedicated to my parents, Sheng-hui, and Eric.

Acknowledgments

I must thank to my parents, especially my father, first and foremost. After my mother passed away 15 years ago, You always encouraged me to pursue my education even when I chose a field that have appeared so odd, and not a making-big-money-in-the-future career. I am grateful to your confidence in me, and your support, economically and emotionally. Thanks for all the science books that you bought for me when the Taiwan community was just surviving from against hungry and war, and for instilling in me a love of learning. You spared no effort to provide me with the best education possible, and for that I am eternally grateful.

To Dr. Typhoon Lee of the institute of earth sciences at Academia Sinica of Republic of China, who guided and supported me for the interest of astronomy, and the historically first master degree thesis in astrophysics in the department of physics of National Taiwan University. Thanks for hiring me as your assistant in the year when I retired from military service, providing me opportunities to improve my English, and introducing me to Caltech by your strong recommendation.

Yuk Yung has supported me for many years at Caltech and inspired me with his wisdom, enthusiasm, generosity, and genuine love of science. Thank you for introducing me to the delights of planetary atmospheres, and patiently correcting my English writing. I would never forget your "personal" classes in Taiwan about the big picture of Solar System, and all your enthusiastic philosophical discussions at Caltech about the differences between eastern and western culture. From you, I have found a perfect combination of the traditional Chinese spirit and the scientific creativeness and

efficiency.

Mark Allen has been a great help in these years and his push of the PH_3 and 2D projects has been much appreciated. I thank him for guiding me through the photochemical kinetics program, and many of the useful discussions. His excellent organizational skills and logical steps toward the correct direction of the project have served as a wonderful example for me.

I have benefited from numerous scientific discussions with Andy Ingersoll, Dave Stevenson, Jeff Blake, and also the academic advisory from Bruce Murray. Their insight and experience have been a valuable resource for me. Honestly, talking to these great scientists becomes the honor in my life. I would like to thank all the planetary science faculties for being roles in science and for caring about the well being of the graduate students.

There are many thanks going to JPL. Glenn Orton, Jim Friedson, Gene Serabyn, Bob West, they all helped me considerably for my thesis and papers. Those discussions in the emails or in the greeting room of JPL were appreciated for bringing me many thoughts and new ideas. I especially appreciate Glenn Orton's generosity in plotting synthetic spectra for me again and again.

At Caltech, there are also many thanks to go around. Yibo Jiang, Wojer Lee, and XiaoDong Song helped me to overcome the unawareness stage when I just came to United States. I especially appreciate those discussions about computer and programming technology with Yibo (Congratulations for your new-born son!). Josh Chang and Gabe Morgan helped me to build up all the photochemical models, showed me details inside

the "black box", and upgraded the KINETICS version. Mimi Gerstell and Julianne Moses have corrected my English writing for several times, and provided me useful criticism in science. Zhiming Kuang was the best "neighbor" in the same office. Thanks for all the great discussions, scientific and otherwise. Michael Black advised me the networking issues, and the administrative staff of the planetary science department kept things running smoothly.

Finally, I must express my gratitude to my wife Sheng-hui. She gave up her teaching career in Taiwan and came to a country without any relative or friend, just for a simple reason to be together with her husband. With great love and affection, I dedicate this thesis to her to whom I owe more than I can express. Thanks for giving my life meaning, Sheng-hui, and for the best gifts you brought to me: Eric and his upcoming sister Karen. Everything you did for me fulfilled my heart and delighted my life. Eric, after you grow up and can understand these words, I hope you know how much father loves you.

致謝

(Acknowledgments in Chinese)

將青春的精華時光投入在加州理工學院這個世界有名的學術殿堂，讓自己有機會浸潤在自然科學的浩瀚領域中，該是人生中難得的機緣吧。完成的本身，不但帶有喜悅，帶有回憶，也是一種極其深刻的惕勵。八年前隻身來到美國，雖然無法預知這個過程將有的曲折與磨練，只爲了圓一個孩提時代的夢想，然而這來時路之刻骨銘心，我將永生難忘。在美國完成的這篇英文博士論文，特地附上一篇短短的中文，希望向所有曾經關心我、幫助我的人，致上深深的謝意。

完成博士學位，首先要感謝的，當然是我的家人，特別是我的父親。在母親過世之後，他撐起了家庭的全部，不但鼓勵我出國深造，在經濟上的支援，還有精神上的鼓勵，成爲支持我完成全部過程的原動力。爸，李家終於有了一個博士，希望我沒有讓您失望。

感謝我前後兩位影響我至爲深遠的恩師，中央研究院的李太楓所長，以及加州理工學院的翁玉林教授。我想，除了授業解惑之外，我從他們兩位身上，真正體驗到做學問的精神與執著。無論是在台灣的中研院地球科學所作碩士論文研究，或是在加州理工學院作博士論文研究，真正使我受益的，其實不在學術研究的本身，而是科學的實證態度與邏輯方法。如果說「師者，所以傳道授業解惑也」，我想這兩位科學家都是可以當之無愧的。

另外，加州理工學院的師長和同學們，他們給予我的指導、幫助，或是無形中的身教典範，都是值得我感念的。特別值得一提的是陳惠陽博士，當初如果不是他的介紹，我可能也不會有機會來到南加州，它是一個非常好的朋友。還有此地的中國同學們，特別是李沃哲、姜一波、宋小東、匡志明等幾位，都是熱心而有才華的中國人，能夠跟他們成爲朋友，有緣分一起相處，實在是我莫大的榮幸。

最後，我要將這篇論文的完成，與我同甘共苦的賢內助一起分享，勝慧，這些年來真是委屈你了，我知道你爲了我，甘願放棄自己喜愛的教學事業，和親愛的家人們，隨我來到美國，而在生下小 B 和即將到來的小妹妹的過程中，又嚐盡辛苦。這些我都知道，也因爲如此，更使我體會到這一切得來的不容易。這個學位應該是我們共同得到的。

Abstract

This thesis consists of 1-D and 2-D photochemical-dynamical modeling in the upper atmospheres of outer planets. For 1-D modeling, a unified hydrocarbon photochemical model has been studied in Jupiter, Saturn, Uranus, Neptune, and Titan, by comparing with the Voyager observations, and the recent measurements of methyl radicals by ISO in Saturn and Neptune. The CH_3 observation implies a kinetically sensitive test to the measured and estimated hydrocarbon rate constants at low temperatures. We identify the key reactions that control the concentrations of CH_3 in the model, such as the three-body recombination reaction, $CH_3 + CH_3 + M \rightarrow C_2H_6 + M$, and the recycling reaction $H + CH_3 + M \rightarrow CH_4 + M$. The results show reasonable agreement with ISO values. In Chapter 4, the detection of PH_3 in the lower stratosphere and upper troposphere of Jupiter has provided a photochemical-dynamical coupling model to derive the eddy diffusion coefficient in the upper troposphere of Jupiter. Using a two-layers photochemical model with updated photodissociation cross-sections and chemical rate constants for NH_3 and PH_3, we find that the upper tropospheric eddy diffusion coefficient $< 10^5$ cm^2 sec^{-1}, and the deeper tropospheric value $> 10^6$ cm^2 sec^{-1}, are required to match the derived PH_3 vertical profile by the observation. The best-fit functional form derivation of eddy diffusion coefficient in the upper troposphere of Jupiter above 400 mbar is $K = 2.0 \times 10^4 (n/2.2 \times 10^{19})^{-0.5}$ cm^2 sec^{-1}. On the other hand, Chapter 5 demonstrates a dynamical-only 2-D model of C_2H_6 providing a complete test for the current 2-D transport models in Jovian lower stratosphere and upper troposphere (270 to 0.1 mbar pressure levels). Different combinations of residual advection, horizontal eddy dispersion, and vertical eddy mixing are examined at different latitudes.

Table of Contents

List of Figures

List of Tables

Chapter 3:

Chapter 4:

Chapter 5:

Chapter 1

Introduction

Photochemistry plays a central role in the determination of the physical and chemical state of the planetary upper atmospheres. Absorption of solar radiation and photodissociation of atmospheric gases into their constituent molecules, radicals, and atoms, followed by subsequent chemical reactions between the photolysis products and other atmospheric molecules control the composition of the "visible" portion of planetary atmospheres. The chemical composition in turn affects many physical aspects of the atmosphere such as its thermal structure, radiation balance, dynamical processes, ionospheric structure, and the formation of clouds and hazes.

During the past decades, modeling photochemistry in the planetary atmospheres, including all the prominent atmospheres such as Earth, Mars, Venus, and outer solar system planets and satellites, has increased our understanding of the chemical and physical processes within the solar system. This thesis will focus on the atmospheres of giant planets, especially that of Jupiter. Jupiter is the largest planet in our solar system, and it is also the most observed object in the outer solar system. This thesis concentrates on the photochemistry and the chemical-dynamical coupling studies in the "visible" part of the atmosphere of Jupiter by using one-dimensional and two-dimensional models. Other outer solar system atmospheres, including those of Saturn, Uranus, Neptune, and

Titan, will be discussed in chapter 3.

This thesis can be roughly divided into two parts: 1-D and 2-D modeling. Chapters 2 to 4 describe the one-dimensional modeling work, which includes both chemical processes and eddy transport. Chapter 5 presents a two-dimensional model of the lower stratosphere of Jupiter with only dynamical processes, which may form the basis of the future coupled chemical and dynamical 2-D model. In Chapter 2, I introduce and review the one-dimensional Caltech/JPL photochemical model, which has been developed for more than 20 years by previous workers. I briefly summarize the basic theory behind the model, and the numerical method for this complex computational system.

Chapter 3 is on the research of the crucial role of the chemical species CH_3 in the hydrocarbon chemistry of the atmospheres of the outer solar system: Jupiter, Saturn, Uranus, Neptune, and Titan. The paper was published in JGR by Lee, Yung, and Moses [2000]. Recent measurements of methyl radicals (CH_3) in the upper atmospheres of Saturn and Neptune by the Infrared Space Observatory (ISO) provide new constraints to photochemical models of hydrocarbon chemistry in these planets. The derived column abundances of CH_3 on Saturn above 10 mbar and Neptune above the 0.2 mbar pressure level are $(2.5 - 6.0) \times 10^{13}$ cm^{-2} and $(0.7 - 2.8) \times 10^{13}$ cm^{-2}, respectively. We use the updated Caltech/JPL photochemical model, which incorporates hydrocarbon photochemistry, vertical molecular and bulk atmospheric eddy diffusion, and realistic radiative transfer modeling, to study the CH_3 abundances in the upper atmosphere of the giant planets and Titan. We identify the key reactions that control the concentrations of CH_3 in the model, such as the three-body recombination reaction, $CH_3 + CH_3 + M \rightarrow C_2H_6 + M$. We evaluate and extrapolate the three-body rate constant of this reaction to

lower-temperatures ($1.8 \times 10^{-16}\ T^{-3.75}\ e^{-300/T}$, $T < 300$ K) and compare methyl radical abundances in five atmospheres: Jupiter, Saturn, Uranus, Neptune, and Titan. The sensitivity of our models to the rate coefficients for the reactions $H + CH_3 + M \rightarrow CH_4 + M$, $H + C_2H_3 \rightarrow C_2H_2 + H_2$, $^1CH_2 + H_2 \rightarrow CH_3 + H$, and $H + C_2H_5 \rightarrow 2\ CH_3$, the branching ratios of CH_4 photolysis, vertical mixing in the five atmospheres, and Lyman α photon enhancement at the orbit of Neptune have all been tested. The results of our model CH_3 abundances for both Saturn (5.1×10^{13} cm^{-2}) and Neptune (2.2×10^{13} cm^{-2}) show good agreement with ISO Short Wavelength Spectrometer measurements. Using the same chemical reaction set, our calculations also successfully generate vertical profiles of stable hydrocarbons consistent with Voyager and ground-based measurements in these outer solar system atmospheres. Predictions of CH_3 column concentrations (for $p \leq 0.2$ mbar) in the atmospheres of Jupiter (3.3×10^{13} cm^{-2}), Uranus (2.5×10^{12} cm^{-2}), and Titan (1.9×10^{15} cm^{-2}) may be checked by future observations.

Chapter 4 presents another project for determining the strength of the 1-D bulk atmospheric vertical motion in the troposphere of Jupiter by modeling PH_3. I briefly summarize the first detection of a rotational transition of PH_3 (phosphine) on Jupiter. Using a Fourier transform submillimeter spectrometer, Weisstein and Serabyn detected the J=3-2 transition of PH_3 at 800.5 GHz. This deep (~ 20%) absorption line is strongly pressure-broadened, with a FWHM of 9.6 GHz. The lineshape of this transition is quite sensitive to the distribution of PH_3 in the upper troposphere. Allen and I then took over the data analysis and modeling works. Using a radiative transfer model that constrains the PH_3 vertical profile to approach a constant mixing ratio in the "deep" ($p \geq 600$ mbar) atmosphere, we derive a PH_3 mixing ratio which falls off with increasing height, but the

slope of the PH_3 falloff in the upper troposphere is steeper than that inferred from both infrared measurements and previous photochemical models. Using a simple 2-layer photochemical model with updated photodissociation cross-sections and chemical rate constants for PH_3, we find that an upper tropospheric eddy diffusion coefficient (K_h) less than 10^5 cm^2 sec^{-1} and a deeper tropospheric value (K_l) larger than 10^6 cm^2 sec^{-1}, are required to match the PH_3 vertical profile derived from the observation. This model includes detailed treatments of the radiation attenuation by Rayleigh scattering and dust/cloud scattering, as well as ammonia condensation effect. The expression for our best-fit derivation for the eddy diffusion coefficient in the upper troposphere above 400 mbar is $K = 2.0 \times 10^4 (n/2.2 \times 10^{19})^{-0.5}$ cm^2 sec^{-1}. NH_3 vertical profiles were thought to be a possible tracer for characterizing 1-D motion in the Jovian troposphere. Since the NH_3 vertical distribution in the upper troposphere of Jupiter might fall on its saturated vapor-pressure line, however, modeling NH_3 does not provide reliable upper-limits for eddy diffusion coefficients. Therefore, we suggest that PH_3 modeling is a better tracer for determining dynamical motions in the upper tropospheric layer below the tropopause but above the cloud tops on Jupiter. We also interpret the transition level between the two dynamical regimes (at levels above the line, K is ~ 10^4 cm^2 sec^{-1}; at levels below the line, K is > 10^6 cm^2 sec^{-1}) as the Jovian radiative-convective boundary in its upper troposphere.

Two-dimensional modeling in the lower stratosphere and upper troposphere (from 0.1 mbar to 270 mbar pressure level) will be presented in chapter 5. This chapter describes the first-stages of work that will ultimately lead to a complete meridional and vertical photochemical-dynamical modeling on Jupiter. Therefore, this project only studies the dynamical motion of the atmosphere without considering chemical effects. We

adopt C_2H_6 as the tracer and develop a two-dimensional dynamical model to calculate its vertical and meridional distribution in the atmospheric range described above. Choosing C_2H_6 as the tracer takes advantage of the latitudinal observations of C_2H_6 by Orton *et al.* [1989], and the fact that it is one of the more stable hydrocarbons in the lower stratosphere. Our dynamical model is based on the 2-D circulation models introduced by West *et al.* [1992] and Friedson *et al.* [1999]. Principal parameters of our model, such as the residual circulation stream function and the large-scale horizontal eddy diffusion coefficient, are derived from their models. There are four major dynamical processes adopted in the model, stream function, horizontal eddy diffusion coefficient, vertical diffusion coefficient, and boundary downward flux. We explore different combinations of the parameters, which are not well constrained in the previous 2-D models of Jupiter. The derived C_2H_6 profiles are then input to the radiative transfer computation, and compared with Orton *et al.*'s infrared observations [1989]. The results suggest that the current 2-D models must consider the influence of vertical eddy diffusion, and that the residual circulation and horizontal eddy diffusions derived by West *et al.* [1992] and Friedson *et al.* [1999] may be too large. The results also provide possible constraints to the downward flux of C_2H_6 from the upper atmosphere at high latitudes. The amount of downward flux may be important for the on-going or future studies of the photochemistry and aerosol chemistry at polar or high latitude regions on Jupiter.

All these works are not only successful in creating a more consistent hydrocarbon, ammonia, and phosphine photochemical model on Jupiter and outer planets, but also increase our understanding of the dynamical motion in the lower stratosphere and upper troposphere of Jupiter. The unified hydrocarbon photochemical model (Chapter 3) for

five outer solar system atmospheres provides future modelers with complete and confident hydrocarbon kinetics. The model also gives chemical kinetics experiments at low temperatures a strong constraint. On the other hand, determination of the vertical eddy diffusion coefficient at levels as low as the troposphere on Jupiter (Chapter 4), and the quantitative investigation for the two-dimensional dynamical processes in the lower stratosphere of Jupiter (Chapter 5), develops a basis for the reliable 1-D and 2-D atmospheric dynamical models of Jupiter.

Chapter 2

One-Dimensional Photochemical Model

2.1. Continuity equation

Studies of photochemistry in the reducing atmospheres of the outer solar system were pioneered by *Strobel* [1973, 1975], who provided the basis for subsequent modeling. In principle, most of the numerical models try to find the steady solution of the continuity equation

$$\frac{\partial n_i}{\partial t} + \vec{\nabla} \cdot \phi_i = P_i - L_i \tag{2.1}$$

where n_i (cm^{-3}) is the number density, ϕ_i (cm^{-2} s^{-1}) is the flux, P_i (cm^{-3} s^{-1}) is the production rate, and L_i (cm^{-3} s^{-1}) is the loss rate, of the species i. The flux $\phi_i = n_i \upsilon_i$ represents transport of air masses between different parts of the atmosphere (υ_i is the atmospheric transport velocity). In the one-dimensional dynamical model, mass transport is simplified to the vertical (z-axis) diffusive processes

$$\phi_i = -D_i\left(\frac{\partial n_i}{\partial z} + \frac{n_i}{H_i} + \frac{1+\alpha_i}{T}\frac{\partial T}{\partial z}n\right) - K\left(\frac{\partial n_i}{\partial z} + \frac{n_i}{H_a} + \frac{1}{T}\frac{\partial T}{\partial z}n\right) \tag{2.2}$$

where D_i is the molecular diffusion coefficient for each constituent i, T is the temperature, n is the bulk atmospheric density, α_i is the thermal diffusivity factor, H_i and H_a are the average scale height of species i and the bulk scale height of the ambient atmosphere,

respectively. K is the eddy diffusion coefficient, which empirically parameterizes all kinds of motions of the bulk atmosphere. Both D_i and K have units of $cm^2\ s^{-1}$. The values of the eddy diffusion coefficient K used in one-dimensional photochemical models are usually determined from atmospheric observations. In the upper atmosphere where $D_i > K$, the constituents are diffusively separated according to their scale heights H_i. On the other hand, in the lower atmosphere where $D_i < K$, the atmosphere is homogeneously mixed. The atmospheric level where $D_i = K$ is known as the homopause.

In the one-dimensional model, the equation of continuity (2.1) becomes

$$\frac{\partial n_i}{\partial t} + \frac{\partial \phi_i}{\partial z} = P_i - L_i \tag{2.3}$$

where all quantities n_i, ϕ_i, P_i, and L_i, are evaluated at an altitude z and time t. The non-linear terms P_i and L_i are evaluated using chemical kinetics. The analytical steady-state solution of the one-dimensional continuity equation is possible if these non-linear terms can be ignored, i.e. $P_i - L_i = 0$. In accordance with steady state $\frac{\partial n_i}{\partial t} = 0$, equation (2.3) becomes a first-order differential equation

$$\frac{d\phi_i}{dz} = 0. \tag{2.4}$$

The continuity equation thus deals only with the dynamical part of the atmosphere. In the lower atmosphere below the homopause and ignoring the thermal gradient terms, the flux expression (2.2) is simplified by

$$\phi_i(z) = -K(z)[\frac{dn_i}{dz} + \frac{n_i}{H_a}] \tag{2.5}$$

Two analytical solutions of equation (2.4) and (2.5) will be demonstrated in the following

two sections.

2.1.1. Case 1 – Constant eddy diffusion coefficient $K(z) = K_0$

From equation (2.4), we define a constant flux $\phi(z) = \phi_0$ at all altitudes, so that equation (2.5) becomes

$$\phi_i(z) = -K_0[\frac{dn_i}{dz} + \frac{n_i}{H_a}] = \phi_0 . \tag{2.6}$$

Solving the first-order differential equation (2.6) derives the vertical number density profile $n_i(z)$

$$n_i(z) = Ce^{-\frac{z}{H_a}} - \frac{\phi_0}{K_0(\frac{1}{H_a})}$$

$$= Ce^{-\frac{z}{H_a}} - \frac{\phi_0 H_a}{K_0} \tag{2.7}$$

C is an arbitrary constant for the solution of the differential equation. It is convenient to define a dimensionless quantity, the mixing ratio of species i

$$x_i \equiv \frac{n_i}{\sum_i n_i} = \frac{n_i}{n_a} . \tag{2.8}$$

Assume that $x_i(0)$ and n_0 are the mixing ratios of species i, and bulk number density, at $z = 0$, respectively. The analytical solution of the vertical mixing ratio profile $x_i(z)$ is thus given by

$$x_i(z) = x_i(0) + \frac{\phi_0 H_a}{n_0 K_0}[1 - e^{\frac{z}{H_a}}]. \tag{2.9}$$

This solution provides the vertical mixing ratio curve for an "inert" species (like He) in the lower atmosphere with constant eddy diffusivity at all levels. A sample case with the constant eddy diffusion coefficient is shown in Figure 2-1. This case simulates the C_2H_6 mixing ratio profile in the lower stratosphere of Jupiter, by providing a constant eddy diffusion coefficient $K_0 = 10^4$ cm^2 sec^{-1}, and a constant downward flux $\phi_0 = -10^9$ cm^{-2} sec^{-1} (the negative flux denotes downward motion).

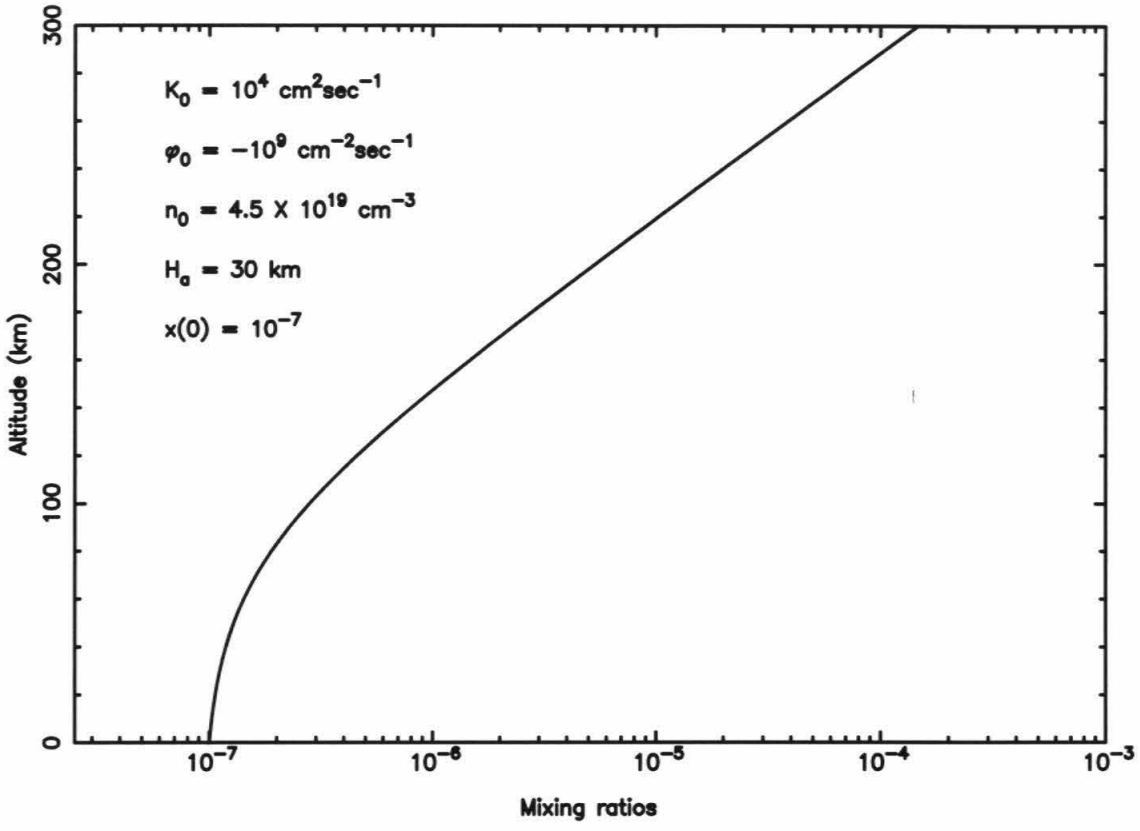

Figure 2-1. The sample case for a constant eddy diffusion coefficient with altitude (K = 10^4 cm^2 sec^{-1}). All parameters applied to equation (2.9) are shown in the upper-left corner of the plot.

2.1.2. Case 2 – Altitude-dependent eddy diffusion coefficient $K(z) = K_0 \exp(z/H_k)$

In this case, the vertical distribution of eddy diffusion coefficients is assumed to increase as the altitude increases. Solving this differential equation as in equation (2.7), we may derive a similar solution of the number density $n_i(z)$, which is represented as a mixing ratio $x_i(z)$.

$$x_i(z) = x_0 + \frac{\phi_0}{n_0 K_0 (\frac{1}{H_a} - \frac{1}{H_k})} [1 - e^{z(\frac{1}{H_a} - \frac{1}{H_k})}] \ . \qquad (2.10)$$

Figure 2-2 shows the sample case for this solution. All values are as the same as for Figure 2-1, except that the constant eddy diffusion coefficient K_0 is replaced by an altitude-dependent eddy diffusion coefficient $K_0 \exp(z/H_k)$, where H_k = 50 km. Note that the eddy diffusion coefficient increases at high altitudes, and this results in low mixing ratios when compared with Figure 2-1.

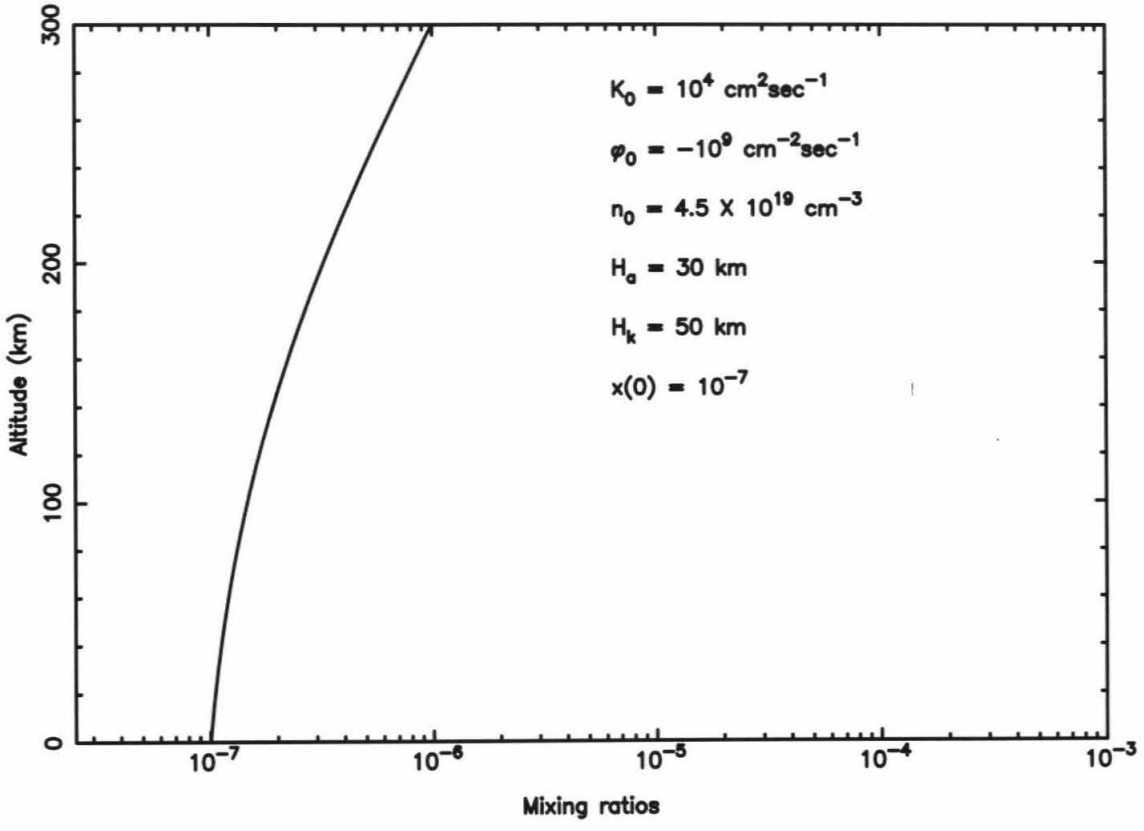

Figure 2-2. The sample case for eddy diffusion coefficient increasing with altitude ($K = 10^4 \exp(z/H_k)$ cm^2 sec^{-1}). All parameters used in equation (2.10) are shown in the upper-right corner of the plot.

2.2. Numeric modeling

The analytical solutions for the one-dimensional continuity equation (2.3) are only applicable to the "pure-dynamical" atmosphere. Considering equation (2.3) with the nonlinear photochemistry terms P_i and L_i, we may derive the steady state solutions ($\frac{\partial n_i}{\partial t} = 0$) by using numerical calculations. The Caltech/JPL photochemical kinetics and diffusion code has been developed to solve the coupled one-dimensional continuity equations as a function of time and altitude [Allen *et al.* 1981; Yung *et al.* 1984]. This program allows the solutions to the coupled continuity equations, and considers diurnally averaged quantities for the flux and the production and loss terms. Both eddy and molecular diffusion are considered in the transport term.

For a typical photochemical model in the atmospheres of the solar system, the continuity equations are solved using finite-difference techniques with appropriate vertical resolution. Newton's method is used to solve nonlinear chemistry. Calculations are performed until successive iterations differ by no more than 0.1%, or other threshold values, for every varying species. A converged process requires the final time step t be at least 10^{15} seconds.

The numerical calculation of a typical 1-D photochemical model needs some inputs that as described in the following.

2.2.1. Background atmospheric structure

The first step in developing a photochemical model for a planetary atmosphere is to generate a hydrostatic-equilibrium background model atmosphere that accurately depicts the density and temperature variations with altitude. The background model atmosphere should consider the temperature profile, planetary shape, rotation rate (including wind speeds), gravitational field, and variation of mean molecular mass with altitude.

2.2.2. Solar flux

The solar flux values adopted in our solar system models were compiled from a variety of sources. To provide general predictions concerning atmospheric chemistry, we use values that are typical of average conditions during the solar cycle. The fluxes were binned in 20-Å intervals at wavelength below 1225 Å, 50-Å intervals between 1225 and 4025 Å, and 100- Å intervals at wavelengths longer than 4025 Å. From 50 to 1050 Å extreme ultraviolet (EUV), the flux was taken from the solar minimum (July 1976) values of Torr and Torr [1985]; from 1050 to 1200 Å mid-ultraviolet, we adopt the Mount and Rottman [1981] for the standard model; and from 1200 to 3050 Å, we use flux values from the 12 May 1983 measurements of the Solar Mesospheric Explorer satellite [R. T. Clancy, personal communication to M. Allen, 1989]. Beyond 3050 Å, we use values compiled by the World Meteorological Organization (WMO 1985). The solar H Ly-α line at 1216 Å is responsible for a large percentage of the methane dissociation on the outer planets; the Ly-α flux (at 1 AU) in our nominal model is 3.21×10^{11} photons cm^{-2} sec^{-1} in

a 1-Å interval centered at 1215.7 Å. A plot for solar flux versus wavelengths used in our model is shown in Figure 2-3.

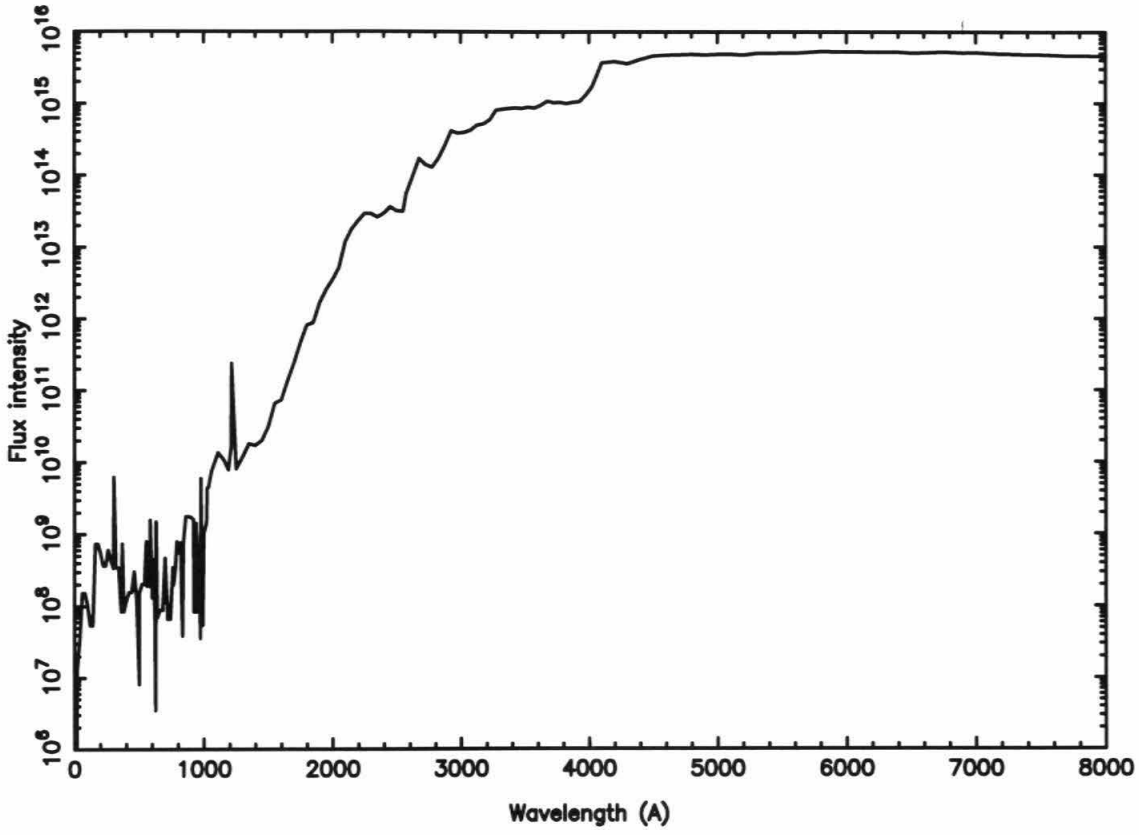

Figure 2-3. The solar flux adopted in the planetary atmosphere photochemical modeling. Wavelengths are in the unit of Å, and the unit for flux intensity is photons cm^{-2} sec^{-1}.

2.2.3. Diffusion coefficients

As described above, in the one-dimensional model, vertical-mixing processes can be parameterized by a single macroscopic eddy diffusion coefficient K that may be variable with altitude. The dynamical motion of the planetary lower atmosphere includes the large-scale circulation driven by residual heating or cooling, or absorption of momentum from upward-traveling gravity waves. The eddy diffusion coefficient profile is one of the main free parameters in the model, and is usually determined by observations.

As the atmospheric density decreases, molecular diffusion begins to dominate. A general expression for the molecular diffusion coefficient in a hydrogen atmosphere is used

$$D_i(n) = A_{H_2} T^{(S_{H_2}-1)} \frac{n_0 T_0}{n} \sqrt{m_{H_2} / m_i} , \tag{2.11}$$

where n is the total number density, T is the temperature of the atmosphere at any particular altitude, m_{H2} is the mass of the hydrogen molecule (2.01594 amu), and m_i is the mass of the diffusing species. Marrero and Mason [1972] have used experiment data to derive expressions for the molecular diffusion coefficients of various atoms and molecules in a hydrogen atmosphere. We use these experimentally derived expressions whenever possible. The molecular diffusion coefficient of CH_4, and the other hydrocarbon molecules, is taken to be

$$D = \frac{2.3 \times 10^{17} T^{0.765}}{n} \sqrt{\frac{16.04}{m_i} \left(\frac{m_i + 2.016}{18.059}\right)} . \tag{2.12}$$

2.2.4. Photochemical reactions

The tables of reactions in the Yung *et al.* [1984] Titan atmosphere model provides a major review of the laboratory, and theoretical, kinetics and photochemistry literature at that time. These tables are the largest compilation to date of hydrocarbons chemical processes occurring in a reducing planetary atmosphere. We frequently update these reaction lists on the basis of reviewing recent papers for chemical experimental, or theoretical estimated kinetics. There are several kinds of chemical reactions in the tables: (a) photodissociation (AB + $h\nu \rightarrow$ A + B); (2) insertion (A + BH $\rightarrow$ AH + B); (3) hydrogen abstraction (A + BH $\rightarrow$ AH + B); (4) combination (A + B + M $\rightarrow$ AB + M); (5) disproportionation (AB + CD $\rightarrow$ AC + BD); (6) exchange and transfer (A + BC $\rightarrow$ AB + C); and (7) cracking and hydrogen scavenging (A + H $\rightarrow$ AH, followed by AH + H $\rightarrow$ A + H_2 or $\rightarrow$ C + D). For photodissociation reactions, the model calculates their J value by integrating the products of cross sections and the solar flux over the relevant wavelength region. For each bimolecular reaction, the rate constant has been directly given in the reaction tables. However, the rate coefficients for three-body combination reactions are interpolated between the low-pressure, three-body values k_0 (cm^6 sec^{-1}) and high-pressure, two-body limiting values k_∞ (cm^3 sec^{-1}) with a simple expression that leads to the limiting values at low and high densities,

$$k(T,M) = \frac{k_0(T)k_\infty(T)}{k_\infty(T) + k_0(T)M}, \tag{2.13}$$

where M is the total atmosphere density (cm^{-3}) and k (T, M) is in units of cm^6 sec^{-1}. More realistic formula has been suggested for interpolation in the transition region between the

two limiting values k_0 and k_∞ by Troe [1977] and DeMore *et al.* [1992],

$$k(T,M) = \frac{k_0(T)k_\infty(T)}{k_\infty(T) + k_0(T)M} 0.6^{(1+\log^2(k_0(T)M/k_\infty(T)))^{-1}}. \tag{2.14}$$

In most cases of photochemical modeling, one of the challenging tasks is to prepare a sufficiently complete set of chemical reactions for all of the relevant atoms and molecules. We need to search all possible sources of kinetic rate constants, including experiments or theoretical estimates. If there are more than two rate constant values for one reaction, we also need to choose the appropriate one, or evaluate the numbers. Determining factors include the valid temperature range, experiment's bath gas, fitting method, or the reputation of the publishing group.

Chapter 3

Photochemical modeling of CH_3 abundances in the outer solar system

3.1. Introduction

One of the most important fields for photochemical modeling of the atmospheres in our solar system is the modeling of hydrocarbons. More recent contributions to our understanding of hydrocarbon photochemistry include the comprehensive works of *Gladstone et al.* [1996] for Jupiter, *Moses et al.* [2000a, b] for Saturn, *Summers and Strobel* [1989] for Uranus, *Romani et al.* [1993] and *Bishop et al.* [1998] for Neptune, and *Yung et al.* [1984], *Toublanc et al.* [1995], and *Lara et al.* [1996] for Titan. All of these modeling investigations consider a straightforward photochemical scheme initiated by methane (CH_4) photolysis followed by radical-radical and radical-molecule interactions that eventually lead to the synthesis of more complex hydrocarbons. These models provide a satisfactory explanation for the observations of stable hydrocarbon molecules, such as CH_4, C_2H_2, C_2H_4, and C_2H_6, obtained from the extensive ground-based and spacecraft (Voyager) observations. However, a rigorous test of the theory of hydrocarbon chemistry, and a systematic comparison between these models using a consistent set of photochemical reactions applied to all the atmospheres of the outer solar system, is still

lacking.

Recent observations of hydrocarbon species by the Short Wavelength Spectrometer (SWS) on the Infrared Space Observatory (ISO) provide new insights into the hydrocarbon photochemistry in the atmospheres of the outer solar system. The first detection of methyl radicals (CH_3) in the outer solar system was made in the atmospheres of Saturn and Neptune by ISO [*Bézard et al.*, 1998, 1999]. CH_3 is one of the most important radicals in hydrocarbon photochemistry because it is a product of methane photolysis and plays an essential role in forming C_2H_6, the most abundant and stable C2 species. These observations pose a challenge to current photochemical models.

The CH_3 column densities deep in the stratosphere of Saturn obtained by ISO/SWS observations were first analyzed by *Bézard et al.* [1998] to be $(1.5 - 7.5) \times 10^{13}$ cm^{-2} above 0.2 mbar and were reanalyzed by *Moses et al.* [2000a] to be $(2.5 - 6.0) \times 10^{13}$ cm^{-2} above 10 mbar. The amount of CH_3 in the stratosphere of Neptune by ISO/SWS observations is $(0.7 - 2.8) \times 10^{13}$ cm^{-2} above 0.2 mbar [*Bézard et al.*, 1999]. Current hydrocarbon photochemical models tend to overpredict the CH_3 column abundance value when using the traditionally adopted CH_3-CH_3 recombination rate constant from *Slagle et al.* [1988]. The observational value for Saturn is about a factor of 5 - 10 lower than the prediction of hydrocarbon photochemical models in which the *Slagle et al.* rate constant is used [e.g., *Bézard et al.*, 1998; *Atreya et al.*, 1998]. According to these researchers, the discrepancy could be attributed to one of two possibilities. Either the eddy diffusion coefficients on Saturn are ~ 100 times less than the standard values, or the self-reaction loss rate constant for CH_3 is about a factor of 10 higher than the value given by *Slagle et al.* [1988]. However, the first possibility is not convincing because decreasing the eddy

diffusion coefficients by 2 orders of magnitude violates the Voyager measurements (Saturn: *Courtin et al.* [1984]) in the atmosphere of those giant planets, and there is no other reason to believe in an arbitrary reduction of vertical transport since the Voyager epoch. In fact, both *Bézard et al.* [1998] and *Moses et al.* [2000a] present current models in which the CH_3 abundance matches the ISO observations by assuming a higher CH_3 recombination rate constant. We will therefore reexamine the currently adopted recombination rate constants for methyl-methyl recombination at low temperature and provide quantitative results for CH_3 column abundances in the stratospheres of those planets.

Hydrocarbon photochemistry in the upper atmospheres of the outer solar system is initiated by photolysis of methane. Primary products of CH_4 photodissociation are CH, $^1CH_2$, $^3CH_2$, and CH_3 radicals. Although the branching ratios of the various possible CH_4 photolysis pathways at the hydrogen Lyman α line are not well determined [*Smith and Raulin*, 1999; *Romani*, 1996; *Moses et al.*, 2000a], a detailed analysis of chemical reactions following primary photodissociation shows that a large portion of $^1CH_2$ radicals readily convert to CH_3 in the presence of H_2. The main paths forming CH_3 in the altitudes above 10^{-4} mbar in Jupiter or in Saturn are as follows:

$$CH_4 + h\nu \rightarrow CH_3 + H$$

or

$$CH_4 + h\nu \rightarrow {}^1CH_2 + H_2$$

$$CH_4 + h\nu \rightarrow {}^1CH_2 + 2H$$

followed by

$$^1CH_2 + H_2 \rightarrow CH_3 + H.$$

These pathways dominate the production of CH_3 radicals in the upper stratospheres of the outer solar system (see detailed discussion in section 3.2). In the middle and lower stratospheres, where less production of CH_3 radicals by photolysis is occurring, the formation of CH_3 by the reaction $H + C_2H_5 \rightarrow 2CH_3$ becomes important. A detailed discussion of the hydrocarbon chemistry can be found in a recent book by *Yung and DeMore* [1999]. Figure 3-1 shows the major pathways for producing and removing CH_3 radicals in the stratospheres of the outer solar system.

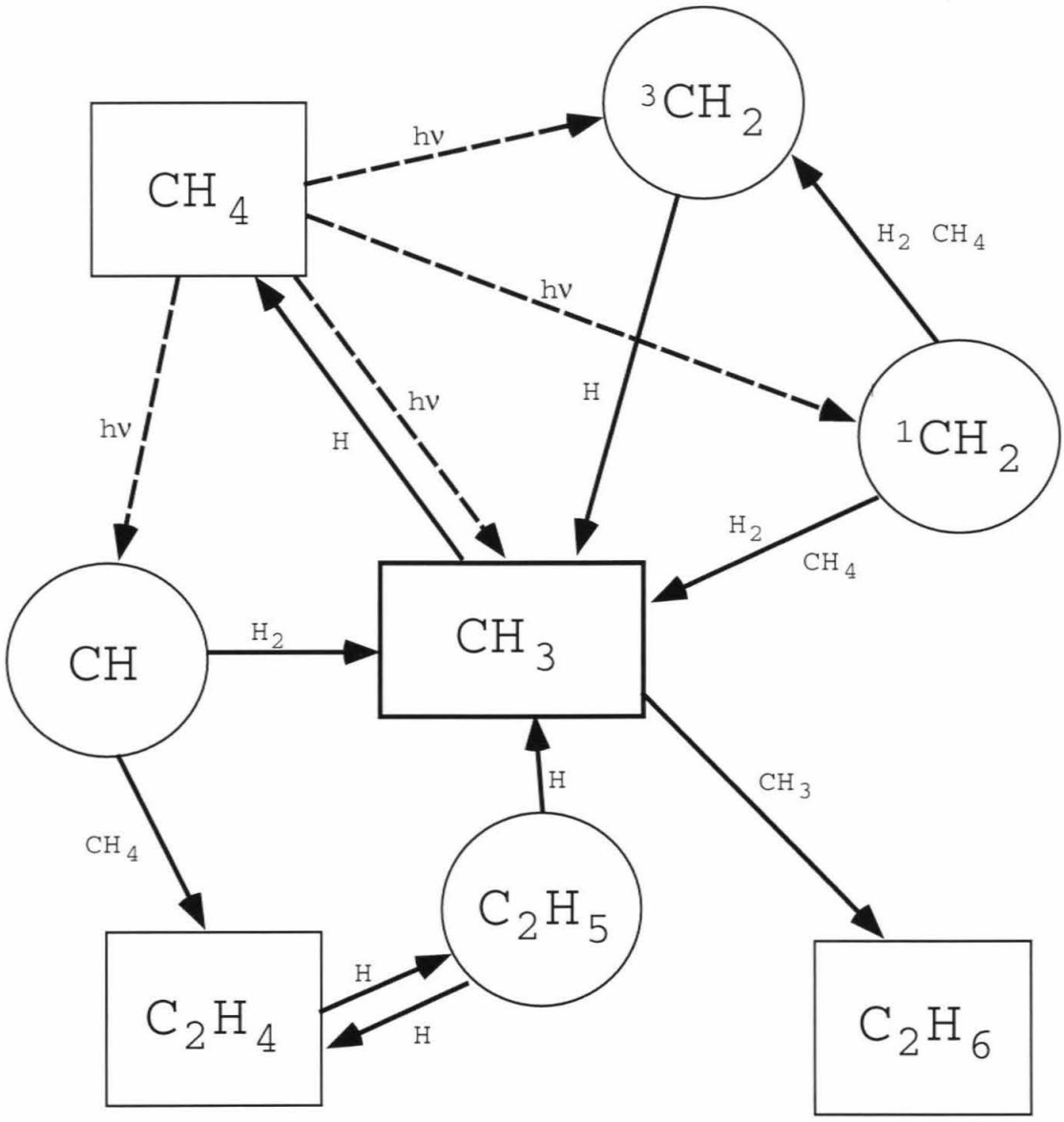

Figure 3-1. Major reaction pathways for methyl radical (CH_3) photochemistry.

Table 3-1. High-Pressure Two-Body (k_∞) and Low-pressure Three-Body (k_0) Rate Constants of Recombination Reaction $CH_3 + CH_3 + M \rightarrow C_2H_6 + M$.

	High-Pressure Constant k_∞	Low-Pressure Constant k_0
Slagle[a]	$1.5\times10^{-7}\ T^{1.18}\ e^{-329/T}$	$8.76\times10^{-7}\ T^{-7.03}\ e^{-1390/T}$
MacPherson[b]	$4.09\times10^{-11}\ e^{137/T}$	$6.0\times10^{-29}\ e^{1680/T}$
Modified Slagle[c,d]	6.0×10^{-11}	$1.8\times10^{-16}\ T^{-3.75}\ e^{-300/T}$

[a] The formulas are valid between 296 and 906 K.

[b] The formulas are valid between 296 and 577 K; k_∞ is from *MacPherson et al.* [1985] while k_0 is from *MacPherson et al.* [1983]

[c] The formula for k_0 is valid only at $T < 300$ K. For $T > 300$ K, the Slagle formula is applied.

[d] The broadening factor of low-pressure rate constant k_0 is as same as the value of Slagle, $F_{cent} = 0.381\ e^{-T/73.2} + 0.619\ e^{-T/1180}$.

In hydrogen-rich environments like the upper atmospheres of the outer solar system, a large portion of CH_3 radicals recycles back immediately to CH_4 by the reaction

$$H + CH_3 + M \rightarrow CH_4 + M. \qquad (3.1)$$

The high-pressure limit rate constant k_∞ and low-pressure limit rate constant k_0 of (3.1) used in our models will be discussed in the next section.

One of the most important reactions for the CH_3 radical is the self-recombination reaction to form the stable ethane (C_2H_6) molecule; it is also one of the major sinks of CH_3 radicals in the upper stratosphere:

$$CH_3 + CH_3 + M \rightarrow C_2H_6 + M. \qquad (3.2)$$

This three-body recombination reaction has been intensively studied and measured in the laboratory [*Hole and Mulcahy*, 1969; *Van den Bergh*, 1976; *MacPherson et al.*, 1983, 1985; *Slagle et al.*, 1988; *Du et al.*, 1996] and by theory [*Wagner and Wardlaw*, 1988; *Forst*, 1991; *Robertson et al.*, 1995; *Klippenstein and Harding*, 1999]. Two widely used empirical rate constant functions from *Slagle et al.* [1988] and *MacPherson et al.* [1983, 1985] are shown in Table 3-1. However, most of the kinetic rate coefficients for this reaction were measured at room temperature or higher. The extrapolation to low temperatures below 200 K, typical of stratospheric temperatures in the outer solar system, by current theoretical techniques is highly uncertain. *Allen* [1989] has pointed out the importance of the temperature dependence of the CH_3 recombination reaction and the possible influence for chemical models of planetary atmospheres. We will evaluate the extrapolation of the three-body rate constant of (3.2) to temperatures lower than 300 K in section 3.2. Along with these two reactions, the rate constants for some related reactions will also be discussed. Table 3-4 lists these reactions.

For the purpose of comparison, we use a one-dimensional diurnally averaged photochemical model to test the impact of the rate constant of (3.2) on the abundances of CH_3 radicals in different atmospheres of the outer solar system. Similar photochemical models have been developed for four planets and one satellite: Jupiter, Saturn, Uranus, Neptune, and Titan. Identical lists of photochemical reactions, cross sections, and rate constants were used for all of the planets, but other parameters such as the physical properties of the planet and its atmosphere (e.g., radius, mass, heliocentric distance, temperature-pressure profile, eddy diffusion coefficient profile, and radiation flux) were specific to each planet. All physical data for model atmospheres are taken from Voyager and ground-based measurements [*Yung and DeMore*, 1999]. By adopting the modified rate constant of (3.2) at low temperatures deduced in this work, our models for the atmospheres of Saturn and Neptune show reasonable agreement with the CH_3 abundances observed by ISO/SWS, and our models also show reasonable agreement with the Voyager observations for stable hydrocarbon molecules. Therefore we have confidence that our models provide reliable estimates of CH_3 concentrations in the atmospheres of Jupiter, Uranus, and Titan. These predictions may be checked by future observations.

3.2. Models and Chemical Kinetics

We developed one-dimensional photochemical models of the upper atmospheres of Jupiter, Saturn, Uranus, Neptune, and Titan on the basis of the updated generic Caltech/Jet Propulsion Laboratory photochemical model [e.g., *Gladstone et al.*, 1996]. Comprehensive studies applying this model to hydrocarbon photochemistry in the upper atmosphere of Titan, Jupiter, and Saturn have been presented by *Yung et al.* [1984], *Gladstone et al.* [1996], and *Moses et al.* [2000a, b], respectively. Because similar photochemical processes operate in the five atmospheres of the outer solar system, we adopt the same set of photochemical cross sections and chemical reactions in all of our models. The physical properties of the atmospheres, such as pressure, temperature, density, eddy diffusion coefficients, or basic planetary parameters like the distance from the Sun and gravity, are the principal differences between the planetary atmospheres. We use the most complete and recently updated set of hydrocarbon photochemical reactions taken from *Moses et al.* [2000a], except for some key reactions, which are discussed in this section. Tables 3-2 and 3-3 show the complete lists of the photodissociation reactions, and chemical reactions, respectively.

Table 3-2. Hydrocarbon photolysis reactions

		Photolysis rate $J(s^{-1})$			
	Reaction	at 10^{-8} mbar	at 1.1×10^{-3} mbar	Wavelength (nm)	Ref.
R1	$H_2 \rightarrow 2H$	2.4×10^{-10}	0	$69 \le \lambda \le 113$	a
R2	$^3CH_2 \rightarrow CH + H$	5.5×10^{-7}	5.5×10^{-7}	$99 \le \lambda \le 198$	a
R3	$CH_3 \rightarrow CH + H_2$	3.7×10^{-9}	2.6×10^{-9}	$147 \le \lambda \le 223$	a
R4	$CH_3 \rightarrow {}^1CH_2 + H$	1.4×10^{-6}	1.4×10^{-6}	$147 \le \lambda \le 153$	a
R5	$CH_4 \rightarrow CH_3 + H$	2.0×10^{-8}	3.6×10^{-11}	$97 \le \lambda \le 163$	a, b, c
R6	$CH_4 \rightarrow {}^1CH_2 + H_2$	1.0×10^{-8}	3.2×10^{-11}	$75 \le \lambda \le 163$	a
R7	$CH_4 \rightarrow {}^1CH_2 + 2H$	1.2×10^{-9}	1.2×10^{-13}	$75 \le \lambda \le 129$	a
R8	$CH_4 \rightarrow {}^3CH_2 + 2H$	1.5×10^{-9}	1.1×10^{-13}	$75 \le \lambda \le 133$	a
R9	$CH_4 \rightarrow CH + H + H_2$	1.3×10^{-8}	3.9×10^{-12}	$79 \le \lambda \le 135$	a
R10	$C_2H_2 \rightarrow C_2H + H$	1.9×10^{-8}	2.5×10^{-9}	$67 \le \lambda \le 223$	a,d,e,f,g,h
R11	$C_2H_2 \rightarrow C_2 + H_2$	8.0×10^{-9}	2.1×10^{-9}	$69 \le \lambda \le 203$	a,d,e,f,g,h
R12	$C_2H_2 \rightarrow C_2H_2^*$	0	0		
R13	$C_2H_3 \rightarrow C_2H_2 + H$	2.3×10^{-6}	2.3×10^{-6}	$415 \le \lambda \le 425$	a
R14	$C_2H_4 \rightarrow C_2H_2 + H_2$	7.3×10^{-8}	5.4×10^{-8}	$93 \le \lambda \le 203$	a,i
R15	$C_2H_4 \rightarrow C_2H_2 + 2H$	1.1×10^{-7}	6.6×10^{-8}	$93 \le \lambda \le 203$	a,i
R16	$C_2H_4 \rightarrow C_2H_3 + H$	7.2×10^{-9}	6.8×10^{-9}	$142 \le \lambda \le 203$	a,i
R17	$C_2H_5 \rightarrow CH_3 + {}^1CH_2$	1.3×10^{-6}	1.3×10^{-6}	$232 \le \lambda \le 256$	a
R18	$C_2H_6 \rightarrow C_2H_4 + H_2$	2.5×10^{-9}	1.1×10^{-10}	$93 \le \lambda \le 163$	a
R19	$C_2H_6 \rightarrow C_2H_4 + 2H$	1.7×10^{-8}	1.4×10^{-10}	$93 \le \lambda \le 163$	a
R20	$C_2H_6 \rightarrow C_2H_2 + 2H_2$	1.8×10^{-8}	3.3×10^{-10}	$93 \le \lambda \le 163$	a
R21	$C_2H_6 \rightarrow CH_4 + {}^1CH_2$	2.5×10^{-9}	1.1×10^{-10}	$93 \le \lambda \le 158$	a
R22	$C_2H_6 \rightarrow 2CH_3$	3.7×10^{-9}	2.2×10^{-11}	$93 \le \lambda \le 158$	a
R23	$C_3H_2 \rightarrow C_3 + H_2$	1.0×10^{-9}	1.0×10^{-9}		(Est.)
R24	$C_3H_3 \rightarrow C_3H_2 + H$	9.9×10^{-6}	9.9×10^{-6}	$247 \le \lambda \le 305$	a,j
R25	$C_3H_3 \rightarrow C_3H + H_2$	4.1×10^{-7}	4.1×10^{-7}	$247 \le \lambda \le 305$	a,j
R26	$CH_3C_2H \rightarrow C_3H_3 + H$	7.5×10^{-8}	7.2×10^{-8}	$142 \le \lambda \le 223$	a,k,l
R27	$CH_3C_2H \rightarrow C_3H_2 + H_2$	1.2×10^{-7}	1.2×10^{-8}	$105 \le \lambda \le 193$	a,k,l
R28	$CH_3C_2H \rightarrow {}^1CH_2 + C_2H_2$	1.3×10^{-9}	1.3×10^{-9}	$192 \le \lambda \le 223$	a,k,l
R29	$CH_2CCH \rightarrow C_3H_3 + H$	6.8×10^{-7}	5.7×10^{-7}	$120 \le \lambda \le 253$	a
R30	$CH_2CCH \rightarrow C_3H_2 + H_2$	1.6×10^{-7}	1.3×10^{-7}	$120 \le \lambda \le 253$	a
R31	$C_3H_5 \rightarrow CH_3C_2H + H$	5.0×10^{-6}	5.0×10^{-6}	$197 \le \lambda \le 256$	a
R32	$C_3H_5 \rightarrow CH_2CCH_2 + H$	2.0×10^{-5}	2.0×10^{-5}	$197 \le \lambda \le 256$	a
R33	$C_3H_5 \rightarrow C_2H_2 + CH_3$	2.2×10^{-6}	2.2×10^{-6}	$197 \le \lambda \le 256$	a

R34	$C_3H_6 \rightarrow C_3H_5 + H$	2.4×10^{-7}	2.4×10^{-7}	$162 \le \lambda \le 203$	a
R35	$C_3H_6 \rightarrow CH_3C_2H + H_2$	1.9×10^{-8}	6.4×10^{-9}	$105 \le \lambda \le 203$	a
R36	$C_3H_6 \rightarrow CH_2CCH_2 + H_2$	3.3×10^{-8}	8.5×10^{-9}	$105 \le \lambda \le 203$	a
R37	$C_3H_6 \rightarrow C_2H_4 + {}^1CH_2$	1.6×10^{-8}	9.4×10^{-9}	$105 \le \lambda \le 203$	a
R38	$C_3H_6 \rightarrow C_2H_3 + CH_3$	1.8×10^{-7}	1.6×10^{-7}	$105 \le \lambda \le 203$	a
R39	$C_3H_6 \rightarrow C_2H_2 + CH_4$	2.4×10^{-8}	1.8×10^{-8}	$105 \le \lambda \le 203$	a
R40	$C_3H_8 \rightarrow C_3H_6 + H_2$	1.7×10^{-8}	1.9×10^{-9}	$120 \le \lambda \le 168$	a
R41	$C_3H_8 \rightarrow C_2H_6 + {}^1CH_2$	5.8×10^{-9}	2.0×10^{-10}	$120 \le \lambda \le 158$	a
R42	$C_3H_8 \rightarrow C_2H_5 + CH_3$	2.8×10^{-8}	8.3×10^{-10}	$120 \le \lambda \le 158$	a
R43	$C_3H_8 \rightarrow C_2H_4 + CH_4$	1.8×10^{-8}	4.6×10^{-10}	$120 \le \lambda \le 168$	a
R44	$C_4H_2 \rightarrow C_4H + H$	7.3×10^{-8}	5.6×10^{-8}	$120 \le \lambda \le 217$	a,m
R45	$C_4H_2 \rightarrow C_2H_2 + C_2$	3.8×10^{-8}	3.0×10^{-8}	$120 \le \lambda \le 217$	a
R46	$C_4H_2 \rightarrow 2C_2H$	1.3×10^{-8}	9.5×10^{-9}	$120 \le \lambda \le 217$	a
R47	$C_4H_2 \rightarrow C_4H_2^*$	9.2×10^{-7}	8.7×10^{-7}	$120 \le \lambda \le 260$	a
R48	$C_4H_4 \rightarrow C_4H_2 + H_2$	8.8×10^{-6}	9.8×10^{-6}	$167 \le \lambda \le 233$	a
R49	$C_4H_4 \rightarrow 2C_2H_2$	2.4×10^{-6}	2.4×10^{-6}	$167 \le \lambda \le 233$	a
R50	$1\text{-}C_4H_6 \rightarrow C_4H_4 + 2H$	7.5×10^{-8}	2.5×10^{-8}	$105 \le \lambda \le 208$	a
R51	$1\text{-}C_4H_6 \rightarrow C_3H_3 + CH_3$	7.8×10^{-8}	6.3×10^{-8}	$105 \le \lambda \le 223$	a
R52	$1\text{-}C_4H_6 \rightarrow C_2H_5 + C_2H$	2.8×10^{-8}	1.5×10^{-8}	$105 \le \lambda \le 223$	a
R53	$1\text{-}C_4H_6 \rightarrow C_2H_4 + C_2H + H$	2.3×10^{-8}	8.8×10^{-9}	$105 \le \lambda \le 188$	a
R54	$1\text{-}C_4H_6 \rightarrow C_2H_3 + C_2H + H_2$	3.9×10^{-8}	6.0×10^{-9}	$105 \le \lambda \le 163$	a
R55	$1\text{-}C_4H_6 \rightarrow 2C_2H_2 + H_2$	1.5×10^{-8}	1.6×10^{-9}	$105 \le \lambda \le 163$	a
R56	$1,2\text{-}C_4H_6 \rightarrow C_4H_5 + H$	7.4×10^{-8}	7.2×10^{-8}	$167 \le \lambda \le 223$	a
R57	$1,2\text{-}C_4H_6 \rightarrow C_4H_4 + 2H$	3.2×10^{-7}	3.1×10^{-7}	$167 \le \lambda \le 203$	a
R58	$1,2\text{-}C_4H_6 \rightarrow C_3H_3 + CH_3$	4.0×10^{-7}	3.9×10^{-7}	$167 \le \lambda \le 233$	a
R59	$1,2\text{-}C_4H_6 \rightarrow C_2H_4 + C_2H_2$	2.2×10^{-8}	2.2×10^{-8}	$167 \le \lambda \le 233$	a
R60	$1,2\text{-}C_4H_6 \rightarrow C_2H_3 + C_2H_2 + H$	3.2×10^{-8}	3.1×10^{-8}	$167 \le \lambda \le 213$	a
R61	$1,2\text{-}C_4H_6 \rightarrow C_2H_3 + C_2H + H_2$	1.1×10^{-8}	1.0×10^{-8}	$167 \le \lambda \le 188$	a
R62	$1,2\text{-}C_4H_6 \rightarrow 2C_2H_2 + H_2$	4.6×10^{-8}	4.5×10^{-8}	$167 \le \lambda \le 233$	a
R63	$1,3\text{-}C_4H_6 \rightarrow C_4H_5 + H$	5.8×10^{-6}	5.8×10^{-6}	$167 \le \lambda \le 233$	a
R64	$1,3\text{-}C_4H_6 \rightarrow C_4H_4 + H_2$	1.0×10^{-6}	1.0×10^{-6}	$167 \le \lambda \le 233$	a
R65	$1,3\text{-}C_4H_6 \rightarrow C_3H_3 + CH_3$	8.4×10^{-6}	8.3×10^{-6}	$167 \le \lambda \le 233$	a
R66	$1,3\text{-}C_4H_6 \rightarrow C_2H_4 + C_2H_2$	3.5×10^{-6}	3.5×10^{-6}	$167 \le \lambda \le 233$	a
R67	$1,3\text{-}C_4H_6 \rightarrow 2C_2H_3$	2.1×10^{-6}	2.1×10^{-6}	$167 \le \lambda \le 233$	a
R68	$C_4H_8 \rightarrow 1,3\text{-}C_4H_6 + 2H$	1.4×10^{-7}	1.1×10^{-7}	$105 \le \lambda \le 203$	a
R69	$C_4H_8 \rightarrow C_3H_5 + CH_3$	3.8×10^{-7}	3.5×10^{-7}	$105 \le \lambda \le 203$	a
R70	$C_4H_8 \rightarrow CH_3C_2H + CH_4$	1.6×10^{-8}	1.3×10^{-8}	$105 \le \lambda \le 203$	a

R71	$C_4H_8 \rightarrow CH_2CCH_2 + CH_4$	2.9×10^{-8}	8.9×10^{-9}	$105 \le \lambda \le 173$	a
R72	$C_4H_8 \rightarrow C_2H_5 + C_2H_3$	5.7×10^{-8}	2.3×10^{-8}	$105 \le \lambda \le 183$	a
R73	$C_4H_8 \rightarrow 2C_2H_4$	3.9×10^{-8}	3.6×10^{-8}	$105 \le \lambda \le 203$	a
R74	$C_4H_8 \rightarrow C_2H_2 + 2CH_3$	1.8×10^{-8}	1.4×10^{-8}	$105 \le \lambda \le 183$	a
R75	$C_4H_{10} \rightarrow C_4H_8 + H_2$	5.5×10^{-8}	4.6×10^{-9}	$120 \le \lambda \le 168$	a
R76	$C_4H_{10} \rightarrow C_3H_8 + {}^1CH_2$	2.7×10^{-9}	4.1×10^{-11}	$120 \le \lambda \le 143$	a
R77	$C_4H_{10} \rightarrow C_3H_6 + CH_4$	5.5×10^{-9}	1.4×10^{-10}	$120 \le \lambda \le 168$	a
R78	$C_4H_{10} \rightarrow C_3H_6 + CH_3 + H$	1.3×10^{-8}	4.0×10^{-10}	$120 \le \lambda \le 168$	a
R79	$C_4H_{10} \rightarrow C_2H_6 + C_2H_4$	2.8×10^{-8}	1.1×10^{-9}	$120 \le \lambda \le 168$	a
R80	$C_4H_{10} \rightarrow 2C_2H_5$	2.0×10^{-8}	8.4×10^{-10}	$120 \le \lambda \le 168$	a
R81	$C_4H_{10} \rightarrow C_2H_4 + 2CH_3$	1.4×10^{-8}	3.7×10^{-10}	$120 \le \lambda \le 168$	a
R82	$C_6H_2 \rightarrow C_6H + H$	7.3×10^{-8}	5.6×10^{-8}		$= J_{44}$
R83	$C_6H_2 \rightarrow C_4H + C_2H$	1.3×10^{-8}	9.5×10^{-9}		$= J_{46}$
R84	$C_6H_6 \rightarrow H + PROD$	9.1×10^{-8}	9.0×10^{-8}	$163 \le \lambda \le 198$	n,o
R85	$C_6H_6 \rightarrow C_4H_2 + C_2H_4$	9.1×10^{-9}	9.0×10^{-9}	$163 \le \lambda \le 198$	n,o
R86	$C_6H_6 \rightarrow 2C_3H_3$	4.6×10^{-8}	4.5×10^{-8}	$163 \le \lambda \le 198$	n,o
R87	$C_6H_6 \rightarrow 3C_2H_2$	7.6×10^{-7}	7.5×10^{-7}	$163 \le \lambda \le 198$	n,o
R88	$C_8H_2 \rightarrow C_6H + C_2H$	1.3×10^{-8}	9.5×10^{-9}		$= J_{46}$
R89	$C_8H_2 \rightarrow 2C_4H$	1.3×10^{-8}	9.5×10^{-9}		$= J_{46}$

References: (a) Gladstone *et al.* [1996], (b) Mordaunt *et al.* [1993], (c) Heck *et al.* [1996], (d) Wu *et al.* [1997], (e) Smith *et al.* [1991], (f) Bénilan *et al.* [1995], (g) Segall *et al.* [1991], (h) Satyapal and Bersohn [1991], (i) Balko *et al.* [1992], (j) Fahr *et al.* [1997], (k) Seki and Okabe [1992], (l) Payne and Stief [1972], (m) Fahr and Nayak [1994], (n) Pantos *et al.* [1978], (o) Malkin. [1992].

Table 3-3. Hydrocarbon chemical reactions

	Reaction	Rate coefficient	Reference
R90	$H + H + M \rightarrow H_2 + M$	$k_0 = 2.7 \times 10^{-31}\, T^{-0.6}$	Baulch *et al.* (1994)
R91	$H + CH \rightarrow C + H_2$	$1.3 \times 10^{-10} e^{-80/T}$	Harding *et al.* (1993)
R92	$H + {}^1CH_2 \rightarrow CH + H_2$	2.0×10^{-10}	Moses *et al.* (2000)
R93	$H + {}^3CH_2 \rightarrow CH + H_2$	2.66×10^{-10}	Boullart and Peeters (1992)
R94	$H + {}^3CH_2 + M \rightarrow CH + H_2 + M$	$k_0 = 3.4 \times 10^{-32} e^{736/T}$	Moses *et al.* (2000)
		$k_\infty = 7.3 \times 10^{-12}$	Moses *et al.* (2000)
R95	$H + CH_3 + M \rightarrow CH_4 + M$	$k_0 = 2.3 \times 10^{-17} T^{-4.03} e^{-1366/T}$	Brouard *et al.* (1989)
		$k_0 = 2.52 \times 10^{-29}$, $T \leq 300K$	
		$k_\infty = 1.14 \times 10^{7}\, T^{-5.72} e^{-1644/T}$	Brouard *et al.* (1989)
		$k_\infty = 3.23 \times 10^{-10}$, $T \leq 280K$	
R96	$H + CH_4 \rightarrow CH_3 + H_2$	$6.4 \times 10^{-18}\, T^{2.11} e^{-3900/T}$	Rabinowitz *et al.* (1991)
R97	$H + C_2H + M \rightarrow C_2H_2 + M$	$k_0 = 1.26 \times 10^{-18} T^{-3.1} e^{-721/T}$	Tsang and Hampson (1986)
		$k_\infty = 3.0 \times 10^{-10}$	Tsang and Hampson (1986)
R98	$H + C_2H_2 \rightarrow C_2H + H_2$	$1.0 \times 10^{-10}\, e^{-11200/T}$	Tsang and Hampson (1986)
R99	$H + C_2H_2 + M \rightarrow C_2H_3 + M$	$k_0 = 8.2 \times 10^{-31} e^{-352/T}$	Hoyermann *et al.* (1968) and
			Gordon *et al.* (1978)
		$k_\infty = 1.4 \times 10^{-11} e^{-1300/T}$	Baulch *et al.* (1994)
R100	$H + C_2H_3 \rightarrow C_2H_2 + H_2$	2.0×10^{-11}	Baulch *et al.* (1994)
R101	$H + C_2H_3 + M \rightarrow C_2H_4 + M$	$k_0 = 5.5 \times 10^{-27}$	Fahr *et al.* (1991) and
		$k_\infty = 1.82 \times 10^{-10}$	Monks *et al.* (1995)
R102	$H + C_2H_4 + M \rightarrow C_2H_5 + M$	$k_0 = 1.3 \times 10^{-29} e^{-380/T}$	Baulch *et al.* (1994)
		$k_\infty = 6.6 \times 10^{-15}\, T^{1.28} e^{-650/T}$	Baulch *et al.* (1994)
R103	$H + C_2H_5 \rightarrow 2CH_3$	1.25×10^{-10}	Sillesen *et al.* (1993)
R104	$H + C_2H_5 \rightarrow C_2H_4 + H_2$	3.0×10^{-12}	Tsang and Hampson (1986)
R105	$H + C_2H_5 + M \rightarrow C_2H_6 + M$	$k_0 = 5.5 \times 10^{-22} T^{-2} e^{-1040/T}$	$10 \times$ Gladstone *et al.* (1996)
		$k_\infty = 2.6 \times 10^{-10}$	Sillesen *et al.* (1996)
R106	$H + C_2H_6 \rightarrow C_2H_5 + H_2$	$2.35 \times 10^{-15} T^{-1.5} e^{-3725/T}$	Baulch *et al.* (1992)
R107	$H + C_3H_2 + M \rightarrow C_3H_3 + M$	$k_0 = 2.52 \times 10^{-28}$	Est. based on $10 \times$ R95
		$k_\infty = 5.0 \times 10^{-11}$	Estimate
R108	$H + C_3H_3 + M \rightarrow CH_3C_2H + M$	$k_0 = 5.5 \times 10^{-27}$	Est. based on R101
		$k_\infty = 1.15 \times 10^{-10} e^{-276/T}$	Homann and Wellmann (1983)
R109	$H + C_3H_3 + M \rightarrow CH_2CCH_2 + M$	$k_0 = 5.5 \times 10^{-27}$	Est. based on R101
		$k_\infty = 1.15 \times 10^{-10} e^{-276/T}$	Est. based on R108
R110	$H + CH_3C_2H \rightarrow CH_3 + C_2H_2$	$9.63 \times 10^{-12} e^{-1560/T}$	Wagner and Zellner (1972a)
	$H + CH_3C_2H + M \rightarrow C_3H_5 + M$	$k_0 = 2.0 \times 10^{-29}$	Est., Whytock *et al.* (1976)

	$k_\infty = 3.98 \times 10^{-11} e^{-1152/T}$	Whytock *et al.* (1976)
R112 $H + CH_2CCH_2 \rightarrow CH_3C_2H + H$	$4.0 \times 10^{-12} e^{-1006/T}$	Wagner and Zellner (1976b)
R113 $H + CH_2CCH_2 + M \rightarrow C_3H_5 + M$	$k_0 = 2.0 \times 10^{-29}$	Est. based on R111
	$k_\infty = 1.0 \times 10^{-11} e^{-1006/T}$	Wagner and Zellner (1972b)
R114 $H + C_3H_5 \rightarrow CH_3C_2H + H_2$	1.4×10^{-11}	Est. based on Tsang (1991)
R115 $H + C_3H_5 \rightarrow CH_2CCH_2 + H_2$	1.4×10^{-11}	Est. based on Tsang (1991)
R116 $H + C_3H_5 \rightarrow CH_3 + C_2H_3$	1.4×10^{-11}	Estimate
R117 $H + C_3H_5 + M \rightarrow C_3H_6 + M$	$k_0 = 2.0 \times 10^{-28}$	Est. based on 10 × R111
	$k_\infty = 2.8 \times 10^{-10}$	Hanning-Lee and Pilling(1992)
R118 $H + C_3H_6 \rightarrow C_3H_5 + H_2$	$2.87 \times 10^{-19} T^{2.5} e^{-1254/T}$	Tsang (1991)
R119 $H + C_3H_6 \rightarrow CH_3 + C_2H$ 4	$2.2 \times 10^{-11} e^{-1641/T}$	Tsang (1991)
R120 $H + C_3H_6 + M \rightarrow C_3H_7 + M$	$k_0 = 1.3 \times 10^{-28} e^{-380/T}$	Est. based on 10 × R102
	$k_\infty = 2.2 \times 10^{-11} e^{-785/T}$	Tsang (1991)
R121 $H + C_3H_7 \rightarrow C_3H_6 + H_2$	3.0×10^{-12}	Tsang (1988)
R122 $H + C_3H_7 \rightarrow C_2H_5 + CH_3$	6.0×10^{-11}	Tsang (1988)
R123 $H + C_3H_7 + M \rightarrow C_3H_8 + M$	$k_0 = 5.5 \times 10^{-22} T^{-2} e^{-1040/T}$	Est. based on R105
	$k_\infty = 2.49 \times 10^{-10}$	Munk *et al.* (1986)
R124 $H + C_3H_8 \rightarrow C_3H_7 + H_2$	$2.2 \times 10^{-18} T^{2.54} e^{-3400/T}$	Tsang (1988)
R125 $H + C_4H + M \rightarrow C_4H_2 + M$	$k_0 = 1.26 \times 10^{-18} T^{-3.1} e^{-721/T}$	Est. based on R97
	$k_\infty = 3.0 \times 10^{-10}$	Est. based on R97
R126 $H + C_4H_2 + M \rightarrow C_4H_3 + M$	$k_0 = 1.0 \times 10^{-28}$	Est. Yung *et al.* (1984)
	$k_\infty = 1.39 \times 10^{-10} e^{-1184/T}$	Nava *et al.* (1986)
R127 $H + C_4H_3 \rightarrow 2C_2H_2$	1.5×10^{-11}	Est. based on R100
R127aH $+ C_4H_3 \rightarrow C_4H_2 + H_2$	5.0×10^{-12}	Est. based on R100
R128 $H + C_4H_3 + M \rightarrow C_4H_4 + M$	$k_0 = 6.0 \times 10^{-30} e^{1680/T}$	Est. based on 0.1×R158
	$k_\infty = 8.56 \times 10^{-10} e^{-405/T}$	Duran *et al.* (1988)
R129 $H + C_4H_4 + M \rightarrow C_4H_5 + M$	$k_0 = 6.0 \times 10^{-31} e^{1680/T}$	Est. based on 0.01×R158
	$k_\infty = 3.3 \times 10^{-12}$	Schwanebeck and Warnatz (1975)
R130 $H + C_4H_5 \rightarrow C_4H_4 + H_2$	2.0×10^{-11}	Est. based on R100
R131 $H + C_4H_5 + M \rightarrow 1\text{-}C_4H_6 + M$	$k_0 = 6.0 \times 10^{-30} e^{1680/T}$	Est. based on 0.1×R158
	$k_\infty = 1.0 \times 10^{-10}$	Gladstone *et al.* (1996)
R132 $H + C_4H_9 \rightarrow C_4H_8 + H_2$	1.5×10^{-12}	Tsang (1990)
R133 $H + C_4H_9 + M \rightarrow C_4H_{10} + M$	$k_0 = 6.0 \times 10^{-30} e^{1680/T}$	Est. based on 0.1×R158
	$k_\infty = 6.0 \times 10^{-11}$	Tsang (1990)
R134 $H + C_6H_2 + M \rightarrow C_6H_3 + M$	$k_0 = 1.0 \times 10^{-28}$	Est. based on R126
	$k_\infty = 1.39 \times 10^{-10} e^{-1184/T}$	Est. based on R126
R135 $H + C_6H_3 \rightarrow C_6H_2 + H_2$	2.0×10^{-11}	Est. based on R127

R136 $H + C_8H_3 \rightarrow C_8H_2 + H_2$	2.0×10^{-11}	Est. based on R127
R137 $C + H_2 + M \rightarrow {}^3CH_2 + M$	$k_0 = 7.0 \times 10^{-32}$	Husain and Young (1975)
	$k_\infty = 2.06 \times 10^{-11} e^{-57/T}$	Harding *et al.* (1993)
R138 $C + C_2H_2 + M \rightarrow C_3H_2 + M$	$k_0 = 1.0 \times 10^{-31}$	Moses *et al.* (2000)
	$k_\infty = 2.1 \times 10^{-10}$	Haider and Husain (1993)
R139 $CH + H_2 \rightarrow {}^3CH_2 + H$	$3.75 \times 10^{-10} e^{-1662/T}$	Becker *et al.* (1991)
R140 $CH + H_2 + M \rightarrow CH_3 + M$	$k_0 = 3.4 \times 10^{-31} e^{736/T}$	Becker *et al.* (1991)
	$k_\infty = 7.3 \times 10^{-11}$	Becker *et al.* (1991)
R141 $CH + CH_4 \rightarrow C_2H_4 + H$	$5.0 \times 10^{-11} e^{200/T}$	Berman and Lin (1983)
R142 $CH + C_2H_2 \rightarrow C_3H_2 + H$	$3.49 \times 10^{-10} e^{61/T}$	Berman *et al.* (1982)
R143 $CH + C_2H_4 \rightarrow C_2H_2 + CH_3$	$2.23 \times 10^{-10} e^{173/T}$	Berman *et al.* (1982)
R144 $CH + C_2H_6 \rightarrow C_3H_6 + H$	$1.8 \times 10^{-10} e^{132/T}$	Berman and Lin (1983)
R145 $^1CH_2 + H_2 \rightarrow {}^3CH_2 + H_2$	1.26×10^{-11}	Braun *et al.* (1970); and
R146 $^1CH_2 + H_2 \rightarrow CH_3 + H$	9.24×10^{-11}	Langford *et al.* (1983)
R147 $^1CH_2 + CH_4 \rightarrow {}^3CH_2 + CH_4$	1.2×10^{-11}	Bohland *et al.* (1985b)
R148 $^1CH_2 + CH_4 \rightarrow 2CH_3$	5.9×10^{-11}	Bohland *et al.* (1985b)
R149 $2\,{}^3CH_2 \rightarrow C_2H_2 + H$	$1.8 \times 10^{-10} e^{-400/T}$	Baulch *et al.* (1992)
R150 $^3CH_2 + CH_3 \rightarrow C_2H_4 + H$	7.0×10^{-11}	Baulch *et al.* (1992)
R151 $^3CH_2 + CH_4 \rightarrow 2CH_3$	$7.1 \times 10^{-12} e^{-5051/T}$	Bohland *et al.* (1985a)
R152 $^3CH_2 + C_2H_2 \rightarrow C_3H_2 + H_2$	$5.0 \times 10^{-12} e^{-3332/T}$	Bohland *et al.* (1986)
R153 $^3CH_2 + C_2H_2 \rightarrow C_3H_3 + H$	$1.5 \times 10^{-11} e^{-3332/T}$	Bohland *et al.* (1986)
R154 $^3CH_2 + C_2H_2 + M \rightarrow CH_3C_2H$	$k_0 = 6.0 \times 10^{-29} e^{1680/T}$	Est. based on R158
	$k_\infty = 2.0 \times 10^{-12} e^{-3330/T}$	Est. based on R153
R155 $^3CH_2 + C_2H_3 \rightarrow C_2H_2 + CH_3$	8.0×10^{-11}	Moses *et al.* (2000)
R156 $^3CH_2 + C_2H_5 \rightarrow C_2H_4 + CH_3$	8.0×10^{-11}	Moses *et al.* (2000)
R157 $CH_3 + H_2 \rightarrow CH_4 + H$	$6.6 \times 10^{-20} T^{2.24} e^{-3220/T}$	Rabinowitz *et al.* (1991)
R158 $2CH_3 + M \rightarrow C_2H_6 + M$	$k_0 = 6.0 \times 10^{-29} e^{1680/T}$	MacPherson *et al.* (1983)
	$k_\infty = 6.0 \times 10^{-11}$	Baulch *et al.* (1992)
R159 $CH_3 + C_2H_3 \rightarrow CH_4 + C_2H_2$	3.4×10^{-11}	Fahr *et al.* (1991)
R160 $CH_3 + C_2H_3 + M \rightarrow C_3H_6 + M$	$k_0 = 6.0 \times 10^{-28} e^{1680/T}$	Est. based on 10×R158
	$k_\infty = 1.2 \times 10^{-10}$	Fahr *et al.* (1991)
R161 $CH_3 + C_2H_5 \rightarrow CH_4 + C_2H_4$	2.0×10^{-12}	Baulch *et al.* (1992)
R162 $CH_3 + C_2H_5 + M \rightarrow C_3H_8 + M$	$k_0 = 1.01 \times 10^{-22} e^{341/T}$ (T≤200K)	Gladstone *et al.* (1996)
	$k_0 = 2.22 \times 10^{-26} e^{2026/T}$ (T>200K)	Gladstone *et al.* (1996)
	$k_\infty = 6.64 \times 10^{-11}$	Sillesen *et al.* (1993)
R163 $CH_3 + C_3H_3 + M \rightarrow 1,2\text{-}C_4H_6$	$k_0 = 6.0 \times 10^{-28} e^{1680/T}$	Est. based on 10×R158
	$k_\infty = 4.2 \times 10^{-12}$	Wu and Kern (1987)

R164 $CH_3 + C_3H_3 + M \rightarrow 1\text{-}C_4H_6$	$k_0 = 6.0 \times 10^{-28} e^{1680/T}$	Est. based on 10×R158
	$k_\infty = 4.2 \times 10^{-12}$	Wu and Kern (1987)
R165 $CH_3 + C_3H_5 \rightarrow CH_4 + CH_3C_2H$	$2.5 \times 10^{-12} T^{-0.32} e^{66/T}$	Tsang (1991)
R166 $CH_3 + C_3H_5 \rightarrow CH_4 + CH_2CCH_2$	$2.5 \times 10^{-12} T^{-0.32} e^{66/T}$	Tsang (1991)
R167 $CH_3 + C_3H_5 + M \rightarrow C_4H_8 + M$	$k_0 = 7.12 \times 10^{-22} e^{715/T}$, T≤200K	Est. based on 10×R171
	$k_0 = 4.57 \times 10^{-24} e^{2184/T}$, T>200K	Est. based on 10×R171
	$k_\infty = 6.5 \times 10^{-11}$	Garland and Bayes (1990)
R168 $CH_3 + C_3H_6 \rightarrow CH_4 + C_3H_5$	$2.32 \times 10^{-13} e^{-4390/T}$	Kinsman and Roscoe (1990)
R169 $CH_3 + C_3H_6 + M \rightarrow C_4H_9 + M$	$k_0 = 1.3 \times 10^{-28} e^{-380/T}$	Est. based on 10×R102
	$k_\infty = 1.34 \times 10^{-13} e^{-3330/T}$	Kinsman and Roscoe (1990)
R170 $CH_3 + C_3H_7 \rightarrow CH_4 + C_3H_6$	$1.9 \times 10^{-11} T^{-0.3}$	Tsang (1988)
R171 $CH_3 + C_3H_7 + M \rightarrow C_4H_{10} + M$	$k_0 = 7.12 \times 10^{-22} e^{715/T}$, T≤200K	Laufer *et al.* (1983)
	$k_0 = 4.57 \times 10^{-24} e^{2184/T}$, T>200K	Laufer *et al.* (1983)
	$k_\infty = 3.2 \times 10^{-10} T^{-0.32}$	Tsang (1988)
R172 $CH_3 + C_3H_8 \rightarrow CH_4 + C_3H_7$	$1.5 \times 10^{-24} T^{3.7} e^{-3600/T}$	Tsang (1988)
R173 $CH_3 + C_4H_5 \rightarrow CH_4 + C_4H_4$	3.4×10^{-11}	Est. based on R159
R174 $CH_3 + C_4H_5 + M \rightarrow PROD + M$	$k_0 = 7.12 \times 10^{-22} e^{715/T}$, T≤200K	Est. based on R171
	$k_0 = 4.57 \times 10^{-24} e^{2184/T}$, T>200K	Est. based on R171
	$k_\infty = 3.2 \times 10^{-10} T^{-0.32}$	Est. based on R171
R175 $C_2 + H_2 \rightarrow C_2H + H$	$1.77 \times 10^{-10} e^{-1469/T}$	Pitts *et al.* (1982)
R176 $C_2 + CH_4 \rightarrow C_2H + CH_3$	$5.05 \times 10^{-11} e^{-297/T}$	Pitts *et al.* (1982)
R177 $C_2H + H_2 \rightarrow C_2H_2 + H$	$1.2 \times 10^{-11} e^{-998/T}$	Opansky and Leone (1996b)
R178 $C_2H + CH_4 \rightarrow C_2H_2 + CH_3$	$1.2 \times 10^{-11} e^{-491/T}$	Opansky and Leone (1996a)
R179 $C_2H + C_2H_2 \rightarrow C_4H_2 + H$	$1.1 \times 10^{-10} e^{28/T}$	Pederson *et al.* (1993)
R180 $C_2H + C_2H_4 \rightarrow C_4H_4 + H$	$7.8 \times 10^{-11} e^{134/T}$	Opansky and Leone (1996b)
R181 $C_2H + C_2H_6 \rightarrow C_2H_2 + C_2H_5$	$3.5 \times 10^{-11} e^{3/T}$	Opansky and Leone (1996b)
R182 $C_2H + C_4H_2 \rightarrow C_6H_2 + H$	$1.1 \times 10^{-10} e^{28/T}$	Est. based on R179
R183 $C_2H + C_4H_{10} \rightarrow C_4H_9 + C_2H_2$	1.0×10^{-11}	Tsang (1990)
R184 $C_2H + C_6H_2 \rightarrow C_6H_2 + H$	$1.1 \times 10^{-10} e^{28/T}$	Est. based on R179
R185 $C_2H + C_8H_2 \rightarrow PROD$	$1.1 \times 10^{-10} e^{28/T}$	Est. based on R179
R190 $C_2H_3 + H_2 \rightarrow C_2H_4 + H$	$5 \times 10^{-20} T^{2.63} e^{-4298/T}$	Fahr *et al.* (1995)
R191 $C_2H_3 + C_2H_2 \rightarrow C_4H_4 + H$	$3.31 \times 10^{-12} e^{-2516/T}$	Fahr and Stein (1988)
R192 $C_2H_3 + C_2H_2 + M \rightarrow C_4H_5 + M$	$k_0 = 8.2 \times 10^{-30} e^{-352/T}$	Est. based on 10×R99
	$k_\infty = 4.17 \times 10^{-19} T^{1.9} e^{-1058/T}$	Weissman and Benson (1988)
R193 $2C_2H_3 \rightarrow C_2H_4 + C_2H_2$	2.4×10^{-11}	Fahr *et al.* (1991)
R194 $2C_2H_3 + M \rightarrow 1,3\text{-}C_4H_6 + M$	$k_0 = 6.0 \times 10^{-28} e^{1680/T}$	Est. based on 10×R158

	$k_\infty = 1.2 \times 10^{-10}$	Fahr *et al.* (1991)
R195 $C_2H_3 + C_2H_4 \rightarrow 1\text{-}C_4H_6 + H$	$1.05 \times 10^{-12} e^{-1559/T}$	Fahr and Stein (1988)
R196 $C_2H_3 + C_2H_5 \rightarrow 2C_2H_4$	8.0×10^{-13}	Tsang and Hampson (1986)
R197 $C_2H_3 + C_2H_5 \rightarrow C_2H_6 + C_2H_2$	8.0×10^{-13}	Tsang and Hampson (1986)
R199 $C_2H_3 + C_2H_5 + M \rightarrow C_4H_8 + M$	$k_0 = 6.0 \times 10^{-28} e^{1680/T}$	Est. based on 10×R158
	$k_\infty = 8.0 \times 10^{-13}$	Tsang and Hampson (1986)
R200 $C_2H_5 + H_2 \rightarrow C_2H_6 + H$	$5.1 \times 10^{-24} T^{3.6} e^{-4253/T}$	Tsang and Hampson (1986)
R201 $2C_2H_5 \rightarrow C_2H_6 + C_2H_4$	2.4×10^{-12}	Baulch *et al.* (1992)
R202 $2C_2H_5 + M \rightarrow C_4H_{10} + M$	$k_0 = 1.55 \times 10^{-22} e^{586/T}$, T≤200K	Laufer *et al.* (1983)
	$k_0 = 5.52 \times 10^{-24} e^{1253/T}$, T>200K	Laufer *et al.* (1983)
	$k_\infty = 1.4 \times 10^{-11} e^{35/T}$	Gladstone *et al.* (1996)
R203 $C_3 + H_2 \rightarrow C_3H + H$	1.0×10^{-14}	Moses *et al.* (2000)
R204 $C_3H + H_2 \rightarrow C_3H_2 + H$	1.0×10^{-14}	Moses *et al.* (2000)
R205 $C_3H_2 + C_2H_2 + M \rightarrow PROD$	$k_0 = 6.0 \times 10^{-31} e^{1680/T}$	Est. based on R158
	$k_\infty = 2.0 \times 10^{-11} e^{-3330/T}$	Est. based on 0.01×R154
R206 $C_3H_2 + C_2H_3 \rightarrow C_3H_3 + C_2H_2$	8.0×10^{-11}	Moses *et al.* (2000)
R207 $C_3H_2 + C_2H_5 \rightarrow C_3H_3 + C_2H_4$	8.0×10^{-11}	Moses *et al.* (2000)
R208 $2C_3H_3 + M \rightarrow C_6H_6 + M$	$k_0 = 6.0 \times 10^{-28} e^{1680/T}$	Est. based on R158
	$k_\infty = 1.2 \times 10^{-10}$	Morter *et al.* (1994)
R209 $C_3H_5 + H_2 \rightarrow C_3H_6 + H$	$5.25 \times 10^{-11} e^{-9913/T}$	Allara and Shaw (1980)
R210 $C_3H_7 + H_2 \rightarrow C_3H_8 + H$	$3.0 \times 10^{-21} T^{2.84} e^{-4600/T}$	Tsang (1988)
R211 $C_4H + H_2 \rightarrow C_4H_2 + H$	$1.2 \times 10^{-11} e^{-998/T}$	Est. based on R177
R212 $C_4H + CH_4 \rightarrow C_4H_2 + CH_3$	$1.2 \times 10^{-11} e^{-491/T}$	Est. based on R178
R213 $C_4H + C_2H_2 \rightarrow C_6H_2 + H$	2.5×10^{-11}	Brachold *et al.* (1988)
R214 $C_4H + C_2H_6 \rightarrow C_4H_2 + C_2H_5$	$3.5 \times 10^{-11} e^{3/T}$	Est. based on R181
R215 $C_4H + C_4H_2 \rightarrow C_8H_2 + H$	$1.1 \times 10^{-10} e^{28/T}$	Est. based on R179
R216 $C_4H + C_6H_2 \rightarrow PROD$	$1.1 \times 10^{-10} e^{28/T}$	Est. based on R179
R217 $C_4H + C_8H_2 \rightarrow PROD$	$1.1 \times 10^{-10} e^{28/T}$	Est. based on R179
R236 $C_4H_5 + H_2 \rightarrow 1\text{-}C_4H_6 + H$	$6.61 \times 10^{-15} T^{0.5} e^{-1864/T}$	Weissman and Benson (1988)
R237 $C_4H_5 + C_2H_2 \rightarrow C_6H_6 + H$	$3.16 \times 10^{-17} T^{1.47} e^{-2471/T}$	Westmoreland *et al.* (1989)
R238 $C_6H + H_2 \rightarrow C_6H_2 + H$	$1.2 \times 10^{-11} e^{-998/T}$	Est. based on R177
R239 $C_6H + CH_4 \rightarrow C_6H_2 + CH_3$	$1.2 \times 10^{-11} e^{-491/T}$	Est. based on R178
R240 $C_6H + C_2H_2 \rightarrow C_8H_2 + H$	$1.1 \times 10^{-10} e^{28/T}$	Est. based on R179
R241 $C_6H + C_2H_6 \rightarrow C_6H_2 + C_2H_5$	$3.5 \times 10^{-11} e^{3/T}$	Est. based on R181
R242 $C_6H + C_4H_2 \rightarrow PROD$	$1.1 \times 10^{-10} e^{28/T}$	Est. based on R179
R243 $C_6H + C_6H_2 \rightarrow PROD$	$1.1 \times 10^{-10} e^{28/T}$	Est. based on R179
R244 $C_6H + C_8H_2 \rightarrow PROD$	$1.1 \times 10^{-10} e^{28/T}$	Est. based on R179

Readers can also refer to Tables II and III in their paper for detailed discussion and Table 3-4 of this for the key chemical reactions whose rate coefficients we have modified.

Table 3-4. Rate Constants of Key Reactions Adopted in Our Models

Reaction	Rate Constant	Reference
$H + CH_3 + M \rightarrow CH_4 + M$	$k_0 = 2.3 \times 10^{-17}\, T^{-4.03}\, e^{-1366/T}$ ($T > 300$ K)	*Moses et al.* [2000a]
	$k_0 = 1.4 \times 10^{-19}\, T^{-3.75}\, e^{-300/T}$ ($T < 300$ K)	see text
$H + C_2H_3 \rightarrow C_2H_2 + H_2$	7.50×10^{-11}	*Monks et al.* [1995]; see text
$H + C_2H_5 \rightarrow 2\,CH_3$	6.0×10^{-11}	*Baulch et al.* [1992]
$^1CH_2 + H_2 \rightarrow CH_3 + H$	7.00×10^{-11} ($T < 150$ K)	see text
	9.24×10^{-11} ($T > 150$ K)	
$2CH_3 + M \rightarrow C_2H_6 + M$	$k_0 = 1.8 \times 10^{-6}\, T^{-3.75}\, e^{-300/T}$	see text
	$k_\infty = 6.0 \times 10^{-11}$	
	($T < 300$ K)	

The units of rate constants in this table are $cm^3\ s^{-1}$ (two-body reaction) and $cm^6\ s^{-1}$ (three-body reaction).

Model atmospheres of the planets are assumed to be hydrostatic, and the pressure-temperature profiles are determined principally from Voyager measurements. In this work, we take the atmospheric parameters of Titan, Jupiter, and Saturn from previous models by *Yung et al.* [1984], *Gladstone et al.* [1996], and *Moses et al.* [2000a], respectively. The thermal structure and vertical mixing in the upper atmosphere of Uranus used in our model are taken from *Herbert et al.* [1987] and *Summers and Strobel* [1989]. The temperature profile for Neptune is taken from *Lindal* [1992] and *Broadfoot et al.* [1989]. The eddy diffusion coefficient of the stratosphere of Neptune is critical for hydrocarbon modeling. We use the eddy-mixing profile suggested by *Romani et al.* [1993], with $K \approx 5 \times 10^7$ cm^2 s^{-1} for $0.5 > p > 10^{-4}$ mbar, because it provides a reasonable fit to the lower limit of the C_2H_6 mixing ratio from the Voyager Infrared Radiometer Interferometer and Spectrometer (IRIS) observations (1×10^{-6}) in the lower stratosphere. Figure 3-2 presents the pressure-temperature profiles in the upper atmospheres of Jupiter, Saturn, Titan, Uranus, and Neptune used in our models; Figure 3-3 shows the vertical eddy diffusion coefficient profiles in the upper atmospheres of those models.

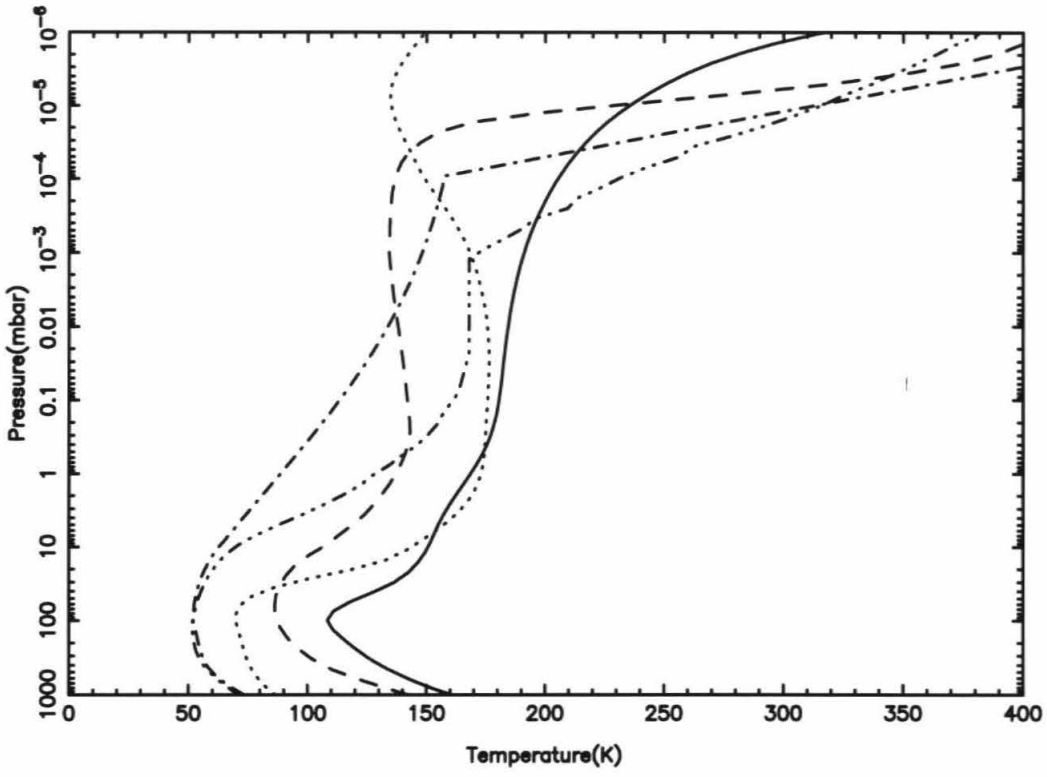

Figure 3-2. Temperature profiles used for the model atmospheres: Jupiter (solid), Saturn (dashed), Uranus (dash-dot), Neptune (dash-dot-dot-dot), and Titan (dotted).

Bézard et al. [1998, 1999] pointed out the importance of the rate constant of the recombination reaction (3.2) at lower temperatures (T < 200 K) in determining the CH_3 abundance on the outer planets. The pressure and temperature regimes where significant CH_4 photodissociation and (3.2) occur are $p \approx 10^{-3}$–10^{-4} mbar and $T \approx 120$ to 160 K in the atmospheres of Saturn or Neptune. However, the rate constant of (3.2) is uncertain since no reliable measurements of the rate constant have been made at any temperature below 200 K in laboratory studies. Also, all of the theoretical studies [*Wagner and Wardlaw*, 1988; *Forst*, 1991; *Robertson et al.*, 1995; *Klippenstein and*

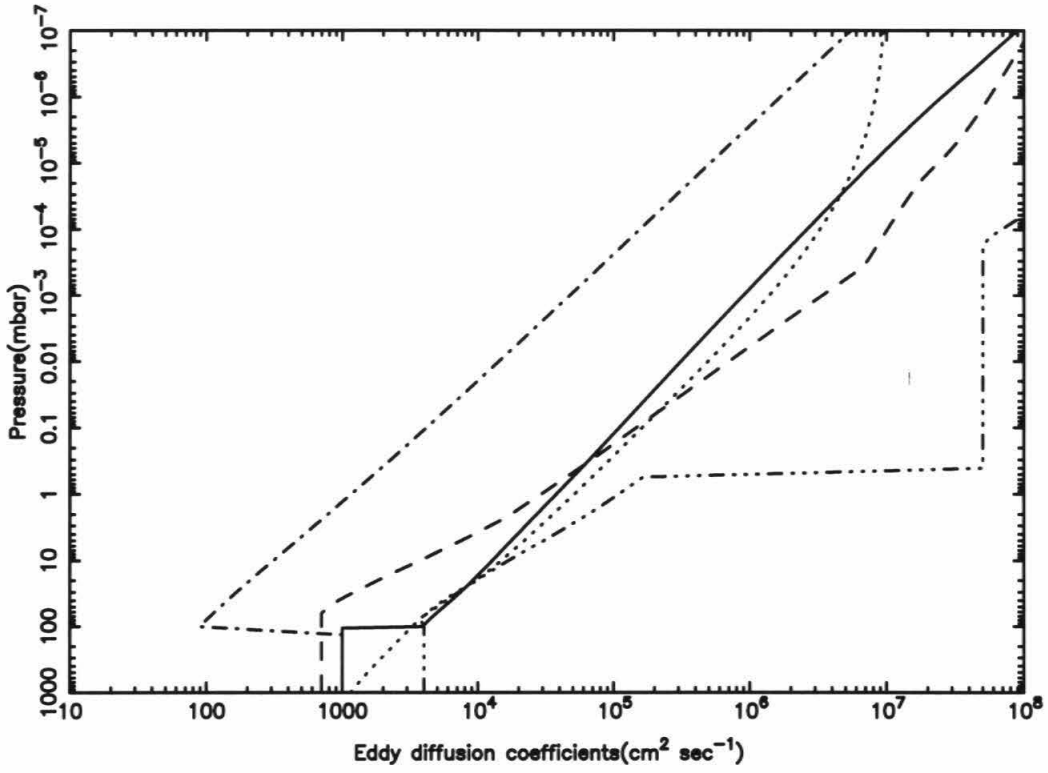

Figure 3-3. Eddy diffusion profiles used for the model atmospheres of Jupiter, Saturn, Uranus, Neptune, and Titan. The lines denote the same planets as in Figure 3-2.

Harding, 1999] of the rate constant function via temperature are unconfirmed under 296 K. Empirical extrapolations of the low-pressure rate constant k_0 and high-pressure rate constant k_∞, by *Slagle et al.* [1988], and *MacPherson et al.* [1983, 1985], are shown in Table 3-1.

Figures 3-4 and 3-5 give the two-body and three-body rate constants, respectively, calculated from 100 to 1000 K, using the formulas of *Slagle et al.* [1988] (solid line) and *MacPherson et al.* [1985] (dash-dotted line) extrapolated to temperatures outside the range in which the formulas were designed. Figures 3-4 and 3-5 also include the

experimental kinetics data in the two-body (high-pressure) and three-body (low-pressure) limit measured by *MacPherson et al.* [1983, 1985]. Both functions by Slagle et al. and *MacPherson et al.* [1985] are consistent with experimental values within their error bars above 300 K, but they significantly deviate from each other at low temperatures. *MacPherson et al.*'s [1985] formulas increase sharply at low temperatures because of the positive exponents, which are adopted for matching the increasing trend of experimental values above 300 K. In contrast, the formula of Slagle et al. decreases when we move to the low-temperature regime, which is opposite to the experimental trend at higher temperatures. We believe that the Slagle et al. formulas are correct only within their temperature range (296 K < T < 906 K) and cannot provide reasonable extrapolation at low temperatures (100 K < T < 200 K). In particular, the low-pressure rate constant k_0 tends to increase as temperature decreases owing to the possible longer lifetime of the intermediate activated complex formed in three-body collisions. The drastic decrease predicted by Slagle et al.'s formula is thus unreasonable. On the other hand, a very rapid increase of rate constant when T < 150 K for *MacPherson et al.*'s [1985] extrapolation at low temperatures is also hard to justify, because of the bulk slower motion of the reactants. There are 2 orders of magnitude difference between these formulas at 150 K, the typical temperature of the stratospheres of the outer solar system.

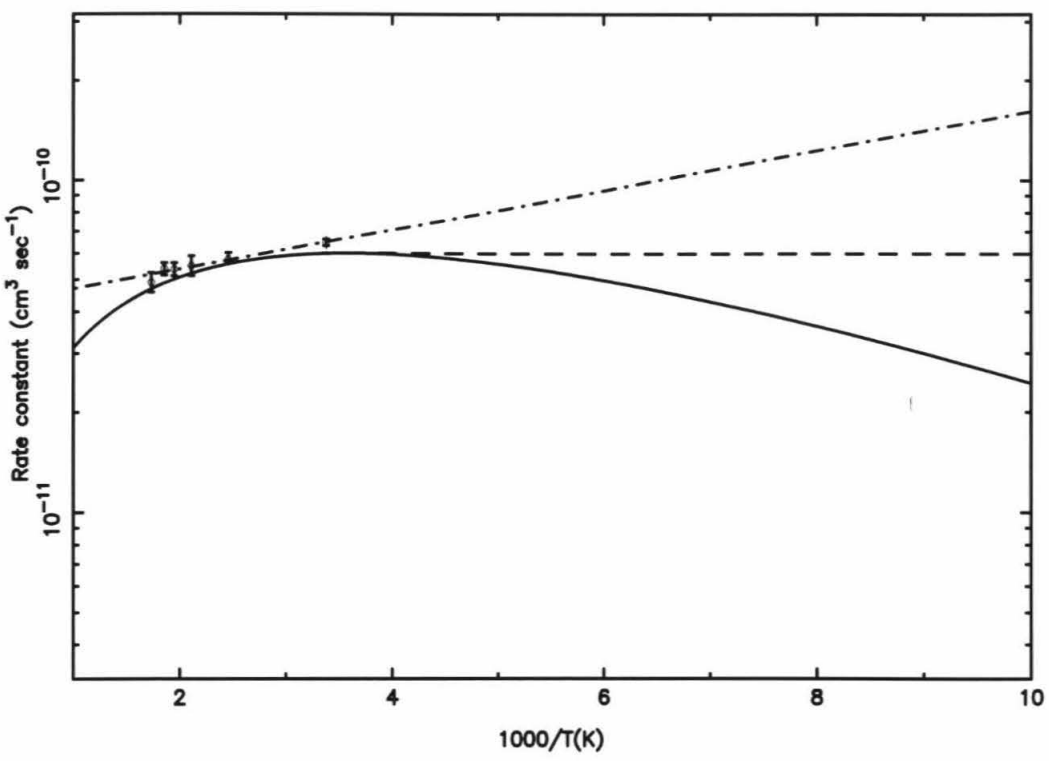

Figure 3-4. High-pressure (two-body) rate constant of $CH_3 + CH_3 \rightarrow C_2H_6$ reaction at temperatures from 100 to 1000K. The solid line, dashed line, and dash-dotted line denote the rate constant formulas derived from *Slagle et al.* [1988], Modified Slagle (this work), and *MacPherson et al.* [1985], respectively. The points with error bars from 296 to 577 K are laboratory results by MacPherson *et al.* [1985].

Our approach is based on an alternative estimate of the rate constant for (3.2). Heuristic reasons [*Troe*, 1977a, b; *Laufer et al.*, 1983] are briefly described as follows, along with preliminary estimates. For the high-pressure limit $CH_3 + CH_3 \rightarrow C_2H_6$, the rate constant k_∞ tends to increase as temperature is reduced to 200 K because of the shift in the position of the transition state to larger C-C bonding distance. This effect may continue as temperature approaches 100 K. On the other hand, the collision frequency goes as the square root of temperature, which tends to counteract the effect

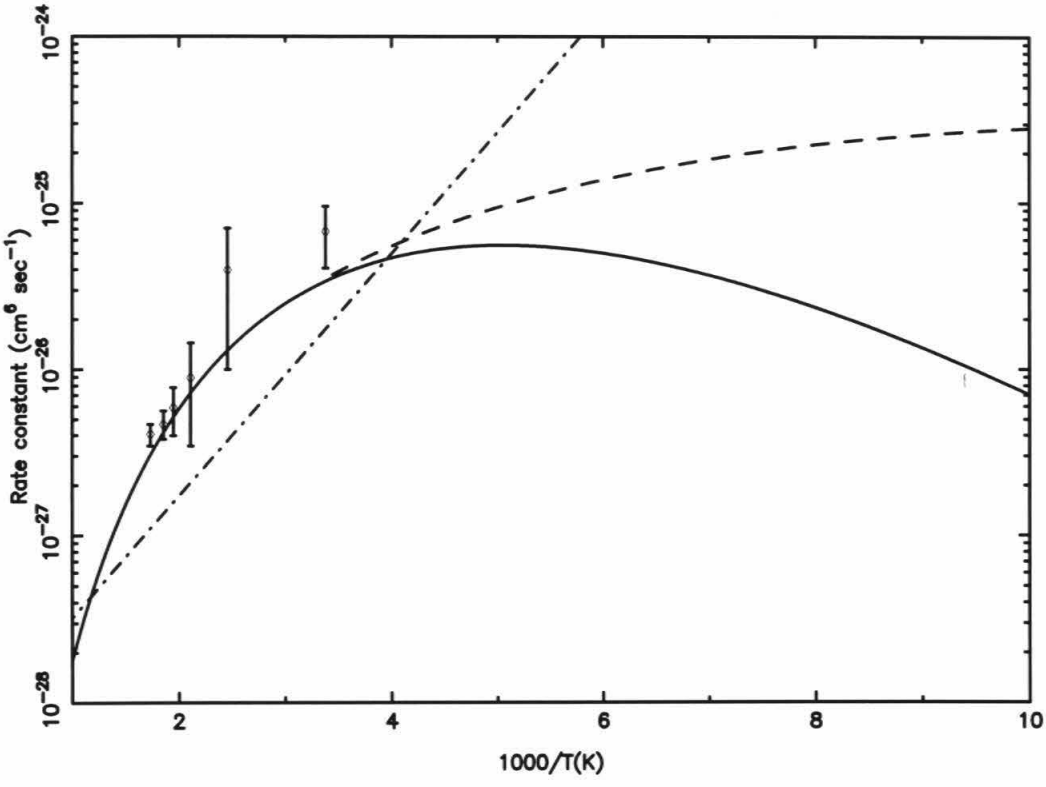

Figure 3-5. Same as Figure 3-4, but for the low-pressure (three-body) rate constant of $CH_3 + CH_3 + M \rightarrow C_2H_6 + M$.

of the changing transition state. These two effects may contribute comparable but opposite corrections to the low-temperature reaction rate. Therefore we propose a constant $k_\infty = 6.0 \pm 3.0 \times 10^{-11}$ cm^3 s^{-1} for T less than 300 K. This value and the error bar were suggested by *Baulch et al.* [1992] and are also consistent with all laboratory measurement values below 1000 K. At temperatures higher than 300 K, we adopt *Slagle et al*'s [1988] two-body rate constant formula, obtaining

$$k_\infty = 1.5 \times 10^{-11}\, T^{1.18}\, e^{137/T} \text{ cm}^3 \text{ s}^{-1} \qquad T > 300 \text{ K}$$

$$k_\infty = 6.0 \pm 3.0 \times 10^{-11} \text{ cm}^3 \text{ s}^{-1} \qquad T < 300 \text{ K} \tag{3.3}$$

For the three-body rate constant k_0, we expect an increase of k_0 as the temperature decreases owing to the longer lifetime of the intermediate activated complex as the internal thermal energy decreases in the low-temperature regime [*Laufer et al.*, 1983]. Slower motion and a smaller rate of collisions counteract this effect, as mentioned previously. These effects suggest a gradual increase of k_0 at low temperature. We can also notice this increasing trend for the measured rate constants at 500, 400, and 300 K, by a factor of 2 - 3, from Figure 3-5. At 300 K the *Slagle et al.* [1988] formula gives k_0 (300 K) = 3.3×10^{-26} cm^6 s^{-1}; thus reasonable estimates for k_0 at low temperatures might be k_0 (200 K) ~ 1.0×10^{-25} cm^6 s^{-1} and k_0 (100 K) ~ 3.0×10^{-25} cm^6 s^{-1}. By a smooth connection with Slagle et al.'s function at $T > 300$ K, we propose a low-pressure rate constant:

$$k_0 = 8.77 \times 10^{-7}\, T^{7.03}\, e^{-1390/T} \text{ cm}^6 \text{ s}^{-1} \qquad T > 300 \text{ K}$$

$$k_0 = 1.8 \times 10^{-6}\, T^{-3.75}\, \text{e}^{-300/T} \text{ cm}^6 \text{ s}^{-1} \qquad T < 300 \text{ K} \tag{3.4}$$

Fitting the combination of the estimated values at 100, 200, and 300 K by using the Arrhenius expression derives this "modified Slagle's" formula. The dashed lines in both Figures 3-4 and 3-5 show the two-body and three-body "modified Slagle's" rate constants, respectively. The pressure-broadening parameter F_{cent} for our estimated k_0 is assumed to be the same as Slagle's value: $F_{\text{cent}} = 0.381\, e^{-T/73.2} + 0.619\, e^{-T/1180}$. The bath gas for estimating the low-pressure rate constant is H_2, which is the dominant gas component in the atmospheres of Jupiter, Saturn, Uranus, and Neptune. The only exception is in the atmosphere of Titan, which is 98% N_2 (Table 3-5). Theoretically, H_2 is not as efficient as N_2 in deactivating the energized $C_2H_6^*$ molecule, so that three-body rate constants in H_2 bath gas may be slower than in N_2 bath gas. The

three-body rate constants, especially for CH_3 recombination reaction and CH_3 recycling to CH_4 reaction, could be higher for Titan. However, we have tested the sensitivity of the model by increasing k_0 for $2CH_3 + M \rightarrow C_2H_6 + M$ and $H + CH_3 + M \rightarrow CH_4 + M$ by a factor of 1.5 for Titan. The result of the test run shows only small changes (< 10%), so that we may ignore the effect of different bath gases. The reason is that the above two reactions compete for CH_3 radicals. Hence, to first order, the efficiencies of the bath gases cancel. We must emphasize that these results are preliminary estimates. We expect to refine them with the application of the RRKM theory.

Moses et al. [2000a] evaluate the rate constant of (3.1) ($H + CH_3 + M \rightarrow CH_4 + M$) on the basis of actual rate measurements of *Brouard et al.* [1989] to derive the temperature-dependent low- and high-pressure limiting formulas for their Saturn model. The expression ((R95) in Table III in their paper) fits the 300 – 600 K data of *Brouard et al.* [1989] reasonably well. However, since the extrapolation to colder temperatures is uncertain, they assume constant rate constants below 300 K to avoid an unphysical turnover in the rates at low temperatures. We notice the similarity between (3.1) and (3.2), and would expect a gradual increase of k_0 of (3.1) when moving to the low temperatures. The following expression replaces the constant low-pressure limiting rate constant (2.5×10^{-29} cm^6 s^{-1}) at $T < 300$ K:

$$k_0 = 1.4 \times 10^{-19}\, T^{-3.75}\, e^{-300/T} \qquad T < 300 \text{ K} \tag{3.5}$$

At 150 K this formula yields a low-pressure limiting rate constant value between the value estimated by *Moses et al.* [2000a] and the corresponding rate constant shown in Table 3-4 of *Gladstone et al.* [1996]. At temperatures above ~300 K we use the *Moses et al.* [2000a] expression.

Preliminary results showed stratospheric C_2H_2 abundances on Neptune that were lower than observations, so we reexamined the chemical production and destruction mechanisms of C_2H_2. The C_2H_2 abundance in the lower stratosphere ($0.1 - 5 \times 10^{-3}$ mbar) of Neptune is maintained by the two-body reaction $H + C_2H_3 \rightarrow C_2H_2 + H_2$. We expect that the rate constants used in previous models (6.0×10^{-12} cm^3 s^{-1} for *Gladstone et al.* [1996, (R85)]; 2.0×10^{-11} cm^3 s^{-1} for *Moses et al.* [2000a, (R100)]) could be underestimates. The direct experimental measurement of vinyl radicals reacting with hydrogen atoms by *Heinemann et al.* [1986] shows the rate constant 4.98×10^{-11} cm^3 s^{-1} at 293 K. *Monks et al.* [1995] have also determined the total rate constants of $H + C_2H_3 \rightarrow$ Products to be $(1.0 \pm 0.3) \times 10^{-10}$ cm^3 s^{-1} at $T = 213$ and 298 K by laboratory experiments. Two major channels of vinyl radical reactions with a hydrogen atom, the three-body reaction (a) $H + C_2H_3 + M \rightarrow C_2H_4 + M$ and the two-body reaction (b) $H + C_2H_3 \rightarrow C_2H_2 + H_2$, have been considered. The fractional product yields Γ derived by Monks et al. show that pathway b dominates at low temperatures (i.e., $\Gamma_b(298\ K) = 0.67 \pm 0.18$ and $\Gamma_b(213\ K) = 0.76 \pm 0.16$). Considering all of these experimental facts, we adopt a reasonable rate constant value (7.5×10^{-11} cm^3 s^{-1}) for $H + C_2H_3 \rightarrow C_2H_2 + H_2$ to ensure that pathway b dominates. This value along with that for channel a producing C_2H_4, does not exceed the error bar of the total reaction rate coefficient for the reaction of vinyl radicals and H, $(1.0 \pm 0.3) \times 10^{-10}$ cm^3 s^{-1}.

The photolysis of CH_4 at Lyman α (1216 Å) is the starting point for producing complex hydrocarbon molecules in the upper region of these outer solar system atmospheres. Four kinds of radicals, CH_3, $^1CH_2$, $^3CH_2$, and CH, have been considered as possible fragments from the breaking of methane molecules by solar UV radiation.

Different radicals lead to various routes and hydrocarbon products. Therefore the branching ratio of CH_4 photolysis may be important to determine product distributions between stable C2 hydrocarbons like C_2H_2 and C_2H_6. Unfortunately, the branching ratios of CH_4 at Lyman α are not well determined owing to the high reactivity of some of the photolysis products and to other experimental difficulties. In this work we adopt the branching ratios suggested by *Slanger and Black* [1982], which were used in the Jupiter hydrocarbon model by *Gladstone et al.* [1996]. The direct production of CH_3 by photolysis of CH_4 is negligible, and the primary channels for $^1CH_2$, $^3CH_2$, and CH are 47, 45, and 8%, respectively. However, *Moses et al.* [2000a] used the photodissociation channels by *Mordaunt et al.* [1993], *Ashfold et al.* [1992], and *Heck et al.* [1996] and other previous laboratory data. According to our sensitivity tests, these two sets of branching ratios lead to only minor differences for C2 hydrocarbon abundances on Jupiter, Saturn and Uranus that are within the errors of the observations. On the other hand, using different CH_4 photolysis channels would seriously affect C2 hydrocarbon mixing ratios on Neptune that could be distinguished by the Voyager IRIS observations. We will discuss the results in the sensitivity test section.

Since the C_2H_6/C_2H_2 ratios in the models seem to be affected by the primary radical yields following CH_4 photodissociation, the interradical exchange reactions could be important along with radical-molecule reactions. In our preliminary Neptune model we found that the C_2H_2 abundance in the lower stratosphere is sensitive to the interradical exchange reaction, $^1CH_2 + H_2 \rightarrow CH_3 + H$. The rate constant of the reaction $^1CH_2 + H_2 \rightarrow CH_3 + H$ may be overestimated in the previous planetary hydrocarbon models. *Gladstone et al.* [1996] and *Moses et al.* [2000a] use the value

of 9.24×10^{-11} cm^3 s^{-1}, which was taken from absolute rate constants measured by Langford *et al.* [1983]. However, Langford et al. measured only the collisional removal rate of $^1CH_2$ radical with hydrogen molecule at 295 K. The experiment does not guarantee the dissociation of the H_2 molecule and the production of the CH_3 radical after collision. The earlier experimental rate constant of the same reaction by *Pilling and Robertson* [1977] is smaller than 9.24×10^{-11} cm^3 s^{-1}. Other similar reactions used in our model, $^1CH_2 + H_2 \rightarrow {}^3CH_2 + H_2$ ($k = 1.26 \times 10^{-11}$ cm^3 s^{-1}), $^1CH_2 + CH_4 \rightarrow {}^3CH_2 + CH_4$ ($k = 1.20 \times 10^{-11}$ cm^3 s^{-1}), and $^1CH_2 + CH_4 \rightarrow 2\ CH_3$ ($k = 5.9 \times 10^{-11}$ cm^3 s^{-1}), are not as fast. Therefore we estimate the rate constant of $^1CH_2 + H_2 \rightarrow CH_3 + H$ to be 7.0×10^{-11} cm^3 s^{-1} for $T < 150$ K, which is ~ 2/3 of the value determined by *Langford et al.* [1983] (see Table 3-4) at low temperatures. The actual value needs to be confirmed by laboratory experiments and theoretical studies.

We also change the $H + C_2H_5 \rightarrow 2\ CH_3$ reaction rate to $k = 6.0 \times 10^{-11}$ cm^3 s^{-1}, which was suggested by *Baulch et al.* [1992] other than by *Sillesen et al.* [1993]. All hydrocarbon chemical reactions that are different from Table III of *Moses et al.*'s [2000a] Saturn paper are summarized in Table 3-4.

This chapter will focus on the consequences of using different CH_3 recombination rate constant expressions. In addition to the rate constant for (3.2), we will carry out a systematic testing of the sensitivity of CH_3 to all key reactions in the model, especially for Neptune. Also, the sensitivity to the temperature variation in the crucial pressure region $p \approx 10^{-3}$–10^{-4} mbar and to the vertical eddy diffusion coefficients on Saturn and Neptune will be tested. The validation of the photochemical model is extremely important for its application to atmospheric evolution. Eventually, the uncertainties in key rate coefficients will have to be

resolved in laboratory studies. The modeling and sensitivity studies will help to focus the kinetics community on the critical issues.

Table 3-5. Some Important Physical Properties in Our Models.

	Jupiter	Saturn	Uranus	Neptune	Titan
Distance, AU	5.2	9.6	19.2	30.1	9.6
Gravity, cm s^{-2}	2325	1032	869	1100	135
Pressure, mbar	1.5×10^{-3}	5.9×10^{-5}	7.9×10^{-2}	2.4×10^{-4}	1.0×10^{-3}
Temperature,[a] K	191	139	116	209	169
Eddy coefficient,[a] cm^2 s^{-1}	7.5×10^{5}	1.2×10^{7}	4.7×10^{3}	5.0×10^{7}	1.3×10^{6}
Density,[a] cm^{-3}	5.6×10^{13}	3.1×10^{12}	5.0×10^{15}	8.2×10^{12}	4.6×10^{13}
Scale height,[a] km	29.3	55.3	45.3	71.4	54.0
CH_4 mixing, ratio[a]	8.2×10^{-5}	1.8×10^{-4}	1.8×10^{-6}	1.4×10^{-4}	2.0×10^{-2}
Dominant gas	H_2	H_2	H_2	H_2	N_2

The physical properties are given at the pressure level of the maximum CH_3 mixing ratio (i.e., where the most significant CH_3 photochemical reactions occur) in the atmospheres of Jupiter, Saturn, Uranus, and Neptune. In the case of Titan, we present the atmospheric data at the 10^{-3} mbar level because the maximum CH_3 mixing ratio is at and above the upper boundary level of our model.

[a] The values at the pressure level of the maximum CH_3 mixing ratio

3.3. Model Results

We calculated the CH_3 abundances by using our hydrocarbon photochemical models for five atmospheres. Some important physical properties and characteristics of the atmospheres at the pressure level where the CH_3 mixing ratio is a maximum (i.e., where the most significant CH_3 photochemical reactions occur) are presented in Table 3-5. For comparison, we carried out modeling studies using the three versions of rate constants for (2), discussed in the previous section. These cases are hereafter referred to as "Slagle," "MacPherson," and "Modified Slagle." The resulting CH_3 column densities are summarized in Table 3-6.

Table 3-6. Column Densities of CH_3 Radicals Above the Tropopause Region for Different Cases.

	Slagle	MacPherson	Modified Slagle
Jupiter	4.5	1.5	3.3
Saturn	8.3	1.6	5.1
Titan	336	38.3	191
Uranus	0.37	0.18	0.25
Neptune	3.0	1.4	2.2

The column density values are in 10^{13} cm^{-2} and were measured at above 100 mbar pressure level.

The column abundance values in Table 3-6 are total column densities of CH_3 above the lower stratosphere. The results for Saturn and Neptune can be compared to the ISO/SWS measurements. In Saturn the "Slagle" case yielded a value of 8.3×10^{13} cm^{-2}, about a factor of 1.5 higher than the observed value, $(2.5 - 6.0) \times 10^{13}$ cm^{-2}, deduced by *Moses et al.* [2000a] above the 10 mbar level. The excess of methyl radicals results from the low rate coefficient of *Slagle et al.*'s [1988] three-body formula for (3.2), as was first pointed out by *Bézard et al.* [1998, 1999]. There is obviously too little methyl radical loss via $CH_3 + CH_3 + M \rightarrow C_2H_6 + M$. On the other hand, the model value for the CH_3 column density obtained using "MacPherson" (1.6×10^{13} cm^{-2}) is less than the ISO observation. The value of "Modified Slagle" (5.1×10^{13} cm^{-2}) is in good agreement with the ISO/SWS measurement.

For the Neptune model, in comparison with the observational value $(0.7 - 2.8) \times 10^{13}$ cm^{-2} deduced by *Bézard et al.* [1999] above the 0.2 mbar level, both the "MacPherson" (1.4×10^{13} cm^{-2}) and "Modified Slagle" (2.2×10^{13} cm^{-2}) cases fit the ISO/SWS data within the uncertainty range. The "Slagle" value (3.0×10^{13} cm^{-2}) obviously fails to fit the observational range because of the slow rate of CH_3 loss from methyl-methyl recombination at the low temperatures of Neptune's stratosphere [cf. *Bézard et al.,* 1999]. The proposed "Modified Slagle" models for both Saturn and Neptune are in good agreement with ISO observations. However, the "MacPherson" rate constant formula also fits the CH_3 observations in Neptune. By considering both Saturn and Neptune cases, and the fact that the "MacPherson" formula gives unrealistic high rates at low temperatures, we therefore conclude that our modified expression for the CH_3 recombination rate provides the best fit to ISO observations among these candidates.

We may notice from Table 3-6 the low CH_3 column abundance in the upper stratosphere of Uranus and the high CH_3 column abundance in Titan. Lower values on Uranus than on other planets are due in large part to its smaller eddy mixing profile, as shown in Figure 3-3. This effect may be seen from the comparative studies for varying the bulk eddy diffusion coefficient in Saturn and Neptune in Table 3-7. On the other hand, the more stagnant atmosphere in Uranus confines methane to lower altitudes. In fact, according to our model and others [e.g., *Summers and Strobel*, 1989; *Herbert et al.*, 1987], the eddy diffusion coefficient profile in the stratosphere of Uranus is at least 2 orders of magnitude less than the eddy profiles in Jupiter and Saturn.

Table 3-7. CH_3 Column Abundances in the Upper Atmospheres of Saturn and Neptune above 10 mbar for Saturn and 0.2 mbar for Neptune

CH_3 Column Abundances, cm^{-2}	Saturn	Neptune
ISO/SWS	$(2.5 - 6.0) \times 10^{13}$	$(0.7 - 2.8) \times 10^{13}$
Best fit model [a]	5.1×10^{13}	2.2×10^{13}
$T(z) + 10$ K [b]	5.4×10^{13}	2.4×10^{13}
$T(z) - 10$ K [c]	5.0×10^{13}	2.1×10^{13}
Bulk eddy $\times$ 2 [d]	8.5×10^{13}	2.6×10^{13}
Bulk eddy / 2 [e]	3.6×10^{13}	1.7×10^{13}

The CH_3 column abundance values were derived from sensitivity test models compared with the "best-fit" model, which uses the reaction rate constants listed in Table 3-2.

[a] The "best fit" model denotes our current photochemical model using the modified Slagle rate constant of CH_3 recombination reaction, and the rate constant list in Table 3-2.

[b] Best fit model + increasing temperature by 10 K at all altitudes.

[c] Best fit model + decreasing temperature by 10 K at all altitudes.

[d] Best fit model + bulk atmospheric eddy diffusion coefficient times 2 at all altitudes.

[e] Best fit model + bulk atmospheric eddy diffusion coefficient divided by 2 at all altitudes.

The unusually high total abundance of CH_3 radicals in the upper atmosphere of Titan is due to the low concentration of H atoms, resulting in very low probability for recycling CH_3 back to CH_4 via (3.1). Future observations of these atmospheres should provide tests for our model predictions.

Our models should provide results consistent with hydrocarbon observations, especially the Voyager data, in the atmospheres of the outer solar system. Figures 3-6

to 3-10 present the vertical profiles of the major hydrocarbon species in our models of Jupiter, Saturn, Uranus, Neptune, and Titan, respectively. The C_2H_2 and C_2H_6 measurements by Voyager are shown as pressure level ranges and error bars. The CH_3 recombination reaction rate constant used in all of those models is the "Modified Slagle" case. For the purpose of comparison, we have chosen the most abundant and long-lived disequilibrium hydrocarbon molecules, C_2H_2, C_2H_4, and C_2H_6, to be shown with the CH_3 radical in each plot. Most of these stable hydrocarbon profiles are in agreement with previous models and observations of the giant planets and Titan (e.g., Jupiter: *Gladstone et al.* [1996]; Saturn: *Moses et al.* [2000a, b] and *Lindal et al.* [1985]; Titan: *Yung et al.* [1984]; Uranus: *Summers and Strobel* [1989] and *Bishop et al.* [1990]; Neptune: *Romani et al.* [1993] and *Kostiuk et al.* [1992]).

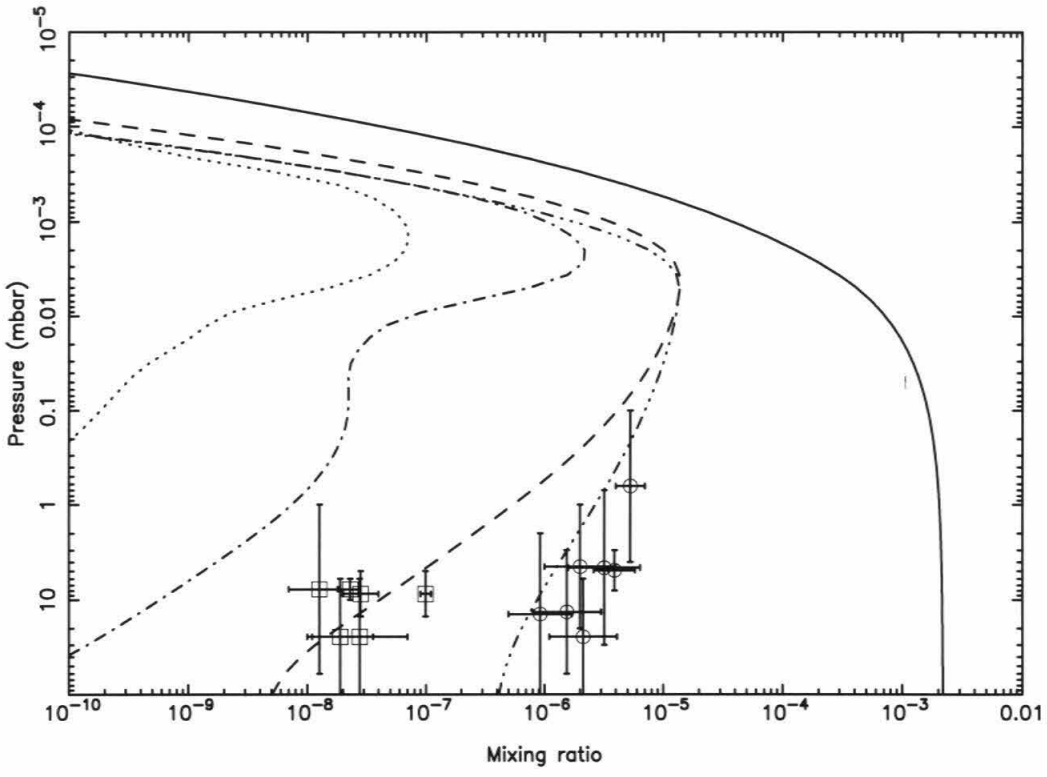

Figure 3-6. Model mixing ratios for hydrocarbons on Jupiter: CH_4 (solid), C_2H_2 (dashed), C_2H_4 (dash-dot), C_2H_6 (dash-dot-dot-dot), and CH_3 (dotted). This case was run by adopting the "Modified Slagle" rate constant for $CH_3 + CH_3 + M \rightarrow C_2H_6 + M$ reaction at low temperatures. Voyager IRIS and ground-based observations: C_2H_2 (open square) and C_2H_6 (open circle).

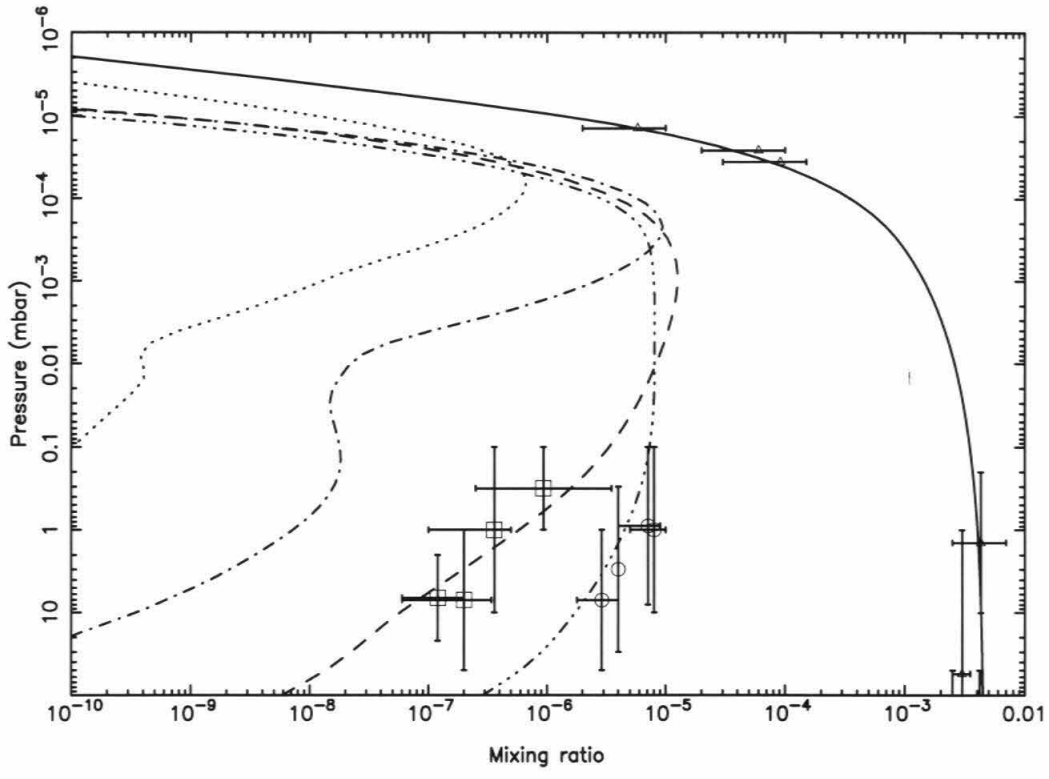

Figure 3-7. Same as Figure 3-6, but for Saturn. Voyager UVS observations: CH_4 (open triangle).

For Jupiter, as shown in Figure 3-6, the C_2H_2 and C_2H_6 mixing ratio profiles compare reasonably well with the ground and satellite observations, including the Voyager IRIS measurement in the North Equatorial Belt (NEB) region (at a latitude of 10^{o} N) with $f(C_2H_2) = (0.7 - 2.3) \times 10^{-8}$ from 1 to 60 mbar and $f(C_2H_6) = (0.8 - 3.0) \times 10^{-6}$ from 3 to 60 mbar (W. Maguire et al., private communication, 1993). The recent ground-based observations at mid-infrared wavelengths by *Sada et al.* [1998] with $f(C_2H_2) = (1.8 - 2.8) \times 10^{-8}$ at 8 mbar and $f(C_2H_6) = (2.6 - 5.8) \times 10^{-6}$ at 5 mbar also show good agreement with our Jupiter model. For Saturn we also compare the C_2H_2

and C_2H_6 mixing ratios from our models to the previous observations, as shown in Figure 3-7. On Saturn the IRIS data at mid-latitudes are $f(C_2H_2) = (0.6 - 3.4) \times 10^{-7}$ and $f(C_2H_6) = (1.8 - 4.0) \times 10^{-6}$ from 5 to 100 mbar [*Courtin et al.,* 1984]. On Titan the IRIS data at mid-latitudes are $f(C_2H_2) = (2.0 - 3.6) \times 10^{-6}$ and $f(C_2H_6) = (1.0 - 2.1) \times 10^{-5}$ from 1 to 10 mbar [*Coustenis et al.,* 1989; 1991]. Both Figures 3-7 and 3-10 demonstrate that our hydrocarbon profiles for Saturn and Titan compare well with both Voyager and ground-based observations. The recent observations in the stratosphere of Saturn by ISO yielded $f(C_2H_2) = 2.5 \times 10^{-7}$ and $f(C_2H_6) = 4.0 \times 10^{-6}$ from 0.3 to 30 mbar [*de Graauw et al.,* 1997]; these values also match our result.

Analysis of Voyager 2 data in the stratosphere of Uranus provides the abundance of C_2H_2 ($\approx 1 \times 10^{-8}$) and C_2H_6 ($\approx (1 - 2) \times 10^{-8}$) only at higher altitudes (above 0.1 mbar pressure level) by ultraviolet spectrometer occultation measurement [*Herbert et al.,* 1987; *Bishop et al.,* 1990]. IUE observation shows a similar result with both C_2H_2 and $C_2H_6 \approx 1 \times 10^{-8}$ above the 0.5 mbar level [*Caldwell et al.,* 1988]. Our Uranus model is in agreement with these observations at 0.1 - 0.01 mbar, as shown in Figure 3-8. However, hydrocarbon abundances in the lower stratosphere of Uranus still need to be verified.

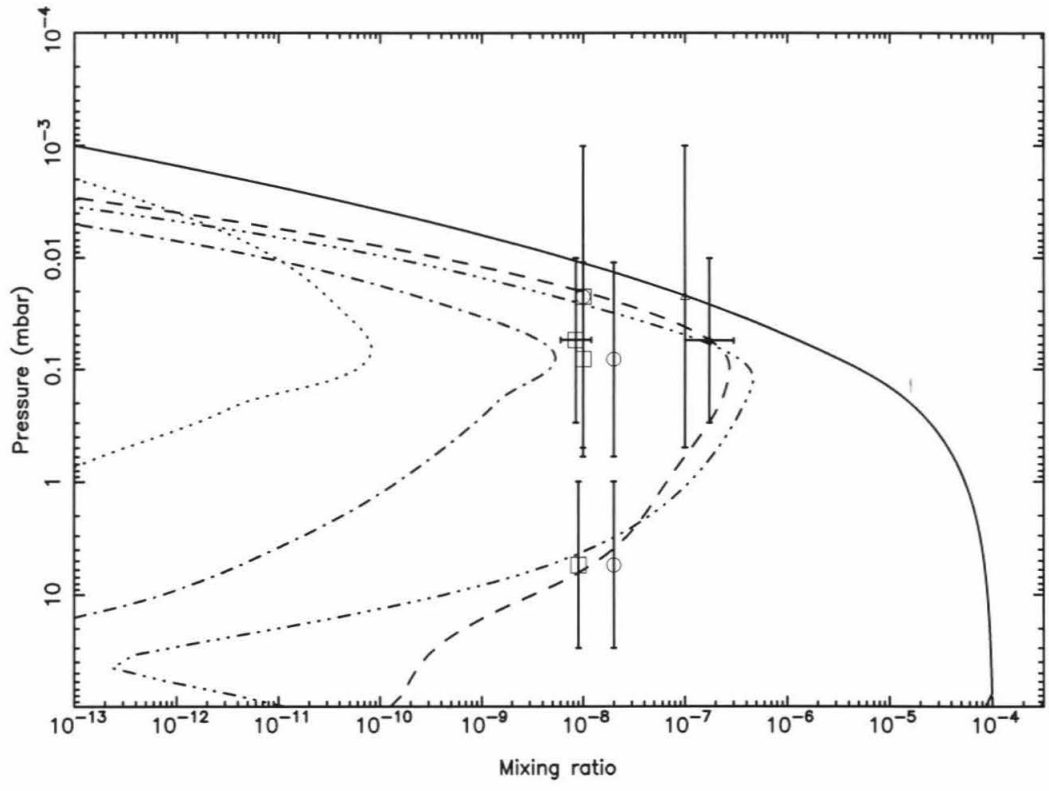

Figure 3-8. Same as Figure 3-6, but for Uranus.

The Neptune model is unusual for its eddy diffusion coefficient. Since the maximum photochemical production of C_2H_6 at the 10^{-4} mbar pressure level in our model gives an upper limit of $(1 - 2) \times 10^{-6}$ for the C_2H_6 mixing ratio at that altitude, the Voyager IRIS observation of $f(C_2H_6) = (1 - 4) \times 10^{-6}$ from 0.1 to 1.0 mbar [*Bézard et al.,* 1991] is hard to explain unless there is an extra source of C_2H_6 in the lower atmosphere or an extremely high rate of eddy mixing throughout the stratosphere [see *Romani et al.*, 1993; *Bishop et al.*, 1998]. The cold trap by C_2H_6 condensation in the tropopause region of Neptune would render extra sources ineffectual. *Romani et al.* [1993] tested different forms for K and were able to fit the IRIS observation with *K*

profiles having relatively high values in the upper stratosphere (e.g., $K \geq 5 \times 10^7$ cm^2 s^{-1} for $p \leq 0.5$ mbar). We adopt this high eddy diffusion coefficient value from 0.5 to 10^{-4} mbar in our Neptune model and assume that the CH_4 mixing ratio is 2×10^{-4} at the tropopause. However, our models do not include the condensation calculations in the stratosphere.

We have assumed in our model that an additional source of Lyman α exists at Neptune. The enhanced Lyman α photon flux may be contributed by the diffusive scattering of solar Lyman α photons from hydrogen atoms in the interplanetary medium (IPM), as has been suggested by *Ajello* [1990], *Moses* [1991], and *Gladstone* [1993]. According to both Moses's and Gladstone's estimate, the background flux from the IPM is in the same order of magnitude as the direct Lyman α flux at the orbit of Neptune. The two Lyman α sources are assumed to be of comparable strength at the orbit of Neptune, which in our model is modeled with doubling Lyman α flux for CH_4 photodissociation. The C_2H_2 and C_2H_6 vertical mixing ratio profiles, calculated by increasing Lyman α radiation by a factor of 2, provide a good fit to the observations in Figure 3-9. In contrast, the direct solar Lyman α flux is obviously much larger than the diffusive Lyman α from IPM for Jupiter, Saturn, and Uranus. Therefore we consider only the direct solar flux in our Jupiter (Figure 3-6), Saturn (Figure 3-7), Titan (Figure 3-10), and Uranus (Figure 3-8) models.

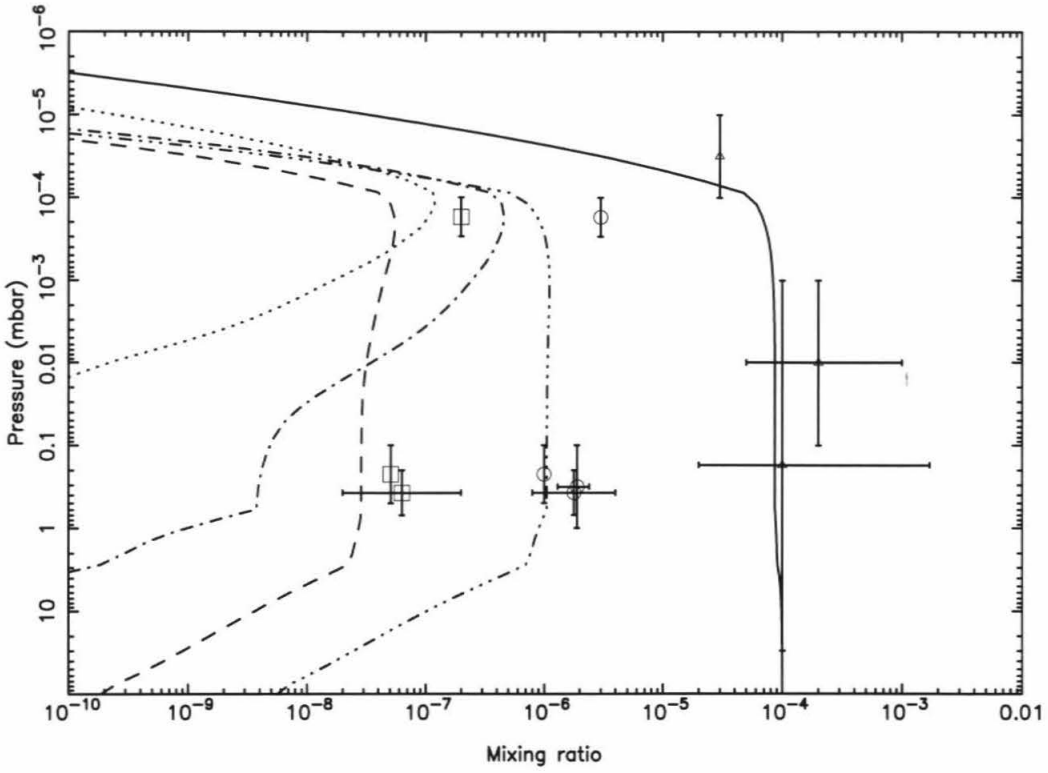

Figure 3-9. Same as Figure 3-6, but for Neptune.

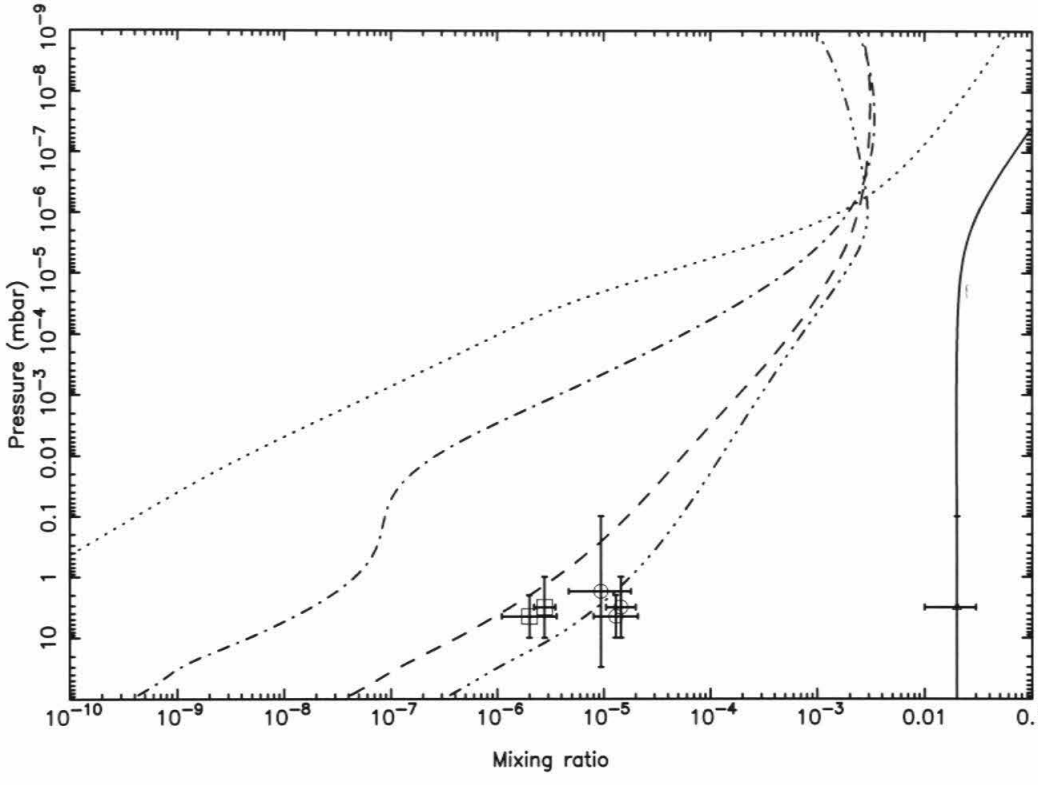

Figure 3-10. Same as Figure 3-6, but for Titan.

3.4. Sensitivity Tests

We test the sensitivities of our models to the temperature and eddy diffusion coefficients of Saturn and Neptune. The results are presented in Table 3-7. There are two types of sensitivity tests: (3.1) Varying temperatures by a 10 K increase or decrease at every pressure level and (3.2) varying eddy diffusion coefficients by a factor of 2 increase or decrease at every pressure level in the models. ISO observations and our normal model results using the "Modified Slagle" reaction rate constant are also listed in Table 3-7 for the purpose of comparison. We see only small changes in the CH_3 column abundances from shifting temperature profiles (± 10 K) in the stratospheres of Saturn and Neptune. This result is not surprising because our "Modified Slagle" rate constant extrapolation function (3.4) changes only 10% for the temperature rising or falling by 10 K near 150 K. Simultaneous changes of other chemical reactions with temperature may cancel this 10% effect. However, choosing rate constant functions by "Slagle" or "MacPherson" would cause larger temperature sensitivities at low temperatures (Figure 3-4).

The eddy diffusion coefficient parameterizes the vertical transport of the atmospheres of the outer solar system, determining the profiles of stable molecules such as CH_4 and C_2H_6. The effects of changing the eddy diffusion coefficient are shown by the last two cases in Table 3-7. The CH_3 column density calculated by enhancing bulk atmospheric eddy transport by a factor of 2 in the upper atmosphere of Saturn is increased by a factor 1.5 from the standard model. In this case, the CH_4 profile is pushed upward and the optical depth unity level is moved higher, resulting in methane photolysis occurring in low-density regions where CH_3 chemical loss is less effective. Naturally, the CH_3 radical abundance decreases as we divide the bulk

eddy diffusion coefficient by 2 and thus reduce the total column abundance of CH_4 above the tropopause. This effect may provide an explanation for the higher CH_3 column abundance, compared to Jupiter, in the atmosphere of Saturn, where the eddy diffusion coefficient above the 0.1 mbar pressure level is bigger than the value on Jupiter (Figure 3-3). The lowest CH_3 value in the atmosphere of Uranus (Table 3-6) is also consistent with this effect because the eddy diffusion coefficient of the stratosphere of Uranus is almost two orders of magnitude smaller than those in the other giant planets.

The Neptune model is the most sensitive to variations in the Lyman α radiation flux and to changes in chemical rate constants. We present four models for Neptune to test the sensitivity of out best fit model (Figure 3-9). Model 1 was carried out by assuming that all Lyman α flux comes from direct solar radiation. (Our best fit Neptune model assumes two times solar Lyman α flux at the orbit of Neptune.) Model 2 assumes that the adopted rate constant of key exchange reaction, $^1CH_2 + H_2 \rightarrow CH_3 + H$, is $k = 9.24 \times 10^{-11}$ cm^3 s^{-1} for $T < 150$ K, a value larger than the one used in our best fit model at low temperatures. Model 3 tests the recycling reaction (3.1), $H + CH_3 + M \rightarrow CH_4 + M$, by assuming three-body rate constant $k_0 = 2.52 \times 10^{-29}$ cm^6 s^{-1} at $T < 300$ K. This value was used by *Moses et al.* [2000a] in their Saturn model. Model 4 tests the key reaction for recycling C_2H_2, $H + C_2H_3 \rightarrow C_2H_2 + H_2$. The rate constant in model 4 is assumed to be 2.0×10^{-11} cm^3 s^{-1}, compared to the rate constant 7.5×10^{-11} cm^3 s^{-1} used in our best fit model (see Table 3-4; we should mention here that all the values in Table 3-4 were chosen to best fit the hydrocarbon observations in all five atmospheres of the outer solar system). The branching ratios of CH_4 photodissociation used by *Moses et al.* [2000a] (48% CH_3, 20% $^1CH_2$, 32% CH; based

on *Mordaunt et al.* [1993]) have also been tested in model 5.

The resultant stable hydrocarbon vertical profiles for models 1, 2, 3, 4, and 5 on Neptune are shown in Figures 3-11, 3-12a, 3-13a, 3-14a, and 3-15a, respectively. The model 2, 3, 4, and 5 results for Saturn (direct solar Lyman α flux test is not needed for Saturn) are shown in Figures 3-12b, 3-13b, 3-14b, and 3-15b, respectively. The CH_3 column abundances calculated from these test models for both Saturn and Neptune are shown in Table 3-8.

A comparison of Figure 3-11 with Figure 3-9 provides the motivation for our consideration of an enhanced Lyman α flux in our Neptune model due to scattering in the IPM. The weak solar radiation at the distance of Neptune (~ 30 AU), three orders of magnitude less than the solar radiation received by the Earth, reduces the generation of C2 or higher hydrocarbon molecules from CH_4 dissociation. Figure 3-9 shows very good agreement between our model results and the observations. Using only direct solar flux, as shown in Figure 3-11, marginally matches the lower limit of C_2H_2 and C_2H_6 error bars of the Voyager IRIS observation. However, the CH_3 column abundance value derived from model 1 (2.1×10^{13} cm^{-2}) fits the ISO observation better than our best fit hydrocarbon model (2.8×10^{13} cm^{-2}). Since the addition of more diffusive Lyman α radiation (exceeding a factor of 2) to our Neptune model would violate the ISO CH_3 observation, our models provide an independent confirmation of the magnitude of the background IPM radiation determined by *Gladstone* [1993].

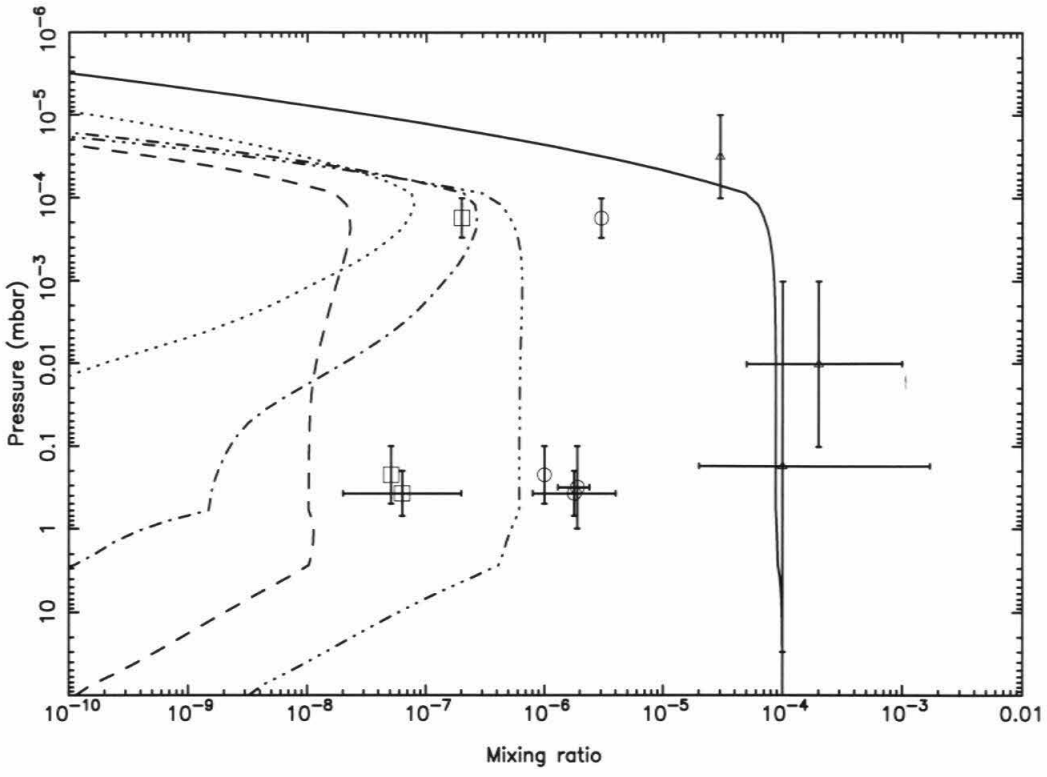

Figure 3-11. Model 1 for Neptune. The solar flux at Lyman α is 1/2 of our best fit model; the Lyman α comes only from direct solar radiation.

Models 2, 3, and 4 provide the chemical sensitivity studies for our best fit model. Three sensitivity tests of the key reactions listed in Table 3-4 affecting stable hydrocarbon products for Neptune are shown in Figures 3-12a, 3-13a, and 3-14a, and for Saturn are shown in Figures 3-12b, 3-13b, and 3-14b. It is obvious that these changed rate constants are more sensitive in the case of Neptune than in the case of Saturn. For example, changing the rate constant of the reaction $^1CH_2 + H_2 \rightarrow CH_3 + H$

Table 3-8. CH_3 Column Abundances in the Upper Atmospheres of Saturn and Neptune above 10 mbar for Saturn and 0.2 mbar for Neptune Derived From Four Test Models

CH_3 Column Abundances, cm^{-2}	Saturn	Neptune
Standard model	5.1×10^{13}	2.2×10^{13}
Model 1[a]	-	1.6×10^{13}
Model 2[b]	5.2×10^{13}	2.3×10^{13}
Model 3[c]	6.6×10^{13}	2.3×10^{13}
Model 4[d]	5.0×10^{13}	2.2×10^{13}
Model 5[e]	6.5×10^{13}	3.1×10^{13}

[a] Model 1 on Neptune uses the typical solar radiation flux. Our "best fit" Neptune model doubles solar flux at Lyman α.

[b] Model 2 adopts $k = 9.24 \times 10^{-11}$ cm^3 s^{-1} ($T < 150$ K) for the temperature-independent rate constant of $^1CH_2 + H_2 \rightarrow CH_3 + H$.

[c] Model 3 adopts $k_0 = 2.52 \times 10^{-29}$ cm^6 s^{-1} for the low-pressure limit rate constant at $T < 300$ K of $H + CH_3 + M \rightarrow CH_4 + M$.

[d] Model 4 adopts $k = 2.0 \times 10^{-11}$ cm^3 s^{-1} for the temperature-independent rate constant of $H + C_2H_3 \rightarrow C_2H_2 + H_2$.

[e] Model 5 adopts CH_4 branching ratios used by *Moses et al.* [2000a]. (48% CH_3, 20% $^1CH_2$, 32% CH; based on *Mordaunt et al.* [1993]).

from 9.24×10^{-11} cm^3 s^{-1} to 7.0×10^{-11} cm^3 s^{-1} for $T < 150$ K in the Saturn model provides only a ~10% decrease of C_2H_2 and C_2H_6 mixing ratios at 0.1 mbar. On the other hand, it gives a factor of 3 less C_2H_2 in the Neptune model at the same level. Changing only single key rate constants does not violate the model fit to C_2H_2 and

C_2H_6 observational values on Saturn, as is shown in Figures 3-12b, 3-13b, and 3-14b. However, such changes affect Neptune more significantly, especially for the C_2H_2 mixing ratio profile (see Figures 3-12a, 3-13a, and 3-14a). Because we use the same chemical model in the five atmospheres, each estimated kinetic value should be constrained to observations on all of these planets and the satellite. Therefore the chemical rate constants adjusted in our models are more acceptable than those derived only from a single atmospheric model. We notice that these newly estimated rate constants have larger influences on the C_2H_2 mixing ratio in the lower stratosphere of Neptune than the C_2H_6 abundance. In model 2, as shown in Figure 3-12a, increasing the reaction rate of $^1CH_2 + H_2 \rightarrow CH_3 + H$ provides significant depletion of C_2H_2 in the lower stratosphere of Neptune. In fact, the C_2H_2 mixing ratio fails to fit the lower limit of the Voyager IRIS error bar for an assumed increased rate constant of $k = 9.24 \times 10^{-11}$ cm^3 s^{-1}. This significant effect is not so obvious in the Jupiter or Saturn models.

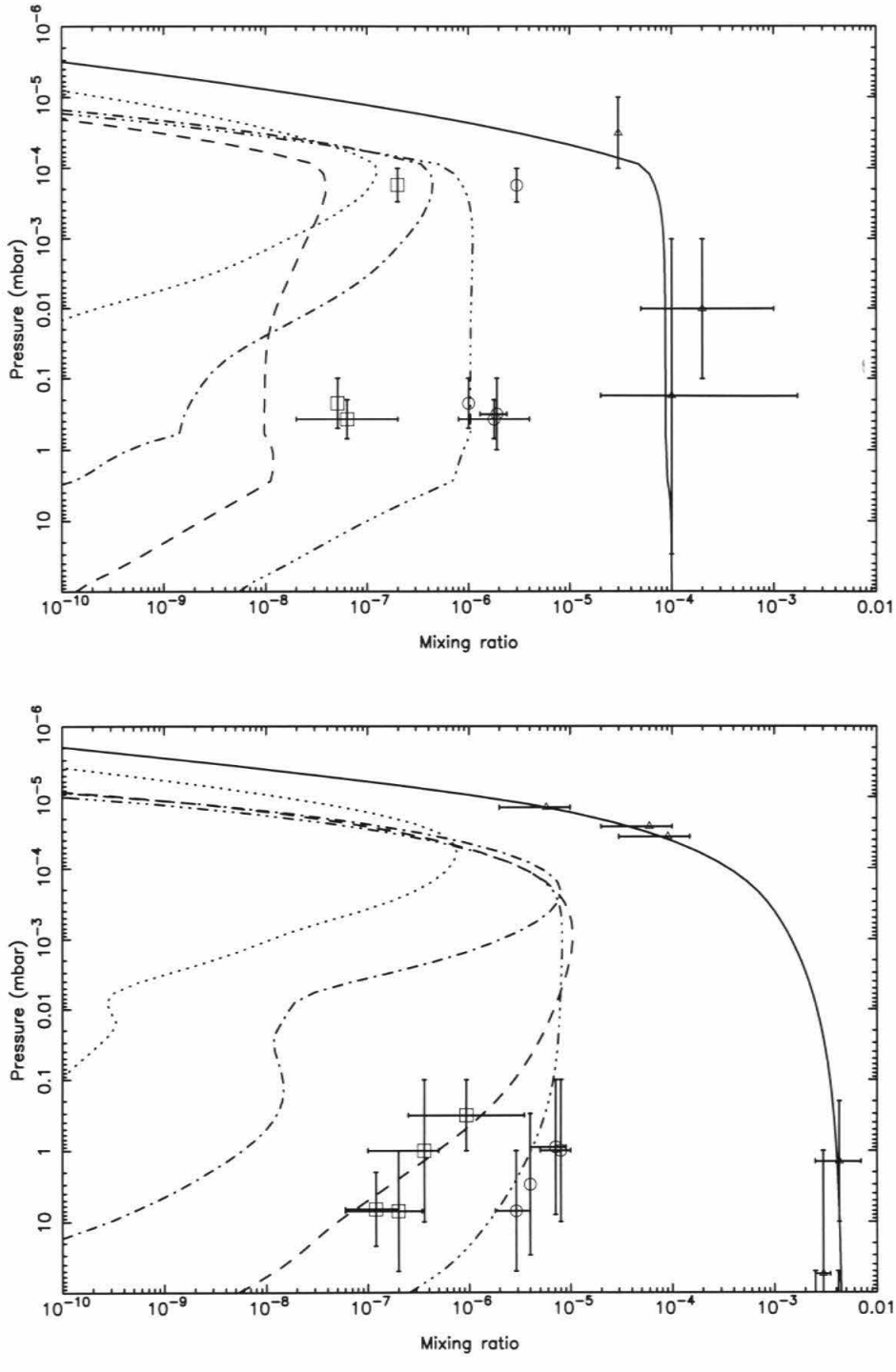

Figure 3-12. Model 2 for (a) Neptune, and (b) Saturn. The rate constant of $^1CH_2 + H_2 \rightarrow CH_3 + H$ is $k = 9.24 \times 10^{-11}$ cm^3 s^{-1} for all temperatures.

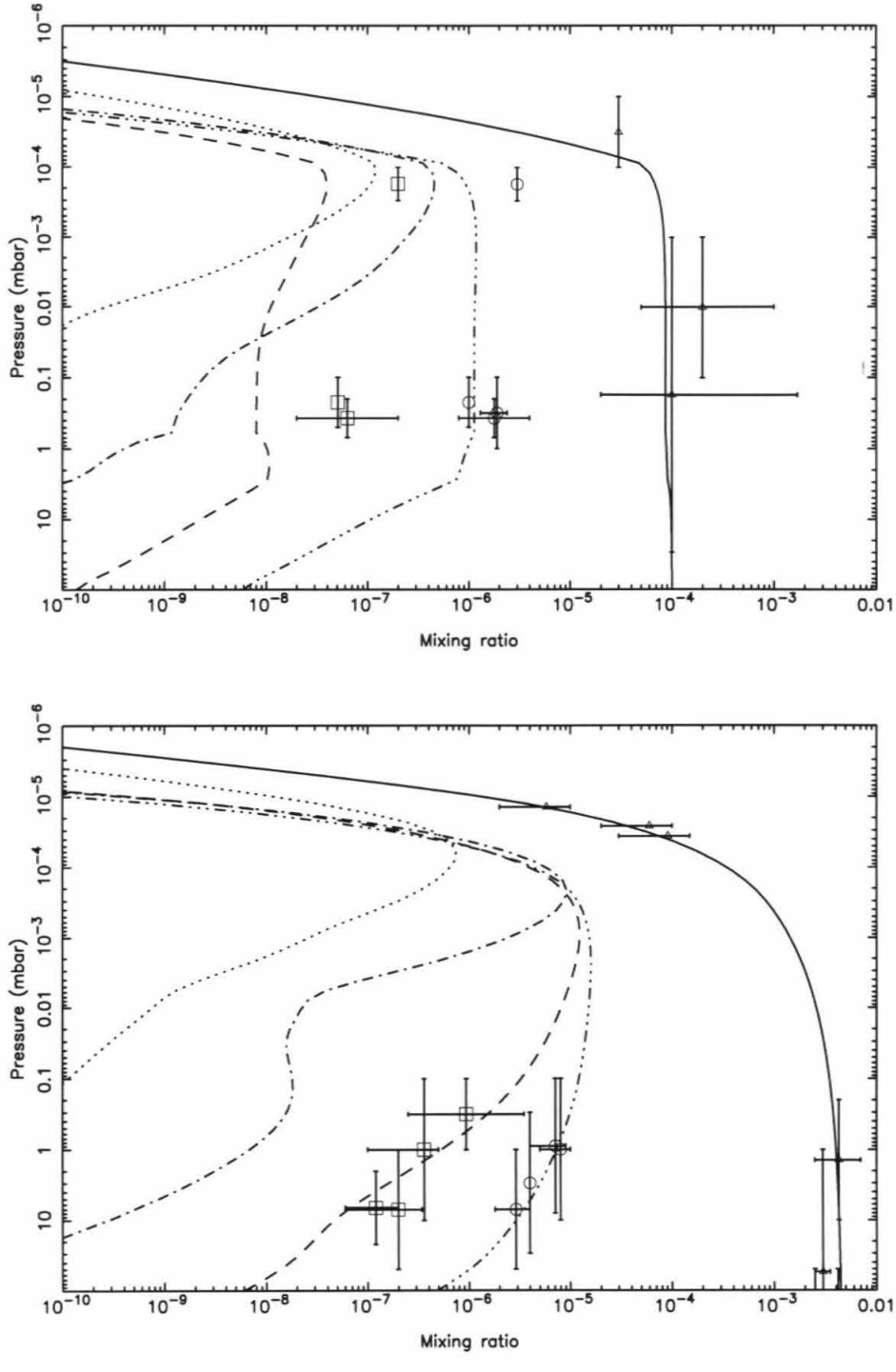

Figure 3-13. Model 3 for (a) Neptune, and (b) Saturn. The rate constant of H + CH_3 + M → CH_4 + M is $k_0 = 2.52 \times 10^{-29}$ cm^6 s^{-1} ($T < 300$ K).

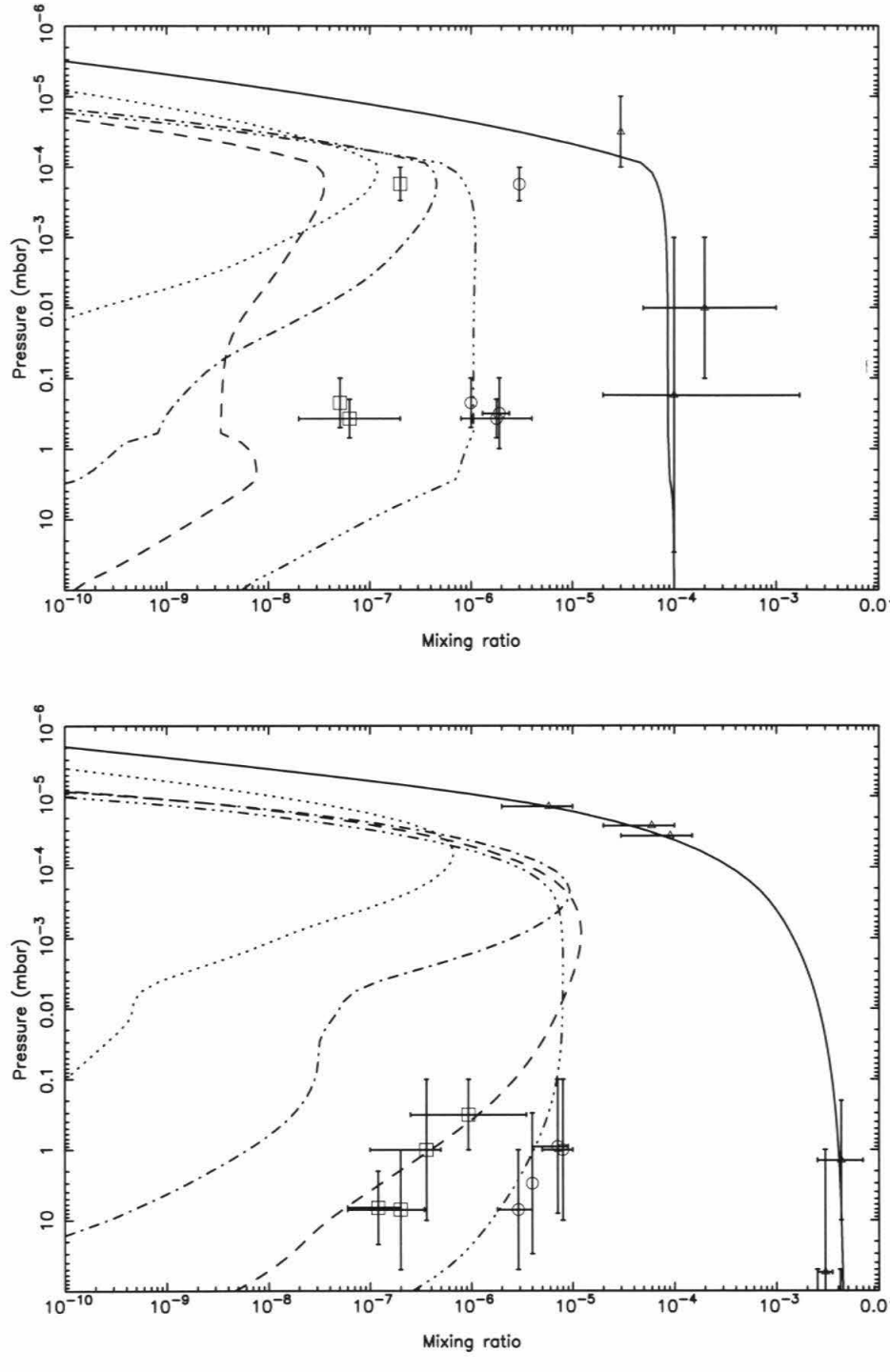

Figure 3-14. Model 4 for (a) Neptune, and (b) Saturn. The rate constant of $H + C_2H_3 \rightarrow C_2H_2 + H_2$ is $k = 2.0 \times 10^{-11}$ cm^3 s^{-1}.

Models 3 and 4, as shown in Figures 3-13a and 14a, respectively, demonstrate the sensitivity of the Neptune model to the reactions H + CH_3 + M→ CH_4 + M and H + C_2H_3 → C_2H_2 + H_2. Since these reactions still lack reliable experimental rate constants at low temperatures, our models, especially the Neptune model, may provide a constraint on the theoretical estimates of chemical kinetics.

Model 5 examines the influence of CH_4 branching ratios on our hydrocarbon models. The major difference between the *Slanger and Black* [1982] values and the *Mordaunt et al.* [1993] values is that the former lacks the CH_4 → CH_3 + H channel, and this channel is the major pathway for the other case. We replace the branching ratios by those adopted in *Moses et al.*'s [2000a] model in our sensitivity test model 5. According to Figure 3-15b and the last row in Table 3-8, there are only slight changes between the two sets of branching ratios on Saturn for C2 hydrocarbon and CH_3 column abundances. However, there is a significant decrease for C_2H_2 by adopting Mordaunt et al. branching ratios for Neptune (Figure 3-15a).

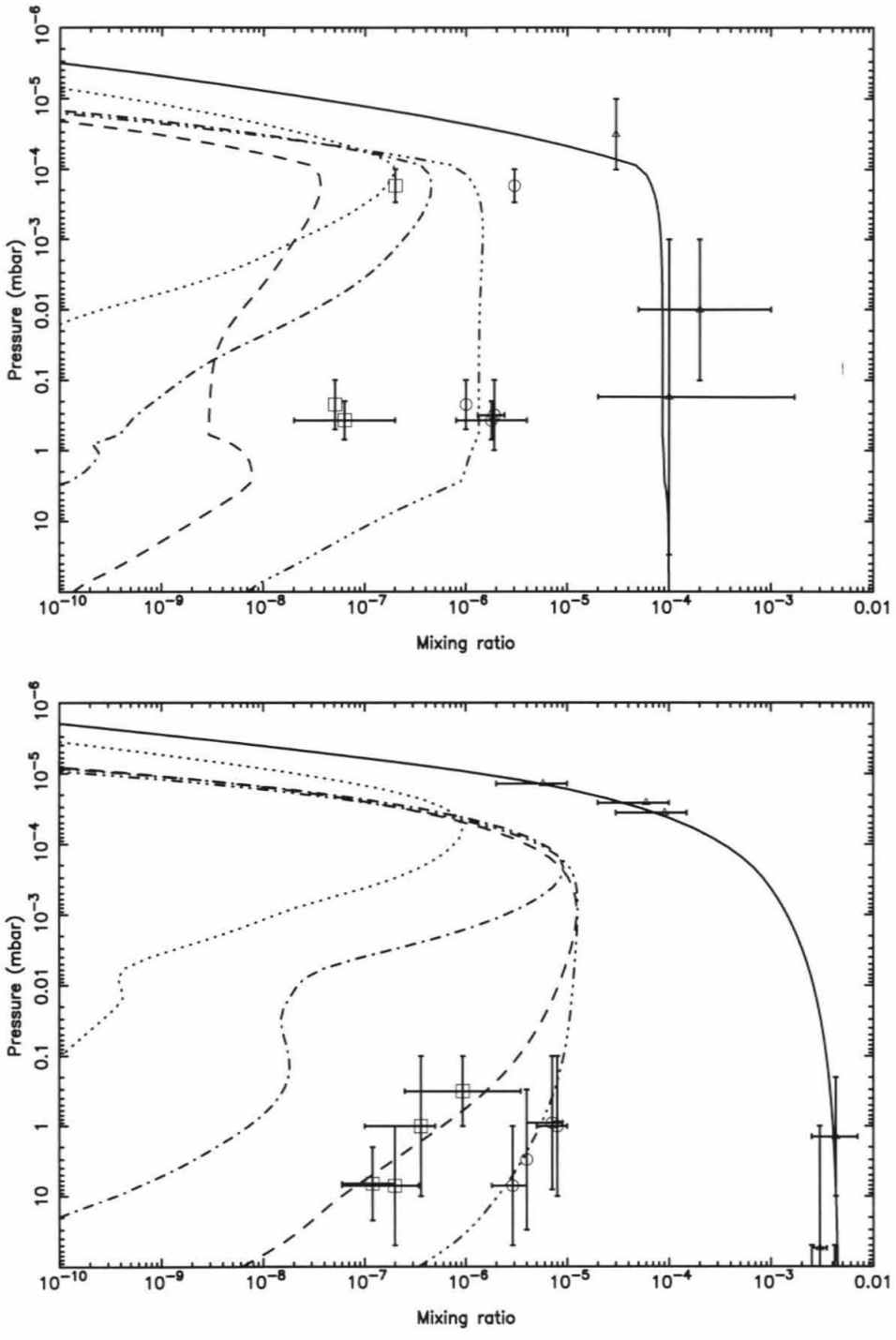

Figure 3-15. Model 5 for (a) Neptune, and (b) Saturn. The CH_4 branching ratios are 48% CH_3, 20% $^1CH_2$, 32% CH.

3.5. Conclusions

Generalized one-dimensional photochemical models using a single chemical reaction set have been applied to the atmospheres of the giant planets and Titan for the first time. We adopt the most complete and recent updated set of hydrocarbon photochemical reactions and cross sections from *Moses et al.* [2000a], except that we test and modify some rate constants and methane photolysis branching ratios. The key reactions that we estimate are $CH_3 + CH_3 + M \rightarrow C_2H_6 + M$, $H + CH_3 + M \rightarrow CH_4 + M$, and $H + C_2H_3 \rightarrow C_2H_2 + H_2$. In this article we suggest a modified formula for the rate coefficient of the recombination reaction $CH_3 + CH_3 + M \rightarrow C_2H_6 + M$ at low temperatures, and we also evaluate the rate constants of other key reactions. We calculate the mixing ratio of hydrocarbon species at each altitude level and determine the total column concentrations of methyl radicals in the stratospheres of Jupiter, Saturn, Uranus, Neptune and Titan. All models are distinguished by their physical properties, such as distance to the Sun and gravity, and their atmospheric characteristics, such as temperature profile and vertical eddy mixing coefficients. The Lyman α flux enhancement at the Neptune's orbit has also been considered.

Our models provide reasonable results compared to the ISO/SWS observations of CH_3 on both Saturn and Neptune. Our modified rate constant formula for the reaction $CH_3 + CH_3 + M \rightarrow C_2H_6 + M$ at low temperatures, incorporated with other estimated rate constants (Table 3-4), also provides good agreement to observations of the stable hydrocarbon species. However, reliable experimental low-temperature kinetics data for most of the reactions listed in Table 3-4 are still lacking. This limitation should provide strong motivation for future laboratory studies. Our prediction for low CH_3 concentrations in the upper stratosphere of Uranus, and a high

CH_3 abundance on Titan, can be checked by future observations.

Chapter 4

Submillimeter Detection of PH_3 in Jupiter and Vertical Mixing in Upper Troposphere

4.1. Introduction

According to the thermodynamic equilibrium model for the Jovian atmosphere, phosphine (PH_3) should be produced at appreciable concentrations only at the relatively high temperatures ($\geq$ 500K) of the deep troposphere [Prinn and Lewis 1975]. In the colder upper troposphere ($\leq$ 150K), the PH_3 abundance is predicted to decrease rapidly as photochemical reactions take place and solid phosphorus precipitates are formed [Fegley and Lodders 1994, Borunov *et al.* 1995]. The presence of observable quantities of PH_3 in the absence of a stratospheric source therefore reveals the existence of rapid vertical mixing from deeper, warmer levels, as suggested by Prinn and Lewis. As a result, observations of PH_3 can provide constraints on photochemical/transport models, making this molecule an important chemical and dynamical probe of the atmosphere of giant planets, e.g. Jupiter and Saturn. However, because of difficulties in inverting infrared spectra, this potential has yet to be fully exploited.

PH_3 has been detected at infrared wavelengths in both Jupiter and Saturn [Ridgway *et al.* 1976, Bregman *et al.* 1975] for decades. Unfortunately, the large numbers of other

spectral features present at these wavelengths, combined with other complicating factors such as scattering by clouds, make retrieval of the vertical PH_3 profile from infrared observations difficult. Weisstein and Serabyn [1994] have previously discussed the merits of wideband millimeter/submillimeter spectroscopy as a complement to existing infrared studies. Using a Fourier transform spectrometer (FTS), Weisstein and Serabyn detected the J=1-0 PH_3 line in Saturn at 267 GHz (1120 μm) but not in Jupiter, indicating a significantly lower PH_3 abundance in the latter. Capitalizing on the increase of line strength with increasing rotational quantum number J, we recently re-observed Jupiter at the 800.5 GHz frequency of the J=3-2 line. (The J=2-1 transition at 533.8 GHz is obscured by telluric H_2O.) These new high-frequency FTS measurements have succeeded in detecting a rotational PH_3 line on Jupiter, allowing a direct determination of the PH_3 mixing ratio and vertical distribution from the observed lineshape.

The retrieval of PH_3 vertical abundance profile by using radiative transfer calculation provides a near solar mixing ratio, from deep atmosphere to upper troposphere. Prinn and Lewis [1975] pointed out that an eddy diffusion coefficient of at least 10^6 cm^2 sec^{-1} below tropopause region is necessary for the upward transport of PH_3 to compensate rapid photochemical destruction. Therefore, the distribution of PH_3 is extremely sensitive to the rate of vertical transport in the upper troposphere, and the chemical lifetime of PH_3 is thus similar to the time constant for transport. In other words, PH_3 is a good trace element in determining eddy diffusion coefficient in upper troposphere for the typical 1-D photochemical model. Solving the continuity equation of PH_3 by equating transport flux and chemical depletion by both UV photons and chemical radicals at different altitudes leads to a vertical distribution of the species. However, since

the PH_3 photodissociation wavelengths are strongly overlapping with NH_3 from 160 to 220 nm, and the scattering effects of solar UV radiation in the denser troposphere become important, the photochemical model should be more complex in the troposphere than in the stratosphere, and needs to be calculated more carefully. Solar UV radiation attenuated by hydrocarbons (CH_4, C_2H_2, C_2H_6, etc.) and NH_3 absorption, Rayleigh scattering (H_2 and He), and dust/cloud scattering, must be implemented. We will discuss the details in the following.

Except for the PH_3 as a dynamical tracer in the Jovian upper troposphere, NH_3 may become another important trace element for its abundant mixing ratios. According to the NH_3 observations [Griffith *et al.*, 1993] below the tropopause on Jupiter, however, NH_3 concentration vertical profile seems to fall on the saturated vapor pressure mixing ratios line from the cloud top to about 200 mbar pressure level. The excess NH_3 above the saturation line is more likely to be condensed and forms possibly the aerosol layer at and above the cloud top level. Thus, the higher limit for eddy diffusion coefficient in this region is hard to determine by modeling NH_3. We can only test the lower limit of eddy diffusion coefficient by increasing its value until the NH_3 mixing ratios reach the saturation profile.

This chapter will be concentrated on the retrieval of PH_3 concentrations in the upper troposphere of Jupiter and the photochemical-dynamical modeling of the result. I should point out that all observations were done by Serabyn and Weisstein in 1994. I have taken over this project since 1996 for finalizing the following work. Section 2 will briefly describe the observations. The manuscript of this section was mostly provided by Serabyn and Weisstein.

4.2. Observations

Serabyn and Weisstein observed the submillimeter spectrum of Jupiter at the Caltech Submillimeter Observatory (CSO) using the FTS described in Serabyn and Weisstein [1996] on June 21-24, 1994 (UT). The resulting submillimeter spectra of Jupiter (and Saturn) have been previously presented as part of a Jovian planet submillimeter line search by Weisstein and Serabyn [1996]. This section will concentrate instead on observations of Jupiter in the highest frequency filter, which contains the PH_3 3-2 rotational line. For the June 1994 observations, the instrumental field of view was defined by a 20" Winston cone, and the spectral resolution was 199 MHz. The size of Jupiter during the observations was 41.3" × 38.6".

Eight pairs of FTS scans were made, both centered on Jupiter's disk and off the planet on blank sky. Further details on the instrumental setup used for these observations and on the calibration procedure can be found in Weisstein and Serabyn [1996]. After conversion of the 350 μm Jupiter spectrum to the T^*_A antenna temperature scale, the resulting spectrum was divided by a spectrum of the Moon obtained over a similar airmass range. The Jupiter/Moon spectrum, shown in Figure 4-1, exhibits a smooth continuum and strong absorption feature near 800.5 GHz corresponding to the J=3-2 transition of PH_3. The full-width at half maximum (FWHM) of the prominent PH_3 line is 9.6 GHz, and the depth at line center is 20%. The negative slope apparent in the continuum of Figure 4-1 may be intrinsic to Jupiter, but may also be produced by a falloff in the telescope efficiency at high frequencies, and so will not be discussed further. Small residual ozone features from the Earth's atmosphere not removed by the Moon division

have been ticked for clarity, but do not adversely affect the spectrum.

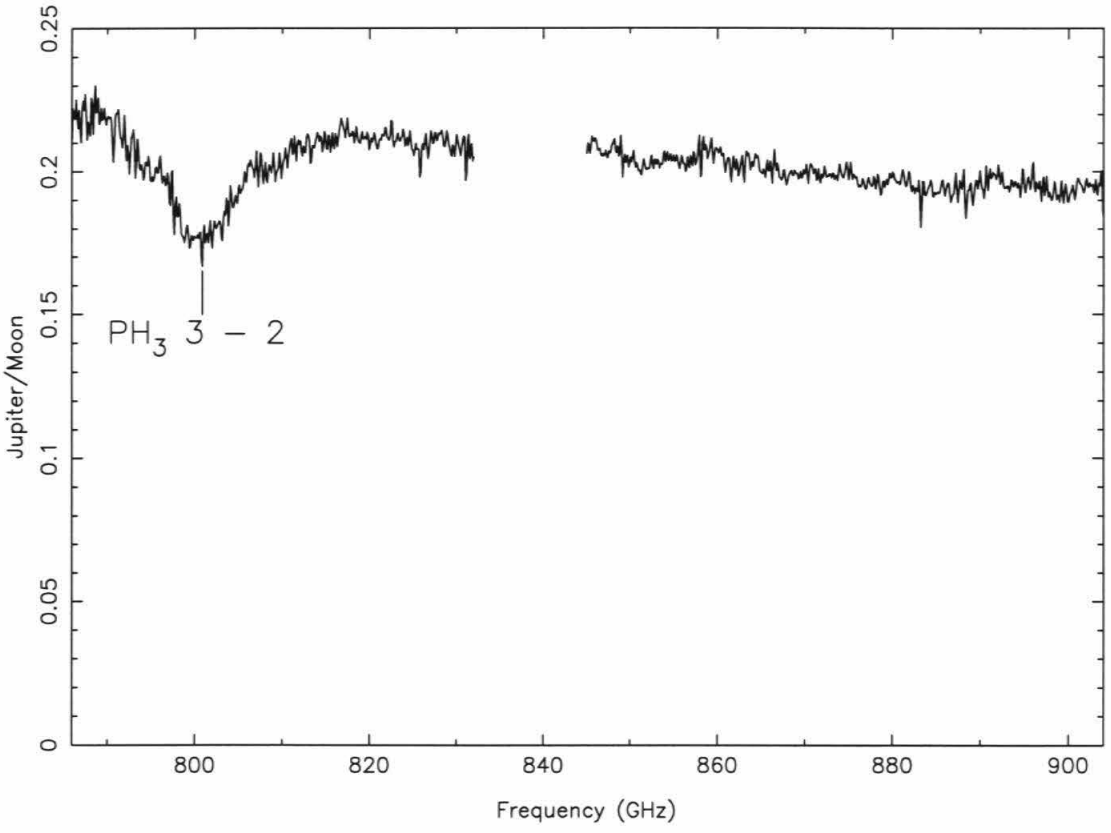

Figure 4-1. Ratio of Jupiter/Moon spectra (both in uncalibrated T_A^* units). The J=3-2 PH_3 transition is marked, and a number of residual O_3 lines not removed by the division are ticked. A portion of the spectrum near 835 GHz has been blanked where it is contaminated by a terrestrial O_2 feature.

4.2.1. Continuum

Because weather prevented completion of beam coupling measurements necessary to directly convert our observations to an absolute brightness temperature scale, we instead performed the scaling from the Jupiter/Moon ratio spectrum using the continuum level provided by a Jovian planet radiative transfer model. The details of this model are given in Weisstein and Serabyn [1994, 1996]. The whole-disk radiative transfer calculation is done using the Planck law, and the output intensity is converted to the equivalent blackbody "brightness temperature", henceforth denoted T_B. Because the spatial resolution of our observations was roughly half the planetary diameter, limb darkening reduced beam-weighted whole-disk brightness temperature by only $\leq$ 2K compared to a simple 1-D model. The pressure-temperature (p-T) profile was obtained from Lindal *et al.* [1981] and adiabatically extrapolated downward. To investigate the consequences of a possible deviation in the average Jupiter p-T profile from the obtained by Lindal, we also computed model spectra in which the temperature at each pressure level (from the top of the atmosphere down to the deepest pressure level probed by Lindal *et al.* 1981) were shifted by $\pm$ 5K. These profiles gave whole-disk brightness temperatures, which varied by < 2K from the nominal case. The consequences of this small shift on PH_3 inversions are discussed in the following section.

We next fit a first-order polynomial baseline to the continuum in Figure 4-1, and a second-order baseline to the synthetic spectrum given by our model, after which we rescaled the observed spectrum by the ratio of the baseline polynomials so that the continuum level of the data was forced to match that of the model. This procedure

preserves the line/continuum ratio, since beam coupling affects the spectrum at each frequency by a given scaling factor, which is independent of the relative importance of line absorption and continuum emission at that frequency. The resulting scaled spectrum (now with a model-derived continuum temperature) is shown in Figure 4-2 on an expanded horizontal scale, together with several fits to the PH_3 line.

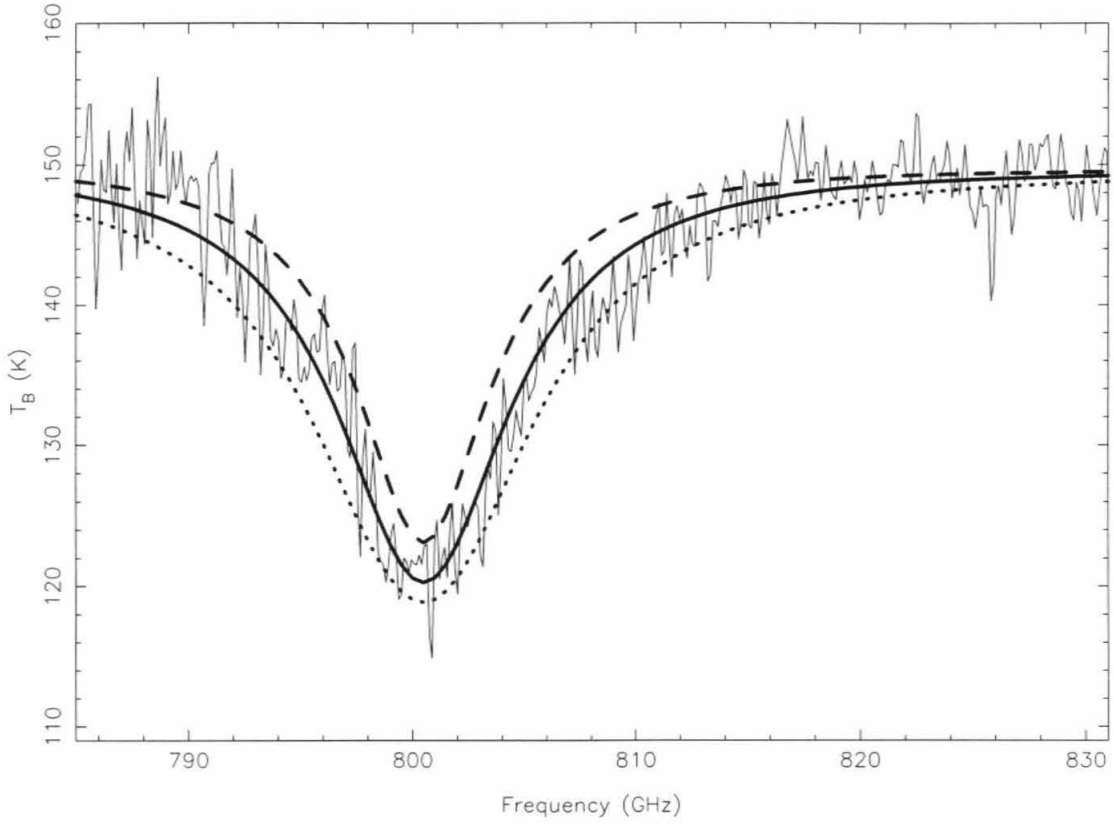

Figure 4-2. Jupiter spectrum converted to brightness temperature units using a radiative transfer model. Models for 0.3 (dashed line), 0.5 (solid line), and 0.8 (dotted line) ppmv PH_3 assuming a constant mixing ratio and cutoff pressure p_c = 250 mbar are overlaid.

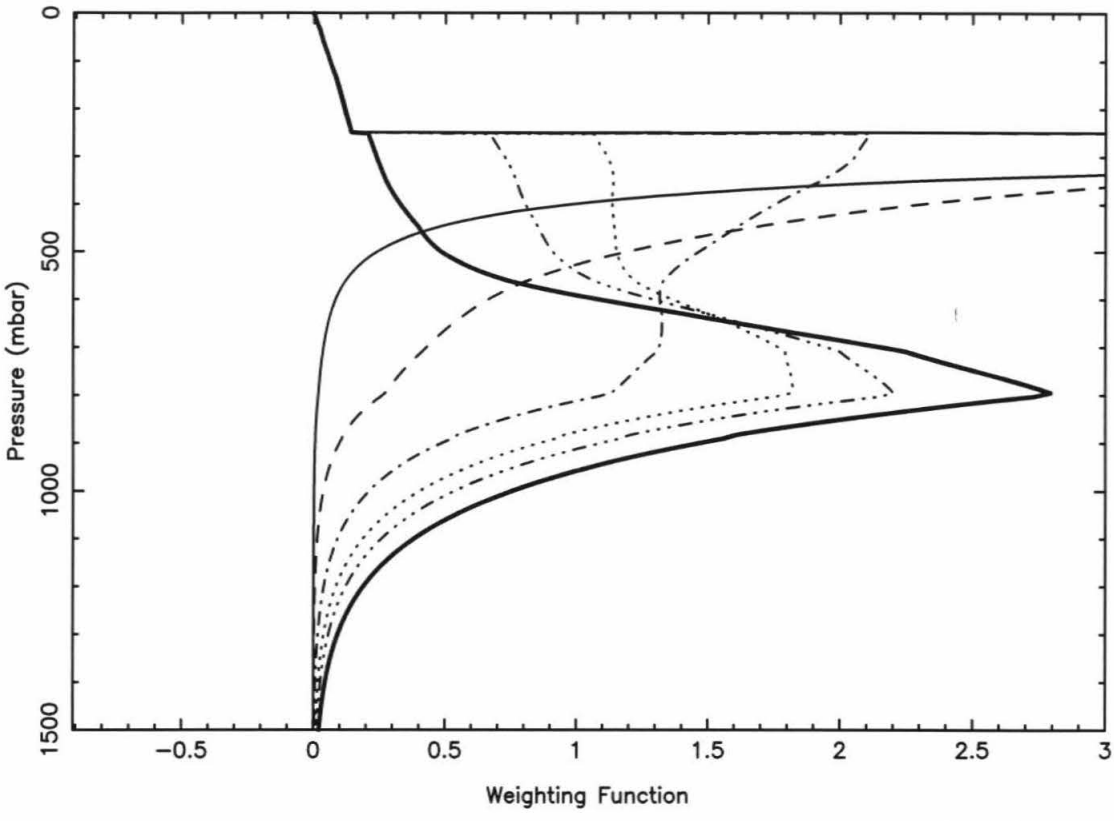

Figure 4-3. Jupiter weighting functions for various frequency offsets from the PH_3 line center. (Thin solid line: ν = 800.5 GHz, $\Delta\nu$ = 0; Dashed line: ν = 802.9 GHz, $\Delta\nu = 0.5\alpha$; Dash-dot line: ν = 805.3 GHz, $\Delta\nu = 1.0\alpha$; Dotted line: ν = 807.7 GHz, $\Delta\nu = 1.5\alpha$; Dash-dot-dot-dot line: ν = 810.1 GHz, $\Delta\nu = 2.0\alpha$; Thick solid line: ν = 829.3 GHz, $\Delta\nu = 6.0\alpha$) The upper peak is mostly due to PH_3, and the lower peak is mostly due to NH_3 continuum emission.

The continuum weighting function determines the deepest level to which our observations probe. As shown in Figure 4-3, continuum emission 6 half-widths away from the PH_3 line center (6α, where α is the half-width at half-maximum) has a weighting function, which peaks near 800 mbar. Continuum contributions to the

weighting function extend to a maximum pressure of ~ 1200 mbar, which is the thus deepest level to which our observations are sensitive. The strong PH_3 line therefore arises from tropospheric absorption at $p < 1200$ mbar.

4.2.2. Stratospheric PH_3

We now discuss modeling of the PH_3 line itself. No emission core is seen in our 199 MHz resolution spectrum (Figure 4-2), demonstrating that little or no PH_3 is present above the cold trap (~ 140 mbar) in Jupiter. The lack of an emission core places a 3σ upper limit of ~ 60 ppb on the stratospheric PH_3 mixing ratio (assumed to be constant) in Jupiter. The extreme small abundance is consistent with the upper tropospheric depletion inferred by Encrenaz *et al.* [1978, 1980] and Tokunaga *et al.* [1979]. This result is virtually independent of the PH_3 mixing ratio profile used to match the tropospheric absorption line. It is also consistent with the lack of an observed line core in high-resolution 267 GHz heterodyne spectra by Lellouch *et al.* [1984] and confirmed by our own heterodyne measurements at the CSO. Other recent observations, like UV spectra by HST Faint Object Spectrograph [Edgington *et al.* 1998], also agree with the lack of PH_3 in Jovian stratosphere.

4.2.3. Tropospheric PH_3

The J=3-2 PH_3 line is a triplet composed of K=0, 1, and 2 levels. These three

components are comparable in line strength and are separated by a total of ~ 100 MHz [Pickett *et al.* 1992], a very small offset compared to the observed line width. Laboratory measurements of the pressure broadening coefficients for the J=3-2 triplet in hydrogen-helium atmospheres do not exist, nor are there any published determinations of the temperature exponent (n in the expression $\Delta\nu \propto (T_0/T)^n$) for any PH_3 rotational lines. Our model therefore uses the pressure broadening coefficient of the J=1-0 transition measured at room temperature by Pickett *et al.* [1981], a Lorentzian lineshape, and, as in Weisstein and Serabyn [1994], assumes the same temperature exponent as for NH_3, n=0.67. (The only extant laboratory measurements are for vibrational transitions at 1950-2150 cm^{-1} [Levy *et al.* 1994] and suggest n=0.73.)

Depletion of PH_3 above the tropopause level on Jupiter has been shown by the lack of emission core in the spectrum (Figure 4-2). We confidentially conclude that most PH_3 absorption features come from the troposphere. To retrieve the vertical distribution of PH_3 in the Jovian troposphere, we must assume certain vertical profiles and then calculate the synthetic spectrum for comparison with the measured spectrum shown in Figure 4-2. In the next section, we will discuss the details of PH_3 vertical profile retrieval.

4.3. Data Analysis

In the absence of an emission core, we now focus on retrieving the PH_3 abundance below the tropopause, for pressure ≥ 100 mbar. For the purpose of creating synthetic spectra for comparison with observations, we adopt a simple model for the vertical distribution of the PH_3 mixing ratio which increases linearly from zero abundance as the pressure increases from p_0 to p_c ($p_0 < p_c$), and constrains the mixing ratio q to remain constant for pressure ≥ p_c. For pressure < p_0, PH_3 is assumed 0. Since there may be no unique choice for the PH_3 vertical profile, we explore the complete set of parameters (p_0, p_c, q) by generating their synthetic spectra and statistically comparing the synthetic spectra with the observed spectrum. The combination of parameters leading to synthetic spectra falling within 3σ (99.73%) gaussian confidence level will be identified as plausible approximations to the real PH_3 distribution in the troposphere of Jupiter.

According to the photochemical models, PH_3 is expected to fall off to zero near the top of the troposphere due to the dissociation by solar UV radiation [Kaye and Strobel, 1984], or by chemical destruction. Weisstein presents the three parameters distribution described above as the "Model B" in his thesis [1996]. This is a more general PH_3 profile that allows a more gradual decrease above the critical level p_c than a simple rectangular distribution model ("Model A").

The submillimeter $J = 3\text{-}2$ observation guides the feasible range of the parameters. We have concluded that most PH_3 absorption features come from the troposphere by observing Figure 4-2, so that p_0 is > 100 mbar. The lower limit of the minimum of the observed spectrum (Figure 4-2) below 130 K also indicates p_0 < 400 mbar. In Figure 4-3,

one sees that, near the PH_3 center ($\Delta\nu = 0$), optical depth unity occurs high in the troposphere, while away from the line center ($\Delta\nu = 6\alpha$), the weighting function is composed almost entirely of the NH_3 contribution. The near line wings, therefore, contain the most useful information about the vertical distribution of PH_3 in Jovian troposphere, and inversion of the broad PH_3 line is most sensitive to PH_3 arising from $p < 600$ mbar. Therefore, we explore values for p_c ranging from the tropopause (100 mbar) down to ~ 500 mbar pressure level. To estimate a plausible range for the deep mixing ratio q, we assumed $p_0 = p_c$ for simplicity, and did simultaneous nonlinear least squares inversion for q and p_c, which yielded a best fit of $q = 0.55$ ppmv and $p_c = 250$ mbar for the nominal Lindal *et al.* [1981] pressure-temperature troposphere profile. To examine the sensitivity of this fit to the PH_3 mixing ratio, models were also run for $q = 0.30$ ppmv and 0.8 ppmv, keeping $p_c = 250$ mbar (see Figure 4-2 for the resulting synthetic spectra). These models constrain the PH_3 mixing ratio to within an estimated uncertainty of ~ 0.10 ppmv. On the basis of these results, we explored the parameter range for q from 0.4 to 0.75 ppmv. It will be seen later that the best-fit parameters fall comfortably within the search range for p_0, p_c, and q.

We generated 30,000 synthetic spectra, covering every combination of p_0, p_c, and q in the range described above (p_0, p_c, q = 100 – 400 mbar, 100 – 500 mbar, 0.4 – 0.75 ppmv, respectively. p_0 and p_c both stepped in increments of 10 mbar, q stepped in increments of 0.1 ppmv). We used a detailed statistical computation between the simulated and observed spectra to identify the best combination of parameters for simulating the PH_3 vertical distribution.

χ^2 test has been used to perform the statistical comparison between the observation (observed spectrum) and the predicted calculations (synthetic spectra). We define the observed spectrum $T_0(\nu_i)$, as shown in Figure 4-2, and the synthetic spectra generated using our radiative transfer code $T_s(\nu_i)$ by applying parameter combinations. The number of degrees of freedom N = 47 for there being 47 wavelength channels of our observation. The normalized standard deviation σ for each combination of the parameters is defined by the average of squared spectrum difference and the number of degrees of freedom,

$$\sigma^2 = \sum_{i=1}^{N} \frac{(T_s(\nu_i) - T_0(\nu_i))^2}{N}. \tag{4.1}$$

Thus, a normalized χ^2 value is obtained by the following formula,

$$\chi^2 = \sum_{i=1}^{N} \frac{(T_s(\nu_i) - T_0(\nu_i))^2}{\sigma^2}. \tag{4.2}$$

The χ^2 value is a measure of the spread of the parameter combinations. If the synthetic spectrum agreed exactly with the observed spectrum, $T_s(\nu_i) = T_0(\nu_i)$, then $\chi^2 = 0$. Larger values of χ^2 indicate larger deviations than expected from the assumed distribution.

According to the formula described above, we calculate the 26 channels centered at 800.5 GHz, instead of the total 47 channels. The purpose for choosing the 26 "center" bins with $T_B < 150K$ is to emphasize the weightings for the PH_3 falloff region in the upper troposphere, where PH_3 abundance is much more sensitive to the photochemical model than in the lower troposphere. We thus obtain the upper limit for normalized χ^2 value ~ 3.02 for confidence level 99.73% within 3σ of the χ^2 Gaussian distribution. The

combinations of parameters p_0, p_c, and q satisfying $\chi^2 < 3.02$ are shown in Table 4-1, and all the corresponding PH_3 vertical profiles are shown in Figure 4-4. The synthetic spectra for these combinations of parameters are also shown in accordance with the observed spectrum in Figure 4-5.

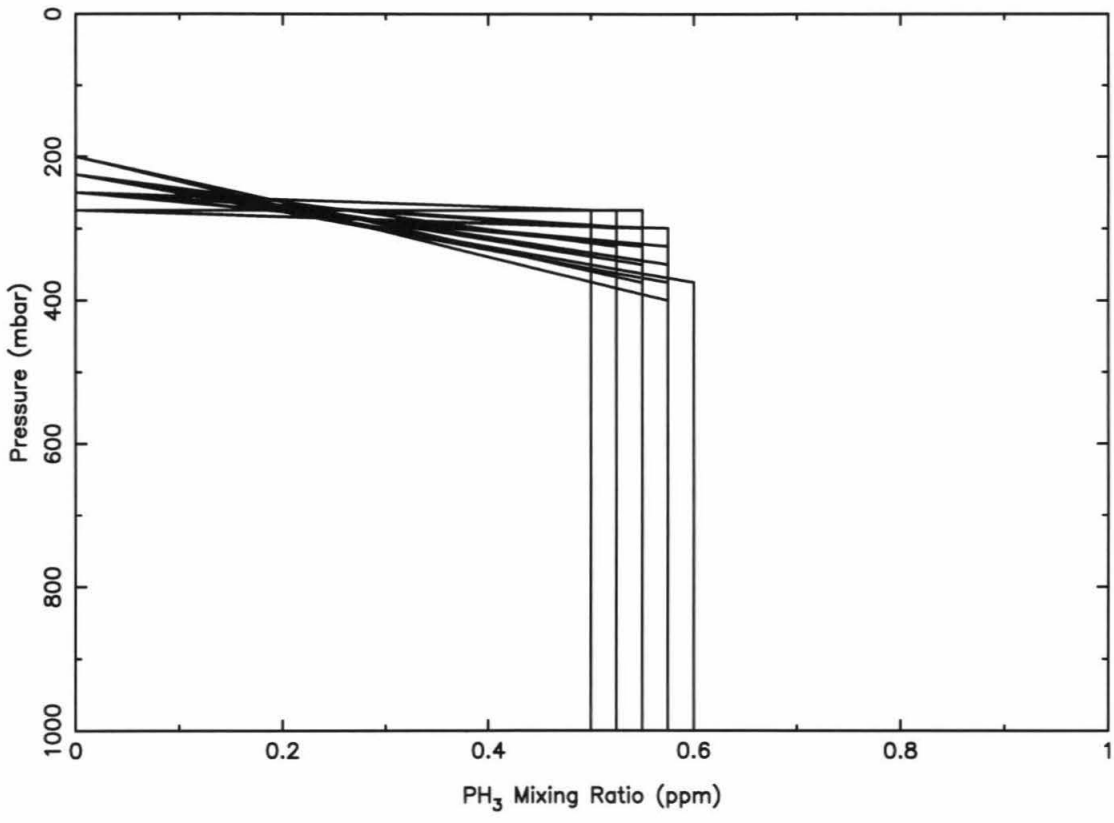

Figure 4-4. PH_3 vertical profiles suggested by radiative transfer model by adopting Model B for the confidence level within 90% ($\chi 2 \leq 3.02$). Model spectra computed using these profiles are shown in Figure 4-5. The parameters for these profiles are shown in Table 4-1.

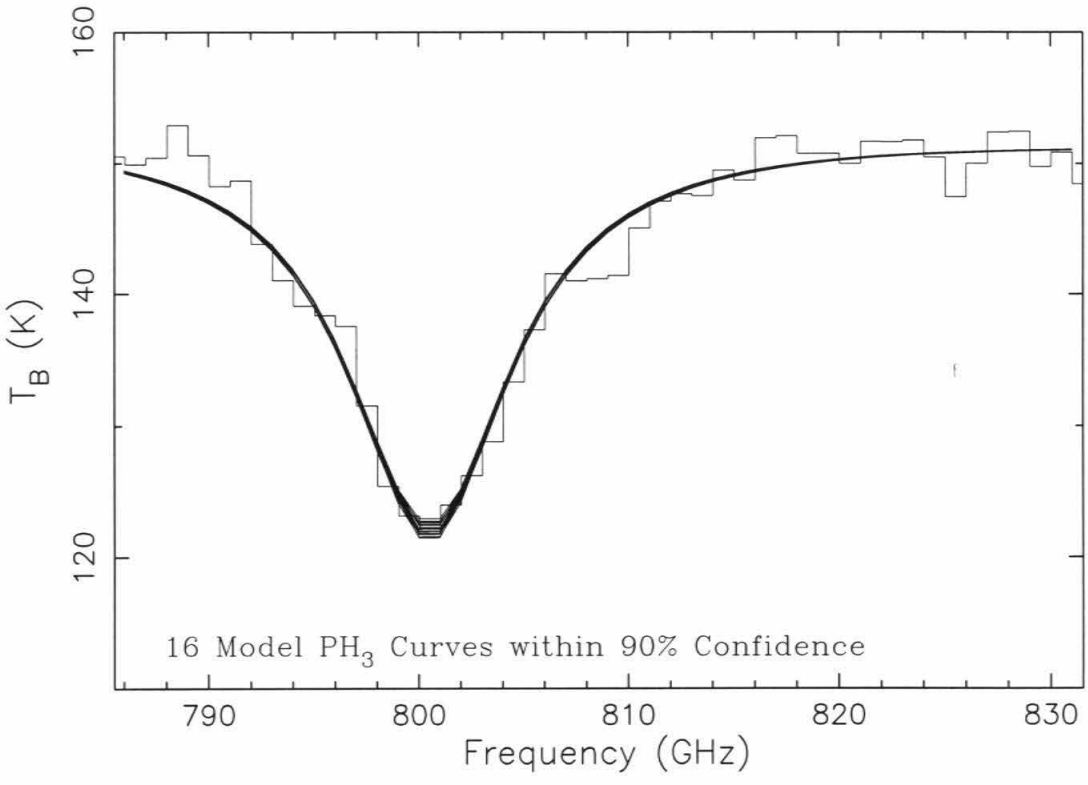

Figure 4-5. Model spectra obtained using the PH_3 profiles of Figure 4-4. The spectrum from Figure 4-2 is superposed for comparison. The polynomial PH_3 model fits the data to within confidence level 90%.

Table 4-1. Parameter set of PH_3 distribution within the 99.37% confidence level

p_0 (mbar)	p_c (mbar)	q (ppmv)	$\chi 2$ (≤ 3.02)
250	300	0.525	2.919
275	275	0.550	2.920
225	350	0.550	2.947
225	325	0.525	2.955
250	325	0.575	2.968
250	325	0.550	2.969
275	300	0.575	2.979
250	275	0.500	2.983
275	275	0.525	2.984
250	300	0.550	2.984
225	350	0.575	2.990
275	300	0.550	2.994
200	400	0.575	2.998
225	375	0.600	3.000
200	375	0.550	3.010
225	375	0.575	3.020

By the statistical analysis described above, we obtain a reasonable "range" of PH_3 vertical distribution, which covers the real PH_3 abundance by 99% confidence. Eddy diffusions of the bulk atmosphere and photochemical reactions control the PH_3 mixing ratio in the upper troposphere. Dynamical and chemical modeling PH_3 will help us to determine these factors.

4.4. Photochemical Model

Thermodynamic equilibrium calculation shows that PH_3 does not originate chemically in the stratosphere and upper troposphere of Jupiter due to the relatively low temperatures. The existence of observable quantities of PH_3 in the absence of known stratospheric chemical source therefore requires a rapid upward transport from deeper, warmer atmospheres. The relatively high temperatures of Jupiter and Saturn exclude the condensation of PH_3 in the troposphere of these planets. (In Uranus or Neptune, however, the saturation of PH_3 may condense it out of the gas phase in those colder atmospheres.) On the other hand, solar UV radiation and other photochemical reactions will destroy PH_3 while they are in the lower stratosphere or upper troposphere. As a result, the fact that phosphine existed in the photochemically controlled region above ammonia cloud indicates fast vertical mixing from deeper levels on a timescale shorter than PH_3's chemical lifetime, and the vertical distribution of PH_3 in the upper troposphere is strongly sensitive to the speed of dredging up from deep atmosphere. Thus, the measurement of PH_3 vertical mixing ratio profile provides a tracer for determining vertical motion in the upper troposphere.

To describe the characteristic vertical motion by a macroscopic quantity, we follow the usual one-dimensional photochemical modeling convention of treating atmospheric mixing as eddy diffusion process. The diffusion rate at each pressure level is parameterized by a quantity known as the eddy diffusion coefficient K, in unit of cm^2 sec^{-1}. Eddy diffusion coefficient corresponds to the macroscopic bulk atmospheric vertical motion. In practice, however, eddy diffusion coefficients are difficult to

determine theoretically, so a range of empirical values is normally considered.

In this work, we use the Caltech/JPL one-dimensional photochemical model to solve photochemical reactions and dynamical transport of each specific species in each Jovian pressure level. We divide Jupiter's atmosphere into 115 layers, with the lower boundary at ~1.2 bar (the lowest observational sensitive level) and the upper boundary at 10^{-9} bar. The pressure layers are specially fine-girded from 10 mbar to 1000 mbar (roughly 10 - 20 mbar differences per grid) for the model's focusing. The pressure-temperature profile used in this model is derived from Lindal *et al.* [1981], the same profile as being adopted in the radiative transfer model. Solar UV radiation is computed using the solar maximum UV flux of Mount and Rottman [1981] for 10°N latitude. Attenuation of solar UV radiation is computed by considering chemical absorptions, Rayleigh scatterings, and aerosol scatterings in the stratosphere and upper troposphere. Chemical opacities may be contributed by hydrocarbons and/or ammonia. Major hydrocarbons in the stratosphere, such as H_2, CH_4, C_2H_2, C_2H_4, C_2H_6, C_3H_8, and C_4H_2, are derived from Gladstone *et al.* [1996]. However, major absorption bands for hydrocarbons are below 1600 Å, which only overlap by tails with PH_3 absorption cross-section wavelength up to 2100 Å. NH_3 absorption may be the biggest opacity source for PH_3. Rayleigh scatterings by H_2 and He are considered in this model. The cross-sections for Rayleigh scattering from 1150 Å to 9000 Å by H_2 are taken from Ford and Browne [1973], and the cross-sections by He are calculated based on the index of refraction taken from Dalgarno and Kingston [1960]. We also consider the solar radiation scattered by aerosol in the Jovian troposphere, where the optical depth for haze and cloud is larger than that in the stratosphere. On the basis of cloud model by West *et al.* (1986; and personal communication), we adopt the optically

thin haze layer (1 to 30 mbar), NH_3 ice haze layer (200 to 600 mbar), and NH_3 cloud layer (600 to 800 mbar), in our model. The single-scattering phase function for the aerosols used in this model was taken from Tomasko and Smith [1982].

Prinn and Lewis [1975] suggested a simple photochemical reaction scheme to account for observable PH_3 abundance above Jovian cloud top. Kaye and Strobel [1984] then introduced a new photochemical scheme, which ultimately converts PH_3 to P_2H_4. Our photochemical reactions of phosphorus and nitrogen species are basically derived from Kaye and Strobel, and Atreya *et al.* [1985]. Table 4-2 shows the complete list of the photochemical reactions used in this model. Major PH_3 destructions are by UV radiation (R3), hydrogen atom (R36), and NH_2 radical (R37).

Table 4-2. Photochemical Reactions used in the model

Reaction				Rate Constant[1]	Reference
R1	$NH_3 + h\nu$	$\rightarrow$	$NH_2 + H$	J_1 (80 Å - 2300 Å)	
R2	$N_2H_4 + h\nu$	$\rightarrow$	$N_2H_3 + H$	J_2 (1210 Å - 2050 Å)	
R3	$PH_3 + h\nu$	$\rightarrow$	$PH_2 + H$	J_3 (60 A - 2100 Å)[2]	
R4	$2H + M$	$\rightarrow$	$H_2 + M$	$k_0 = 2.70\times10^{-31}\ T^{-0.6}$	Ham *et al.* [1970]
R5	$H + CH_3$	$\rightarrow$	CH_4	$k = 3.5\times10^{-10}$	
R6	$N + H_2$	$\rightarrow$	$NH + H$	$k = 4.65\times10^{-10}$	Koshi *et al.* [1990]
R7	$NH + H$	$\rightarrow$	$N + H_2$	$k = 1.66\times10^{-12}\ T^{0.7} e^{-956/T}$	Mayer and Schieler [1966]
R8	$NH + H_2$	$\rightarrow$	$NH_2 + H$	$k = 5.96\times10^{-11}\ e^{-7782/T}$	Dove and Nip [1979]
R9	$NH + NH_2$	$\rightarrow$	$N_2H_2 + H$	$k = 2.49\times10^{-9}\ T^{-0.5}$	Davidson *et al.* [1990]
R10	$NH + NH_2$	$\rightarrow$	N_2H_3	$k = 1.16\times10^{-10}$	Pagsberg *et al.* [1979]
R11	$NH_2 + H + M$	$\rightarrow$	$NH_3 + M$	$k_0 = 6.06\times10^{-30}$	Grodon *et al.* [1971]
				$k_\infty = 3.00\times10^{-10}\ e^{-525/T}$	K.S.[3]
R12	$NH_2 + H$	$\rightarrow$	$NH + H_2$	$k = 1.00\times10^{-11}$	Baulch *et al.* [1992]
R13	$NH_2 + H_2$	$\rightarrow$	$NH_3 + H$	$k = 5.97\times10^{-12}\ e^{-4570/T}$	Hack *et al.* [1986]
R14	$2NH_2 + M$	$\rightarrow$	$N_2H_4 + M$	$k_0 = 1.30\times10^{-28}$	Mulenko *et al.* [1987]
				$k_\infty = 2.60\times10^{-9}\ e^{-17/T}$	K.S.
R15	$2NH_2$	$\rightarrow$	$NH_3 + NH$	$k = 8.30\times10^{-11}\ e^{-5032/T}$	Davidson *et al.* [1990]
R16	$NH_2 + CH_3$	$\rightarrow$	CH_3NH_2	$k = 8.70\times10^{-11}\ e^{-35/T}$	K.S.
R17	$NH_3 + M$	$\rightarrow$	$NH_2 + H + M$	$k = 3.65\times10^{-8}\ e^{-47036/T}$	Davidson *et al.* [1990]
R18	$NH_3 + H$	$\rightarrow$	$NH_2 + H_2$	$k = 9.00\times10^{-19}\ T^{2.4}\ e^{-4990/T}$	Ko *et al.* [1990]
R19	$NH_3 + CH$	$\rightarrow$	PROD	$k = 7.23\times10^{-11}\ e^{+317/T}$	Becker *et al.* [1993]
R20	$NH_3 + CH_3$	$\rightarrow$	$NH_2 + CH_4$	$k = 7.77\times10^{-13}\ e^{-6365/T}$	Leroy *et al.* [1985]
R21	$N_2 + H$	$\rightarrow$	$NH + N$	$k = 4.98\times10^{-12}\ T^{0.5}\ e^{-71450/T}$	Roose *et al.* [1978]
R22	$N_2H_3 + H$	$\rightarrow$	$2NH_2$	$k = 2.70\times10^{-12}$	Gehring *et al.* [1971]
R23	$2N_2H_3$	$\rightarrow$	$N_2 + N_2H_4 + H_2$	$k = 6.00\times10^{-11}$	
R24	$N_2H_4 + H$	$\rightarrow$	$N_2H_3 + H_2$	$k = 9.87\times10^{-12}\ e^{-1198/T}$	Stief and Payne [1976]
R25	$P + H + M$	$\rightarrow$	$PH + M$	$k_0 = 3.40\times10^{-33}\ e^{+173/T}$	K.S.
R26	$P + H_2 + M$	$\rightarrow$	$PH + H + M$	$k_0 = 5.00\times10^{-15}$	Husain and Norris [1982]
				$k_\infty = 2.00\times10^{-32}$	
R27	$P + PH$	$\rightarrow$	$P_2 + H$	$k = 5.00\times10^{-11}\ e^{-400/T}$	K.S.
R28	$2P + M$	$\rightarrow$	$P_2 + M$	$k_0 = 1.40\times10^{-33}\ e^{+500/T}$	K.S.

R29	$PH + H$	$\rightarrow$	$P + H_2$	$k = 1.50\times10^{-10}\, e^{-416/T}$	K.S.
R30	$PH + H_2 + M$	$\rightarrow$	$PH_3 + M$	$k_0 = 3.00\times10^{-36}$	K.S.
R31	$PH_2 + H$	$\rightarrow$	$PH + H_2$	$k = 6.20\times10^{-11}\, e^{-318/T}$	K.S.
R32	$PH_2 + H$	$\rightarrow$	PH_3	$k = 3.70\times10^{-11}\, e^{-340/T}$	K.S.
R33	$PH_2 + CH_3$	$\rightarrow$	CH_3PH_2	$k = 1.20\times10^{-10}\, e^{-37/T}$	K.S.
R34	$PH_2 + NH_2$	$\rightarrow$	NH_2PH_2	$k = 1.00\times10^{-10}\, e^{-18/T}$	K.S.
R35	$2PH_2$	$\rightarrow$	P_2H_4	$k = 2.80\times10^{-11}\, e^{-30/T}$	K.S.
R36	$PH_3 + H$	$\rightarrow$	$PH_2 + H_2$	$k = 7.21\times10^{-11}\, e^{-887/T}$	Arthur *et al.* [1997]
R37	$PH_3 + NH_2$	$\rightarrow$	$PH_2 + NH_3$	$k = 1.36\times10^{-12}\, e^{-984/T}$	Cosbo *et al.* [1986]
R38	$P_2 + H$	$\rightarrow$	$PH + P$	$k = 6.20\times10^{-11}\, e^{-318/T}$	

[1] The photodissociation rate constants for R0 to R5 are in units of s^{-1}. Two-body rate constants are in units of cm^3 $molecule^{-1}$ s^{-1}. Three-body rate constants are in units of cm^6 $molecule^{-2}$ s^{-1}.

[2] Value for R3 is for diurnally averaged radiation fields at 500 mbar, 10° N latitude, and PH_3 cross-sections for $\lambda \geq 1500$ Å are taken from Chen *et al.* [1991].

[3] K.S. represents Kaye and Strobel. [1984].

The importance of NH_3 - PH_3 coupling was introduced by Strobel [1977] via the reaction R37,

$$NH_2 + PH_3 \rightarrow NH_3 + PH_2.$$

The photochemistry of NH_3 and PH_3 are always considered together because both are abundant in the upper troposphere of Jupiter, absorb UV radiation in an overlapping wavelength regime (1600 Å - 2100 Å), and undergo similar photolysis schemes. If R37 were fast enough in the Jovian troposphere, it might affect the result by competing the phosphine destruction with hydrogen atom. We adopt the rate constant for R37 from measurement by Cosbo *et al.* [1983]. The rate constant for R36, $PH_3 + H \rightarrow PH_2 + H_2$, is taken from the recently measurement by Arthur *et al.* [1997].

NH_3 is one of the most important photochemical species under the tropopause of Jupiter. We expect two competitive factors cited by NH_3 for the vertical distribution of PH_3: (1) NH_3 in the upper troposphere attenuates the photolysis rate of PH_3 by shielding solar UV radiation in the range of PH_3 photodissociation wavelength (1600 Å - 2100 Å); (2) NH_2 radical, originated from photodissociation of NH_3, tends to eliminate PH_3 in the upper troposphere by R37.

The temperature in the troposphere of Jupiter is high enough for preventing condensation of PH_3, but not enough for NH_3. The ice-gas phase transition of NH_3 ranges from 100 K to 195 K, which falls on the typical temperature range of the Jovian upper troposphere. In fact, the observation of NH_3 mixing ratio above cloud top provides an evidence of saturated NH_3 distribution from 300 mbar to 800 mbar [Griffith *et al.* 1992].

We consider the precipitation of NH_3 using the saturated vapor pressure below tropopause ($p > 100$ mbar). Griffith *et al.* also detected and discussed the strong depletion of NH_3 in the tropopause by different pathways. We do not include those special factors introduced by them to explain the NH_3 depletion mechanism, like charged particle bombardment, lightning, or over condensation process. The saturated NH_3 mixing ratio profile is adopted in the model from 300 mbar to 800 mbar, in compatible with the infrared observation described above. The evidence for condensation of NH_3 in the upper troposphere may also provide an indirect lower limit for our conclusion: The too low eddy diffusion coefficient for yielding NH_3 abundance lower than its saturation profile from 300 mbar to 800 mbar will be prohibited.

4.5. Model Results

In our model, PH_3 profile is conveniently divided into two layers. The transition pressure level p_t is defined as the boundary level between higher altitude layer (eddy diffusion coefficient = K_h) and lower altitude layer (eddy diffusion coefficient = K_l). We simply estimate the p_t values from all these profiles shown in Figure 4-4, ranging from 275 mbar to 400 mbar. For the PH_3 mixing ratio in deep troposphere, both infrared observations, which sample the 0.5 – 4 bar pressure range in Jupiter (Table 4-3), and our observation from 0.2 to 0.6 bar, obtains the PH_3 mixing ratio of $(0.5 - 0.6) \times 10^{-6}$, arguing that PH_3 must be well-mixed in the lower troposphere. The retrieved profiles within 99.73% confidence level, as shown in Figure 4-4, agree well for the mixing ratio of PH_3 below 600 mbar level to be $(0.55 \pm 0.05) \times 10^{-6}$. We thus constrain the parameter q (mixing ratio at lower boundary level in our model) from 5.0×10^{-7} to 6.0×10^{-7}.

We first test the uniform eddy diffusion coefficient cases, i.e. $K_l = K_h$. The eddy diffusion coefficients ranging from 10^3 $cm^2 sec^{-1}$ to 10^7 $cm^2 sec^{-1}$, in accordance with q = 0.55 ppmv mixing ratio at the lowest boundary, will be applied to the model. These results of test models (K= 10^3, 10^4, 10^5, 10^6, and 10^7 $cm^2 sec^{-1}$) are shown in Figure 4-6. The adopted eddy diffusion coefficients cover a reasonable range of dynamical motion in the troposphere and lower stratosphere, suggested by Prinn and Lewis [1976], Kaye and Strobel [1984], Griffith *et al.* [1993], and Edgington *et al.* [1998]. For larger K values, the transport time scale is much smaller than the photochemical destruction time scale for

Table 4-3. Published Jupiter PH_3 Abundance

Mixing Ratio (ppmv)	Pressures (bar)	λ (μm)	Author
0.54	5	4.8	Larson *et al.* 1977
0.7 ± 0.1	2 – 5	4.8	Bjoraker *et al.* 1986
0.6 ± 0.2	1 – 4	4.6	Kunde *et al.* 1982
0.41 ± 0.15	1 – 2	4.5	Drossart *et al.* 1982
0.54	1	9.0	Ridgway *et al.* 1976
0.54 ± 0.10	0.65	4.6	Kunde *et al.* 1982
0.30 ± 0.23	0.6	8.9	Griffith *et al.* 1992
0.75 ± 0.18	0.1 – 1.0	9.0	Knacke *et al.* 1982
0.37 ± 0.05	0.50	4.6	Kunde *et al.* 1982
0.1 - 0.2	0.2 – 0.6	8.3 – 11.6	Encrenaz *et al.* 1978, 1980
0.09 - 0.18	≤ 0.6	10.2 – 13.4	Tokunaga *et al.* 1979
< 0.15	0.14	0.16 – 0.23	Edgington *et al.* 1998
0.55 ± 0.2	0.2 – 0.6	380	this work

PH_3 in the upper troposphere, which pushes PH_3 to higher altitude. For example, while K_h > 10^5 cm^2 sec^{-1}, as shown in Figure 4-6, PH_3 might be seen in the stratosphere. Due to the lack of observable PH_3 above tropopause, the eddy diffusion coefficient for higher altitudes (K_h) must be less than 10^5 cm^2 sec^{-1}. A steep profile above 400 mbar level, as shown in Figure 4-4, requires even smaller eddy diffusion coefficient near tropopause.

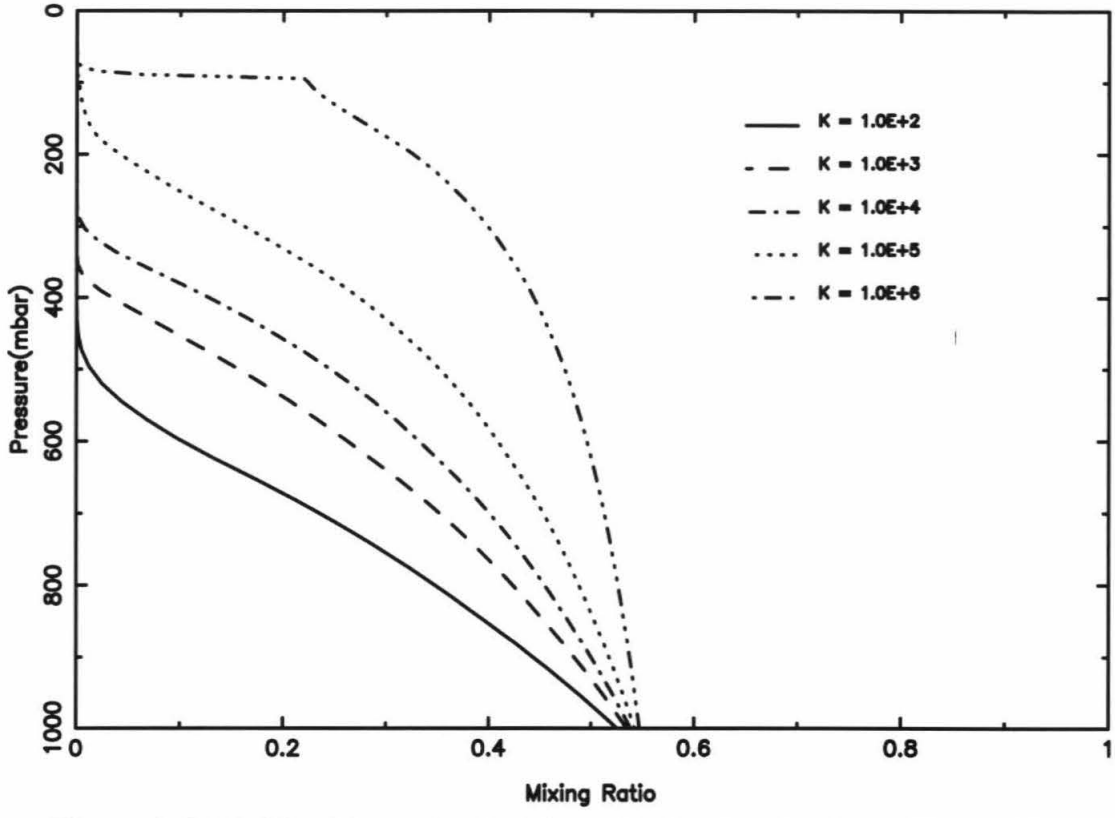

Figure 4-6. Model mixing ratios for PH_3 on Jupiter by adopting uniform eddy diffusion coefficients in the upper troposphere: K = 10^2 cm^2 sec^{-1} (solid), 10^3 cm^2 sec^{-1} (dashed), 10^4 cm^2 sec^{-1} (dash-dot), 10^5 cm^2 sec^{-1} (dotted), 10^6 cm^2 sec^{-1} (dash-dot-dot-dot).

On the other hand, for $K_l < 10^5$ cm^2 sec^{-1}, PH_3 has been strongly depleted in the upper troposphere. The calculated mixing ratios are less than 3.0×10^{-7} for the altitudes above 500 mbar pressure level, which is not consistent with our analysis. This implies that the eddy diffusion coefficient for the lower altitudes (K_l) should be greater than 10^5 cm^2 sec^{-1}. Therefore, $K_l \geq 10^5$ $cm^2 sec^{-1}$, and $K_h < 10^5 cm^2 sec^{-1}$, are reasonable range for estimating eddy diffusion coefficients in the upper troposphere of Jupiter.

However, all these uniform eddy diffusion coefficients shown in Figure 4-6 failed to interpret the characteristics of the best-fit retrievals (Figure 4-4). It seems impractical to find a uniform eddy diffusion coefficient solution for explaining our submillimeter observations.

Figure 4-7 shows five cases proposed to test the sensitivity of eddy diffusion coefficients at higher altitudes. We choose q = 0.55 ppmv at 1.2 bar as boundary condition for all cases. The transition points between two layers are chosen to be 350 mbar, which is estimated by the profiles shown in Figure 4-4. Eddy diffusion coefficients are all set to 1.0×10^7 cm^2 sec^{-1} at lower altitudes. As a result, $K_h = 10^4$ cm^2 sec^{-1} fits well to the best-fit profiles (Figure 4-4) at higher altitudes. K_h value as small as 10^2 cm^2 sec^{-1} (solid line) fails to fit the "slope" of these profiles due to the slow dynamical transport for PH_3. We may also exclude the case for $K_h \geq 10^5$ cm^2 sec^{-1} (dotted line) because there is no observed PH_3 above tropopause. To summarize the uniform eddy diffusion coefficient cases, $10^3 < K_h < 10^5$ cm^2 sec^{-1} is consistent with our observation above the transition level. However, K_l is not constrained as well as K_h by a similar analysis because it lacks upper limit for dynamical motion speed at lower altitudes.

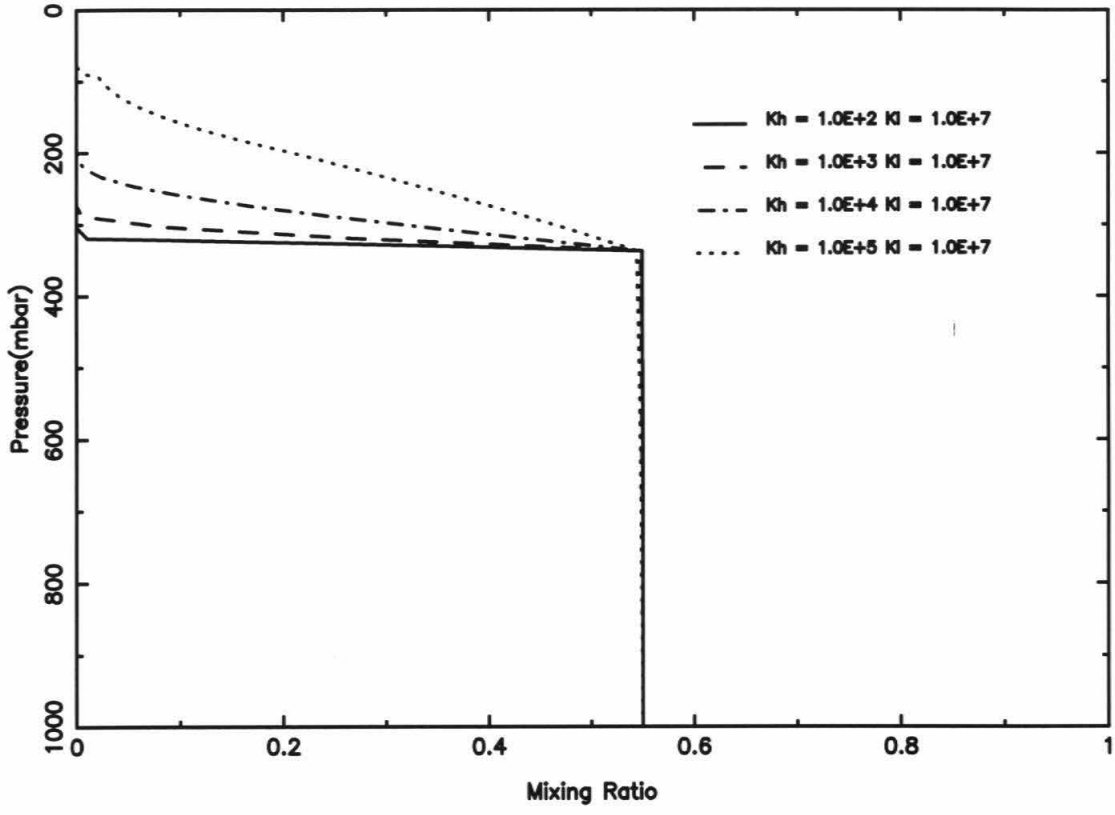

Figure 4-7. PH_3 mixing ratios sensitivity test in the photochemical model. All profiles adopt eddy diffusion coefficients at lower altitudes ($p \geq 350$ mbar) 10^7 cm^2 sec^{-1}. Eddy diffusion coefficients at higher altitudes are: $K_h = 10^2$ cm^2 sec^{-1} (solid), 10^3 cm^2 sec^{-1} (dashed), 10^4 cm^2 sec^{-1} (dash-dot), and 10^5 cm^2 sec^{-1} (dotted).

Other independent measurements and photochemical modeling agree well with our results at higher altitudes ($10^3 < K_h < 10^5$ cm^2 sec^{-1}) in the upper troposphere of Jupiter. The eddy diffusion coefficient estimated from early observations of Jupiter's UV albedo [Tomasko 1974] is less than 2×10^4 cm^2 sec^{-1}, and 1.2×10^4 cm^2 sec^{-1} extrapolated from the measured homopause value by Atreya [1986, p.77] assuming $K \propto n^{-0.5}$ (where n is

number density). $K \leq 3 \times 10^3$ cm^2 sec^{-1} derived from the observed *para*-hydrogen fraction at the equator [Conrath and Gierasch, 1984] also falls in the range of our results.

Assume that the eddy diffusion coefficients are both constants in the two layers, we derived a best-fit case for $K_h = 10^4$ cm^2 sec^{-1}, $K_l \geq 10^6$ cm^2 sec^{-1}, and $p_t = 350$ mbar, in comparison with profiles in Figure 4-4. However, since Atreya suggested $K \propto n^{-0.5}$ [1986] for eddy diffusion coefficient under tropopause, we thus explore our model further by applying the formula,

$$K = K_0 (n / n_0)^{-\alpha}, \tag{4.3}$$

where n is the total number density of the atmosphere, n_0 is the number density at the transition pressure level, and K_0 is the eddy diffusion coefficient proposed at this level.

We adopt the exponent value α to be 0.5, which is as same as the value suggested by Atreya [1986]. At the transition level $p_t \approx 400$ mbar, the number density n_0 is about 2.2×10^{19} cm^{-3}, and we estimate $K_0 \approx 2.0 \times 10^4$ cm^2 sec^{-1}. For levels below the transition point, K is set to 10^6 cm^2 sec^{-1}. The mixing ratio at the lowest boundary for PH_3 is assumed 0.6 ppmv, which is consistent with the observational constraints listed in Table 4-3. The modeling PH_3 vertical profile is shown in Figure 4-8. This result agrees well to our 99.73% confidence level analysis.

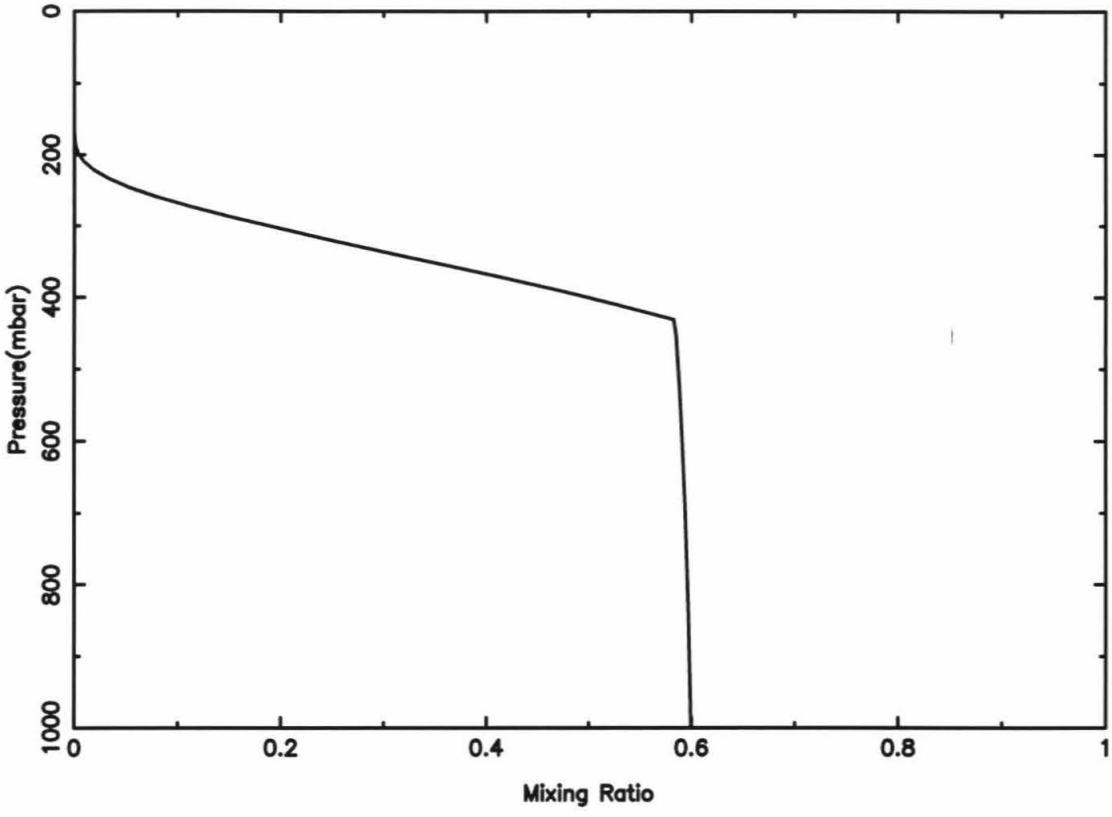

Figure 4-8. Model mixing ratios for PH_3 on Jupiter by adopting functional form eddy diffusion coefficients in the upper troposphere. In this case, at pressure levels 100 mbar $\leq p \leq$ 400 mbar, $K = 2.0 \times 10^4 (n/n_0)^{-0.5}$ cm^2 sec^{-1}. The number density $n_0 = 2.2 \times 10^{19}$ cm^{-3}. PH_3 mixing ratio below 1 bar level is 0.6 ppmv.

However, these parameters may not be determined uniquely by the observation. If we assumed the transition pressure level 550 mbar, and the PH_3 mixing ratio 0.675×10^{-6} at 1.2 bar, we can derive a model result (Figure 4-9) by applying $K_0 = 5.0 \times 10^4$ cm^2 sec^{-1}, $n_0 = 2.5 \times 10^{19}$ cm^{-3}. This transition level is chosen at the cloud top of Jupiter. The χ^2 value for this test case is 3.18, which is not too far away from the acceptable statistical

confidence level.

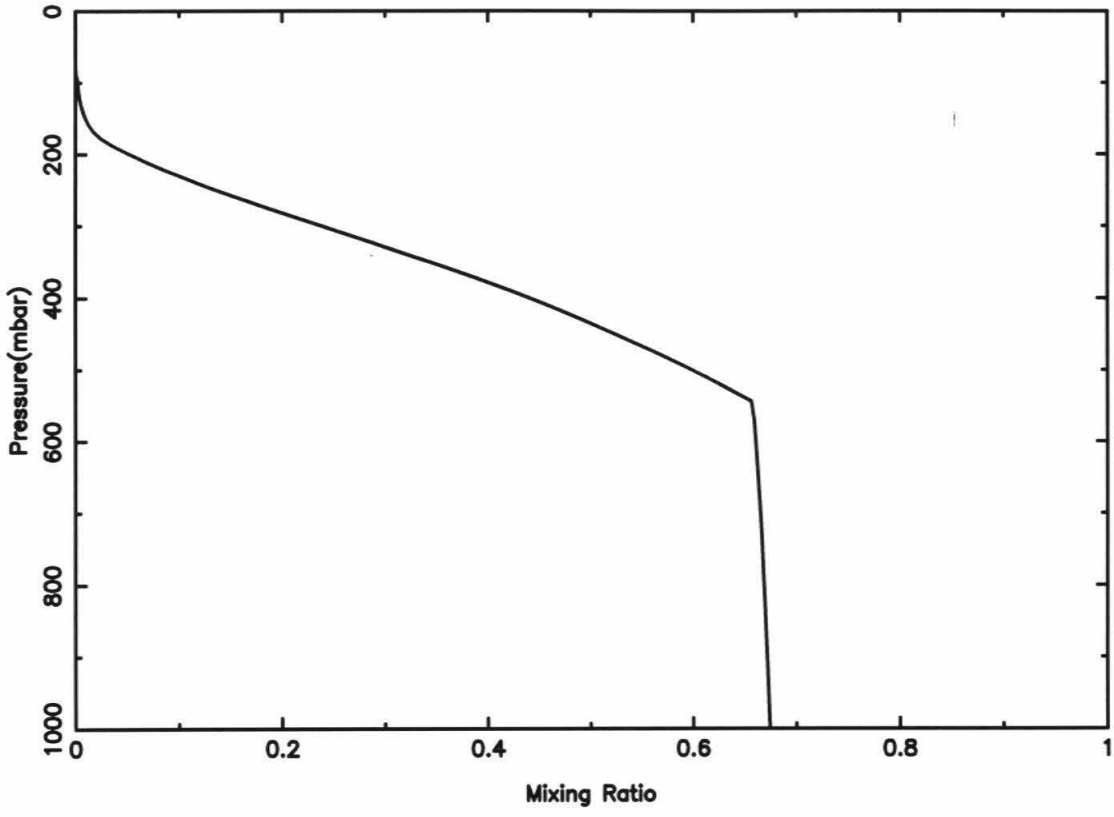

Figure 4-9. Model result for PH_3 mixing ratio on Jupiter by adopting functional form eddy diffusion coefficients in the upper troposphere. In this case, at pressure levels 100 mbar $\leq p \leq$ 550 mbar, $K = 5.0 \times 10^4 (n/n_0)^{-0.5}$ cm^2 sec^{-1}. The number density $n_0 = 2.5 \times 10^{19}$ cm^{-3}. PH_3 mixing ratio below 1 bar level is 0.675 ppm.

4.6. Discussion and Summary

Detection of the PH_3 J=3-2 transition in Jupiter has allowed inversion for the PH_3 vertical mixing profile as a function of pressure in Jupiter's upper troposphere. While confirming the roughly solar [6.2×10^{-7}; Anders and Grevesse, 1989] deep tropospheric mixing ratio determined from infrared observations, the well-resolved and uncontaminated lineshape reveals a much more rapid falloff with altitude of the PH_3 abundance than infrared measurements and photochemical models had previously suggested. The steep slope of the falloff profile implies an eddy diffusion coefficient at higher altitudes near tropopause, 10^3 cm^2 sec^{-1} < K_h < 10^5 cm^2 sec^{-1}, for transition level p_t = 250 - 400 mbar, while our deep PH_3 concentrations of $0.55 \pm 0.05 \times 10^{-6}$ requires a deep tropospheric eddy diffusion coefficient of $K \geq 10^5$ cm^{2}sec^{-1}. The best-fit functional form for eddy diffusion coefficient above 400 mbar is $K = 2.0 \times 10^4 (n / 2.2 \times 10^{19})^{-0.5}$ cm^2 sec^{-1}.

Table 4-3 summarizes the previous PH_3 determinations on Jupiter, arranged in order of decreasing pressure of peak sensitivity. As it indicates, most previous determinations are derived from infrared spectroscopy. While our best "deep" PH_3 mixing ratio $5.5 \pm 2.0 \times 10^{-7}$ agrees well with those obtained by Ridgway [1976], Drossart *et al.* [1982], Kunde *et al.* [1982], and roughly with that of Knacke *et al.* [1982] at deep levels, our best-fit PH_3 profile requires more PH_3 in the upper troposphere than found by these authors at the same levels. We also find significantly more PH_3 in the upper troposphere than derived from the measurements of Encrenaz *et al.* [1978, 1980], Tokunaga *et al.* [1979], and Griffith *et al.* [1992]. We have no reason to believe that temporal variations are

responsible for this discrepancy, especially since changes on a global scale would be required to produce an appreciable effect over our large beam. However, observations at 5 μm may indicate that the PH_3 abundance in Jupiter is spatially variable by a factor of up to two [Drossart *et al.* 1984, Bjoraker 1985, and Drossart *et al.* 1990].

The chemical production source for PH_3 is essentially absent in the region that we modeled. Photochemically destruction mechanism for PH_3 is therefore important for determining what altitude that the dynamical motion of PH_3 could reach. Several reactions are responsible for PH_3 decomposition: PH_3 photolysis (R3) by solar UV radiation, chemically loss by reacting with H atoms (R36), or NH_2 radicals (R37). For CH_4 and hydrocarbons in the stratosphere, UV photolysis is the major sink for CH_4 [Gladstone *et al.* 1996]. However, most UV photons are shielded, or scattered in the deeper atmosphere that we studied. The most important opacity source for PH_3 photodissociation is the absorption of UV by NH_3 above 300 mbar pressure level. Rayleigh scattering by H_2, He and aerosol scattering by haze layer above NH_3 clouds contribute partly to the attenuation of solar UV radiation. As shown in Figure 4-10, PH_3 photodissociation rate (R3) has only been seen near the tropopause, with several orders of magnitude slower than chemical destruction by H and NH_2 (R36 and R37, respectively), which are major sinks for PH_3 in the upper troposphere.

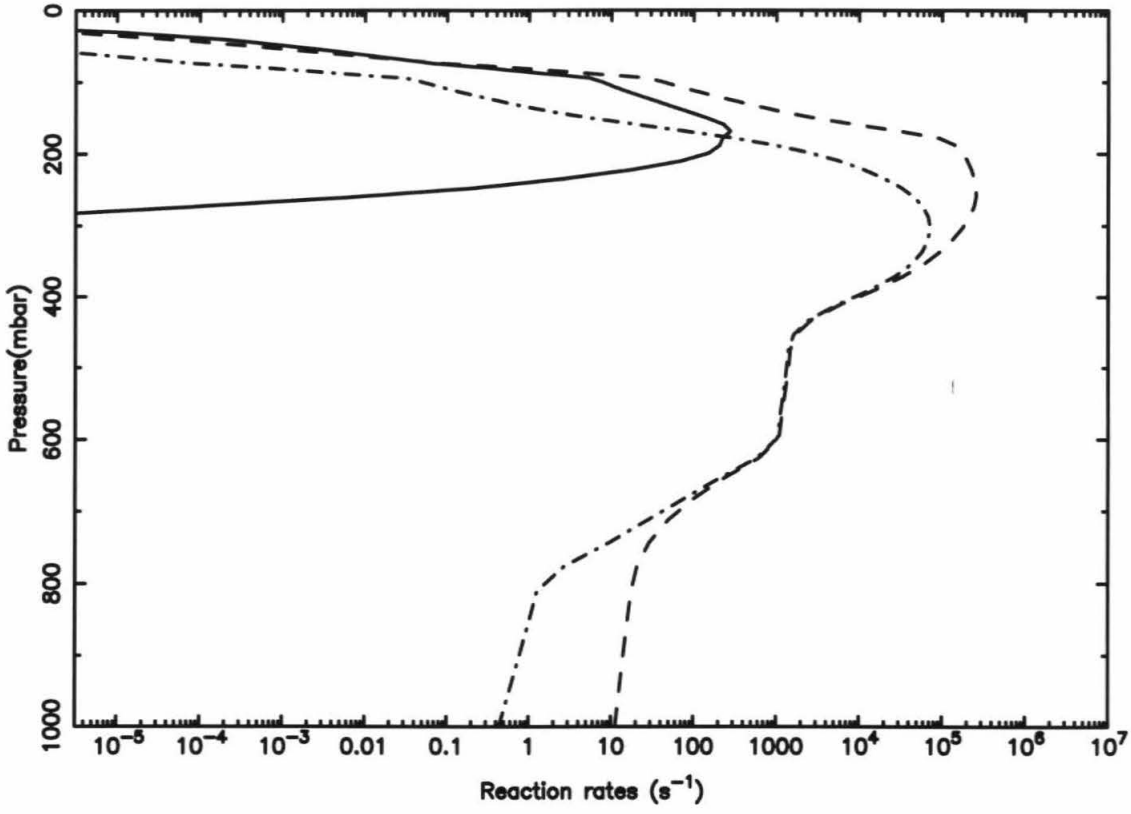

Figure 4-10. Photochemical reaction rates for PH_3 loss mechanism: $PH_3 + h\nu = PH_2 + H$ (solid), $PH_3 + H = PH_2 + H_2$ (dashed), $PH_3 + NH_2 = PH_2 + NH_3$ (dash-dot).

The presence of NH_3 in the upper troposphere is important to PH_3 destruction mechanism. The shielding of UV radiation by NH_3 reduces the photolysis rate for PH_3. On the other hand, while NH_3 decomposes to H and NH_2 radicals by solar radiation near tropopause, H and NH_2 will react with PH_3 to increase its loss rate. For example, at 200 mbar pressure level, our model shows that the NH_3 photolysis (R9) rate is 2.41×10^5 cm^{-3} sec^{-1}, the H and NH_2 production rates at the same level are 2.44×10^5 cm^{-3} sec^{-1}, $2.45 \times$

10^5 cm^{-3} sec^{-1}, respectively. There are 98% H and NH_2 radicals generated by NH_3 photodissociation. The PH_3 loss rate at 200 mbar is 2.06×10^5 cm^{-3} sec^{-1}, while the PH_3 photodissociation (R11) rate is only 69.4 cm^{-3} sec^{-1}, only 0.033% to the total loss rate. Therefore, we can conclude that the chemical destructions by H and NH_2, which come from NH_3 photolysis, are the major mechanism responsible for PH_3 loss in the upper troposphere of Jupiter.

Combining the results from the upper and deep troposphere of Jupiter gives the first simultaneous determination of the eddy diffusion coefficient in these two pressure regimes, and is consistent with a significant contrast between the deep and upper tropospheric eddy diffusion coefficients previously proposed by Massie and Hunten [1982]. We tentatively identify the 300 - 400 mbar levels, the pressure level at which our data indicates a change in K of several orders of magnitude, as the radiative-convective boundary of Jupiter. This boundary is expected to occur where the atmospheric temperature lapse rate first decreases from the convectively unstable adiabatic rate to a sub-adiabatic value. The atmospheric level at which this transition occurs delineates the boundary between the well-mixed troposphere and the overlying stably stratified stratosphere. The radiative-convective boundary thus marks the true dynamical boundary between troposphere and stratosphere, and evidently occurs slightly deeper than the temperature inversion (which occurs at p ~ 140 mbar and T ~ 110K in Jupiter). The pressure of the radiative-convective boundary obtained from our PH_3 inversion is slightly smaller than that predicted by radiative-convective models of Appleby and Hogan [1984], which suggest the boundary occurs in the range 500 - 700 mbar, except that we adopt the functional form proposed for transition level at 550 mbar. However, the

radiative-convective boundary can also be estimated as the pressure level corresponding to the observed effective infrared temperature of Jupiter. Combining the 124.4 ± 0.3K observed by Voyager [Hanel *et al.* 1981] with the p-T profile of Lindal *et al.* [1981] gives a pressure of ~ 360 mbar, in excellent agreement with the pressure level for the radiative-convective boundary implied by our measurements.

A small eddy diffusion coefficient in the upper troposphere also has important chemical implications for the upper atmosphere of Jupiter, since a stagnant (low K) region in the upper troposphere can also produce enhanced abundance in chemically inactive species, which flow downward through the troposphere with a constant flux. Landry *et al.* [1991] have shown that this process is capable of producing concentrations which are comparable to those generated by rapid upward mixing from the deep troposphere. The small upper tropospheric eddy diffusion coefficient derived from our PH_3 analysis therefore suggests that stratospheric photochemical production may provide a substantial fraction of the observed abundance of disequilibrium species at $p < 400$ mbar in Jupiter. This mechanism could enrich the upper tropospheric concentrations of species such as CO, HCN, and hydrocarbons such as C_2H_2.

Chapter 5

Two-Dimensional Model of C_2H_6 in the Lower Stratosphere of Jupiter

5.1. Introduction

Studies of two-dimensional (hereafter 2-D) dynamical transport and circulation models for the upper troposphere and lower stratosphere of Jupiter started more than a decade ago. Unlike the Earth, however, there were fewer observational constraints on Jupiter, thus these proposed circulation models need validation. The infrared measurements of C_2H_2 and C_2H_6 at wavelengths around 814 cm^{-1} at different latitudes of Jupiter by Orton *et al.* [1989] provide an opportunity to test the current 2-D models. On the basis of 2-D circulation computed by West *et al.* [1992] and Friedson *et al.* [1999], we perform dynamical models for C_2H_6 in the Jovian lower stratosphere and upper troposphere, and compare the results with Orton *et al.*'s observations, to test the validity of their dynamical models.

As in many areas of the planetary science, progress in the dynamical transport model for the Jovian atmosphere was driven by satellite and ground-based observations. Using the data from Voyager infrared spectrometer (IRIS), Gierasch *et al.* [1986] deduced the meridional residual circulation at the 150- and 270-mbar pressure levels of the Jovian

atmosphere. In this simple 2-D transport scheme of the upper troposphere, they suggested a meridional circulation associated with the zonal jet system of Jupiter. The cloud, NH_3, and para-hydrogen distribution observed by IRIS are consistent with upwelling motion at the equatorward edges of prograde atmospheric jets, and subsidence in the poleward edges of the jets. The temperature field derived by Voyager IRIS is also consistent with such vertical motion, with radiative heating balancing adiabatic cooling of rising air parcels. They also found that the zonal wind jets decay with altitude within the upper troposphere. This implies a dynamical model with Coriolis acceleration of the zonal wind balanced by a linear mechanical drag. These findings suggested that the residual circulation in the upper troposphere might closely approximate the Lagrangian mean circulation.

Conrath *et al.* [1990] introduced a zonally symmetric, linear radiative-dynamical model of the upper troposphere and lower stratosphere of Jupiter, Saturn and Uranus. They extended the calculation of the residual circulation up to the 0.1 mbar pressure level, using a dynamical model similar to that of Gierasch *et al.* [1986] but including seasonally varying insolation with frictional damping to drive the circulation. Their model considered radiative heating and cooling by CH_4 and C_2H_6, but ignored the effect of aerosols. They derived a residual circulation of the same form as that of Gierasch *et al.* [1986] below the 10 mbar level, with regions of upwelling and subsidence alternating with latitude on a scale of the width of the zonal jets. In the upper atmospheric levels above 10 mbar, where Gierasch *et al.* [1986] did not study, they predicted a global circulation with rising motion over the equatorial region and sinking over the poles.

The seasonal effect and latitudinal gradient of radiative heating is weak according to

Conrath *et al.* [1990]. Their model ignored the effect of solar heating due to aerosol absorption. However, stratospheric aerosols on Jupiter are abundant in the polar region and may produce strong latitudinal thermal gradients by solar heating. West *et al.* [1992] included the radiative heating by polar aerosols in their circulation model. They adopted the atmospheric aerosol distribution from the International Ultraviolet Explorer (IUE) observations. The inferred 2-D residual circulation is different from that of Conrath *et al.* [1990]. The circulation between 0.1 mbar level and 270 mbar level consists of two different patterns. Below 100 mbar pressure level near tropopause of Jupiter, the circulation derived by West et al. [1992] is similar to that obtained by Gierasch *et al.* [1986] for the upper troposphere, but with the important difference that strong subsidence is predicted for the regions poleward of ±50°. Net radiative cooling of the upper troposphere in the polar region induces the subsidence. In the lower stratosphere above 100 mbar level, in each hemisphere, there is a circulating cell centered near the 10 mbar level, with air sinking at low and mid-latitudes and rising at high latitudes. Air lying above ~10 mbar drifts equatorward in this model while air below this level drifts poleward.

Moreno and Sedano [1997] performed a similar calculation of the residual circulation on Jupiter, based on West *et al.*'s method [1992], but used a different spatial distribution for the stratospheric aerosol derived from Hubble Space Telescope (HST) images. They obtained a different circulation above the 50-mbar level, based on the different pattern of solar heating. The circulation cells are induced by upwelling at low and mid-latitudes and subsidence at high latitudes except for a small region of upwelling at high latitudes in the southern polar region. Below 50-mbar level, their residual

circulation is qualitatively similar to that of West *et al.* [1992].

The 2-D dynamical transport of tracer in the terrestrial stratosphere could be closely approximated by the advective residual circulation because transport effects induced by eddy transience and dissipation could be ignored to first order in comparison with zonal mean diabatic effects [Dunkerton, 1978]. This approximation requires that eddies are linear, steady, and adiabatic [Andrews *et al.* 1987]. However, Orton *et al.* [1994] detected changes in the shape of planetary wave packet in the upper troposphere and stratosphere of Jupiter occurring on a time scale ~10^6 s, which is comparable to the residual advection time scale. Therefore, Friedson *et al.* [1999] suggested that the 2-D transport model of the Jovian stratosphere should include eddy dispersive transport due to wave transience or other non-linear effects. They use the HST observations of the spreading of debris introduced into Jupiter's stratosphere by the impact of Comet Shoemaker-Levy 9 to test the formulation of mixing and transport in 2-D models. The impact debris was transported rapidly equatorward by stratospheric winds from the impact latitude -45° to at least -20° during the 3.2-year period. The authors indicated that all above 2-D residual circulation models, which only considered advection and small-scale eddies, predict poleward drifting of air in the southern hemisphere between the 100 and 10 mbar levels. The disagreement between these advection-only models and the observations suggests the possible importance of eddies. Friedson *et al.* [1999] further proposed an alternative phenomenological model for the transport based on large-scale mixing due to quasi-geostrophic eddies. They introduced the zonal mean horizontal eddy diffusion coefficients (K_{yy}) into the dynamical advection model by West *et al.* [1992]. The modified residual circulation model explains qualitatively the equatorward spreading of

the S-L9 debris.

The K_{yy} parameterizes the eddy meridional dispersive transport, which was not considered in the previous 2-D models. However, Friedson *et al.* [1999] treated the eddy mixing only occurring along isobaric surfaces, and thus ignored the vertical dispersion terms. In this paper, we further test the influence of large-scale vertical eddy mixing (K_{zz}; see the formula of 2-D transport in the next section.) on the 2-D transport model in the lower stratosphere and upper troposphere of Jupiter. Although there is no direct observational evidence for significant vertical dispersion in the Jovian upper troposphere, eddy mixing may be important for the vertical motion above the cloud top according to the recent study of PH_3 by Lee *et al.* [2000]. The origin of such large-scale vertical eddy mixings in the upper troposphere is still uncertain, breaking of propagating gravity waves from the lower atmosphere may provide part of the explanation.

Introducing a different residual circulation requires new measurements of latitudinal temperature distribution. Instead, we provide a complete test for the current 2-D transport models in Jovian lower stratosphere and upper troposphere (270 to 0.1 mbar pressure levels). Different combinations of residual advection, horizontal eddy dispersion, and vertical eddy mixing will be examined by modeling C_2H_6 mixing ratios at different latitudes, and comparing with Orton et al.'s [1989] infrared observations. Constraining 2-D model results by C_2H_6 observations takes advantages of the sensitivity of the radiative transfer modeling for vertical distribution of the tracer. The 2-D model formulation and all the dynamical processes (advection, horizontal eddy mixing, vertical eddy mixing, and boundary flux) will be described in section 2.

Since the 2-D test models are to be explored over a wide range of the parameter space for all these processes by the power of modern computers, we need a simple radiative model to evaluate every model result before processing the detailed and complicated radiative transfer computations. A simple and efficient two-layer radiative transfer integration method will be introduced in section 3. This method provides a first-order estimate of the C_2H_6 vertical distribution from a model at certain latitude to fit Orton *et al.*'s [1989] observations.

5.2. Two-Dimensional Dynamical Model

Simulation of the spatial distribution and photochemical interaction of trace species in the atmosphere often requires accurate numerical treatment for advection and diffusion. The consideration for dynamical motion in the two-dimensional model, which includes both meridional and vertical directions, is obviously more complex than the simple eddy diffusion parameterized vertical motion in the one-dimensional photochemical model. We will describe the derivation of 2-D computational formula and the origins of the possible processes (stream function, eddy diffusion coefficient, and boundary flux) adopted in the model in the following paragraphs.

In the absence of sources, sinks, and viscosity, the rate of change of a trace constituent in a fixed volume in a fluid field is equal to the amount of constituent transported across the boundaries into or out of the volume,

$$\frac{\partial \rho}{\partial t} + \bar{\nabla} \cdot \rho \vec{u} = 0, \tag{5.1}$$

where ρ is the tracer density and $\vec{u}$ is the fluid velocity. $\rho\vec{u}$ is conventionally defined as the constituent flux.

The equation (5.1) can be rewritten in the advective form

$$\frac{d\rho}{dt} = \frac{\partial \rho}{\partial t} + \vec{u} \cdot \bar{\nabla}\rho = -\rho \bar{\nabla} \cdot \vec{u}, \tag{5.2}$$

where $\vec{u} \cdot \bar{\nabla}\rho$ is the advection of the tracer.

For incompressible flows the velocity is nondivergent ($\bar{\nabla} \cdot \vec{u} = 0$). Therefore, the right-hand side of equation (5.2) is zero, and the tracer is conserved following a fluid parcel.

We replace the density variable ρ by mixing ratio χ, which is frequently used in tracer transport modeling:

$$\frac{\partial \chi}{\partial t} + \vec{u} \cdot \vec{\nabla} \chi = 0 .$$

For a practical 2-D model, dispersions, sources and sinks of the tracer constituent should be considered. The continuity equation (5.2) is thus written as

$$\frac{\partial \chi}{\partial t} + \vec{u} \cdot \vec{\nabla} \chi = (P - L) + \vec{\nabla} \cdot K \vec{\nabla} \chi \tag{5.3}$$

where P and L represents photochemical production and loss, and K is an "eddy diffusion" coefficient, which is meant to represent small-scale irreversible dispersions.

The mass-conserved fluid velocity field for advection can be defined as the derivatives of a "stream function" ψ,

$$\upsilon = -\frac{\partial \psi}{\partial z} . \tag{5.4}$$

$$\omega = \frac{\partial \psi}{\partial y} . \tag{5.5}$$

For the 2-D velocity field $\vec{u} = (\upsilon, \omega)$, υ and ω represent the meridional and vertical motions, respectively. Consider the spherical nature of the planetary atmospheres, we define in our model the meridional coordinate y = aθ, where a is planetary radius, and θ is latitude defined to be -90° at the South Pole and 90° at the North Pole. For vertical coordinate, we adopt z = H ln(p_0/p), where p is pressure and p_0 is the reference pressure at z = 0 level, and H is the scale height of the atmosphere. The definition of velocity field for meridional motion υ and vertical motion ω via the coordinates can be rewritten as

$$\upsilon = -\frac{1}{\cos\theta} e^{z/H} \frac{\partial}{\partial z}(e^{-z/H}\psi). \tag{5.6}$$

$$\omega = \frac{1}{\cos\theta}\frac{\partial \psi}{\partial y}. \tag{5.7}$$

The eddy diffusion coefficient K in equation (5.3) is written as a 2 × 2 tensor in the 2-D model,

$$\mathrm{K} = \begin{pmatrix} \mathrm{K}_{yy} & \mathrm{K}_{yz} \\ \mathrm{K}_{zy} & \mathrm{K}_{zz} \end{pmatrix}.$$

Thus, the eddy diffusive fluxes $\bar{F} = -\mathrm{K}\bar{\nabla}\chi$ are parameterized by

$$F_y = -(\mathrm{K}_{yy}\frac{\partial \chi}{\partial y} + \mathrm{K}_{yz}\frac{\partial \chi}{\partial z}).$$

$$F_z = -(\mathrm{K}_{zy}\frac{\partial \chi}{\partial y} + \mathrm{K}_{zz}\frac{\partial \chi}{\partial z}).$$

Including all processes for equation (5.3), and using the stream function to represent velocity field, we derive the computational formula in our 2-D model as

$$\begin{aligned} &\frac{\partial \chi}{\partial t} - \frac{1}{\cos\theta}[e^{z/H}\frac{\partial}{\partial z}(e^{-z/H}\psi)\frac{\partial \chi}{\partial y} - \frac{\partial \psi}{\partial y}\frac{\partial \chi}{\partial z}] \\ &-\frac{1}{\cos\theta}\frac{\partial}{\partial y}\{\cos\theta(\mathrm{K}_{yy}\frac{\partial \chi}{\partial y} + \mathrm{K}_{yz}\frac{\partial \chi}{\partial z})\} \\ &-e^{z/H}\frac{\partial}{\partial z}\{e^{-z/H}(\mathrm{K}_{zy}\frac{\partial \chi}{\partial y} + \mathrm{K}_{zz}\frac{\partial \chi}{\partial z})\} \\ &= (P - L) \end{aligned} \tag{5.8}$$

To solve this equation numerically, we divide the atmosphere into 36 horizontal × 33 vertical boxes, as shown in Figure 5-1.

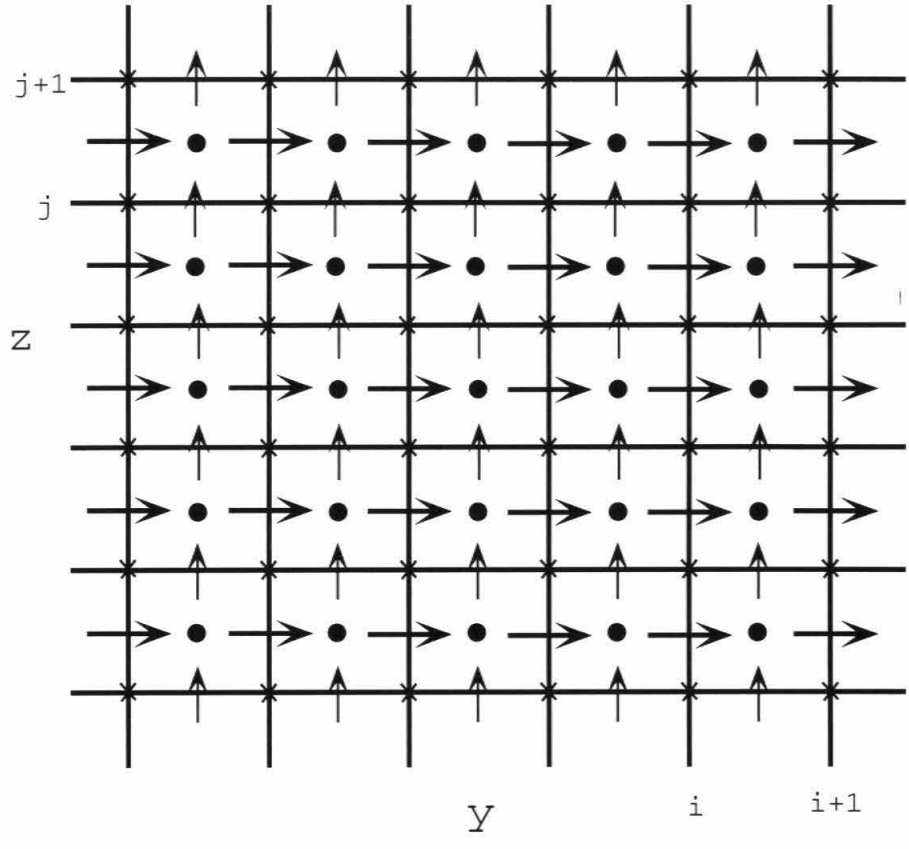

Figure 5-1. A schematic 2-D model. Special symbols in the figure indicate locations where various physical quantities are defined: crosses for stream function; solid points for mixing ratio and P, L rates; horizontal arrows for horizontal flux; vertical arrows for vertical flux.

The y-axis grids are 36 equally spaced from –87.5° to 87.5°, by an increment of 5° latitudes. The z-axis is 33 altitude grids from 270 mbar pressure level up to 0.1 mbar pressure level. Note that the mean mixing ratio χ is defined at the center of each grid box (the solid dots in Figure 5-1). The stream function ψ is defined at the corners of the grid boxes (crosses) so that differentiation of ψ can produce the appropriate

advection velocities. All horizontal and vertical fluxes are defined at the boundaries of each grid box.

We also describe the major components of the 2-D dynamical model in the following sub-sections.

5.2.1. Tracer

Our model adopts ethane (C_2H_6) for the tracer constituent. C_2H_6 is one of the most stable hydrocarbons in the upper atmosphere of Jupiter. From the comprehensive one-dimensional photochemical hydrocarbon model by Gladstone *et al.* [1996], major photochemical reactions for C_2H_6 occur at above 10^{-2} mbar pressure levels. In the lower stratosphere and the top of the troposphere (0.1 to 270 mbar) where our model operates, dynamical motion controls the distribution of C_2H_6. Therefore, we choose ethane as the tracer component so that the right-hand term (P - L) of equation (5.8) could be assumed to be zero.

5.2.2. Stream function

Stream function represents the mass conservative part of the residual circulation. We use the zonally averaged two-dimensional stream function introduced by West *et al.* [1992]. The authors calculated the annual-average diabatic circulation in the Jovian lower stratosphere and upper troposphere between 270 and 0.1 mbar by first estimating the zonal mean net radiative heating. The vertical component of the residual velocity field (the vertical advective velocity ω) was derived from the

balance between the zonal mean net radiative heating and adiabatic heating or cooling associated with subsidence or upwelling. The meridional velocity component (the horizontal pole ward advective velocity υ) was then derived as that required to satisfy the continuity equation with the vertical component. The meridional and vertical velocity components were then used to calculate the two-dimensional mass stream function by equation (5.6) and (5.7). The stream function of the circulation is shown in Figure 5-2.

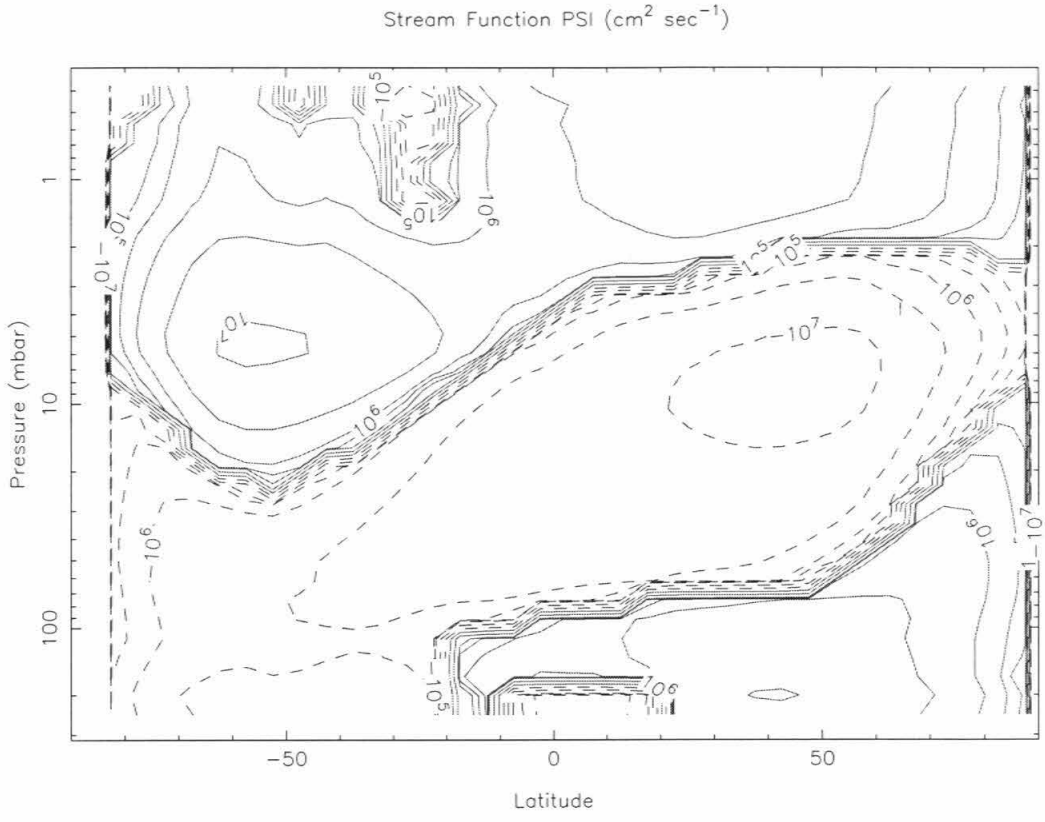

Figure 5-2. Two-dimensional map of the stream function derived from West *et al.* [1992]. The horizontal axis represents the latitude from -90° to +90°. The vertical axis represents altitude by atmospheric pressure levels. The unit of the stream function is g cm^{-1} sec^{-1}.

5.2.3. Meridional eddy diffusion coefficient (K_{yy})

West *et al.* [1992] also estimated the annual-average Eliassen-Palm (EP) flux divergence and Coriolis deflection of the meridional residual velocity. Friedson *et al.* [1999] used their derived EP flux divergence, incorporate with the assumption that large-scale, quasi-geostrophic eddies are primarily responsible for both the tracer transport and the wave-mean flow interaction in the stratosphere, to estimate the 2-D map of K_{yy}. Friedson *et al.* interpret the rapidly equatorward transported debris from the impact of Comet Shoemaker-Levy 9 by adopting the horizontal eddy diffusion coefficient K_{yy} in their 2-D dynamical model. Figure 5-3 shows the 2-D map of their derived K_{yy}. Negative values of K_{yy} were set to zero in the calculation to avoid numerical instability. We adopt these K_{yy} values shown in Figure 5-3 as the "normal" horizontal eddy diffusion coefficient parameter in our 2-D model.

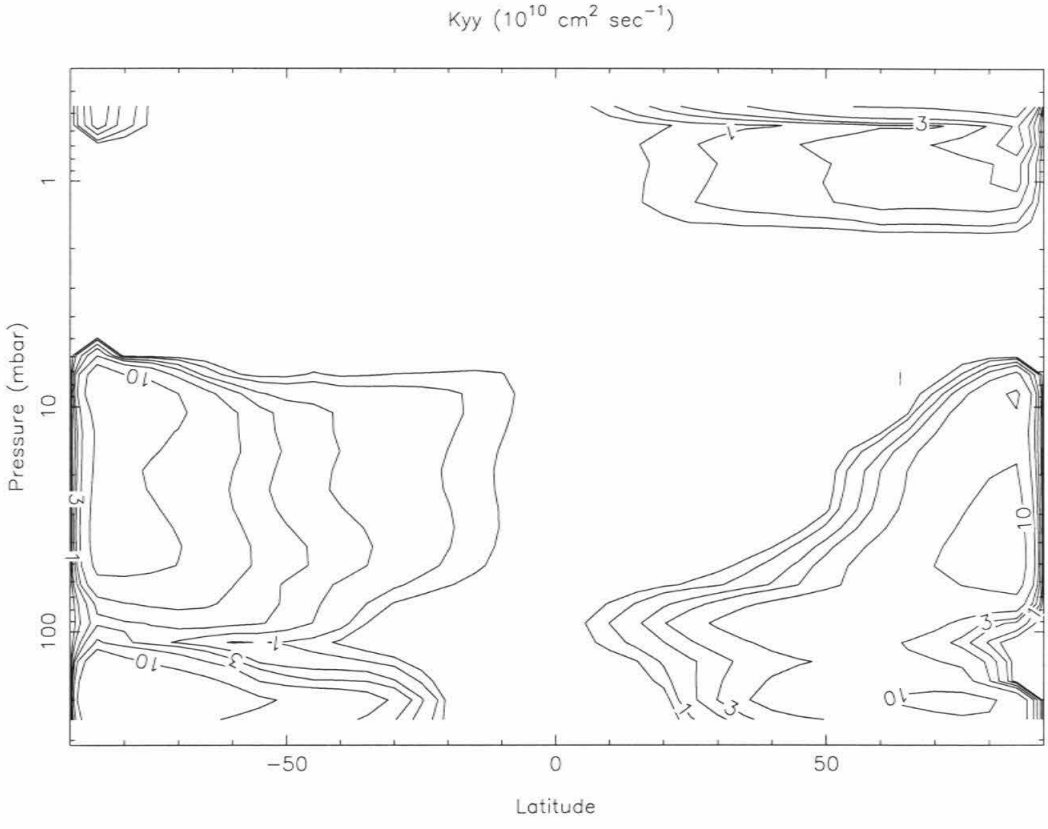

Figure 5-3. Two-dimensional map of the horizontal eddy diffusion coefficient K_{yy} derived from Friedson *et al.* [1999]. The horizontal axis represents the latitude from -90° to +90°. The vertical axis represents altitude by atmospheric pressure levels. The unit of the K_{yy} is 10^{10} cm^2 sec^{-1}.

5.2.4. Vertical eddy diffusion coefficient (K_{zz})

To evaluate the importance of the vertical eddy diffusion coefficient was one of the major motivations for our 2-D model. We adopt the K_{zz} value from the one-dimensional photochemical model by Gladstone *et al.* [1996]. The functional form of the eddy diffusion coefficient profile is

$$K(n) = K_H(n_H/n)^{\gamma} \qquad P \leq P_T$$

$$= K_T \qquad P > P_T$$

where P_T represents the pressure of the tropopause (pressure ~ 100 mbar). According to Gladstone et al.'s model, $K_H = 1.4 \times 10^6$ cm^2 sec^{-1}, $K_T = 1.0 \times 10^3$ cm^2 sec^{-1}, $n_H = 1.4 \times 10^{13}$ cm^{-3}, and $\gamma = 0.45$, for the Northern Equatorial Belt (NEB) region on Jupiter. Since there is not enough information for the latitude-dependence of the vertical eddy diffusion coefficient, we simply assumed that this NEB K_{zz} profile could be used at all latitudes by giving each latitude its own scaling factor. Note that the vertical eddy diffusion coefficient in the 1-D model parameterizes the bulk atmospheric vertical motion for the tracer. The 1-D "eddy diffusion coefficient" contains both advection and diffusion, or other dynamical terms. The scaling factor for K_{zz} at low latitudes near NEB should be smaller than unity.

5.2.5. Boundary flux

We assume the (*P-L*) term on the right-hand side of equation (5.8) zero, *i.e.* no chemical source or sink is allowed for C_2H_6 between 270 and 0.1 mbar in our model. However, there are external downward fluxes derived from the photochemically

active upper stratosphere of Jupiter. In our model, there must be some fluxes transported downward at the upper boundary (0.1 mbar level). As for the vertical eddy diffusion coefficient, boundary flux values at each latitude are not constrained except for the one at NEB region provided by the 1-D photochemical model. Gladstone *et al.*'s [1996] hydrocarbon model provided the downward C_2H_6 flux -1.4×10^9 cm^{-2} sec^{-1} at 0.1 mbar level (negative value denotes downward flux). Therefore, we take C_2H_6 downward flux at low latitudes -1.4×10^9 cm^{-2} sec^{-1}. We should point out that the 1-D hydrocarbon model by Gladstone *et al.* [1996] only considered C_2H_6 productions from CH_4 photodissociation by solar UV radiation. If the solar radiation is the only source for C_2H_6 formation at each latitude, the "normal" upper boundary flux at high latitudes must decrease due to the geometrical solar angle increases (a factor of $\cos\theta$, where θ increases from 0° to ±90°). However, extra sources of C_2H_6, such as hydrocarbon chemistry induced by energetic particles (Wong *et al.* 2000), or by lightning at mid-high latitudes, could provide larger fluxes than the "normal" fluxes at mid-high latitudes.

5.3. Simplified Radiative Transfer Method

The 2-D model results for ethane vertical and horizontal distribution will be compared to the infrared observations [Orton *et al.* 1989] via a radiative transfer model. However, detailed calculation over many latitudes is a time-consuming task. In this section, we try to develop a simplified and empirical radiative transfer computation method for quickly evaluating the 2-D modeling results at different latitudes.

For observations of the emission from planetary atmospheres, the radiative transfer integration starts at the top of the atmosphere and continues downward until some very large optical depth is reached,

$$I_\nu(\tau) = \int_0^\tau B_\nu(T(z))e^{-\tau'}d\tau', \tag{5.9}$$

where optical depth τ is defined by $d\tau = k_\nu(p)dz$, $k_\nu(p)$ is the absorption coefficient at pressure level p, and $B_\nu(T)$ is the Planck function for temperature T.

For numerical evaluation of the integration in a real atmosphere divided into N layers, the radiative transfer formula will be rewritten as following,

$$I_\nu = \sum_{i=1}^{N} B_\nu(T_i)(1-e^{-\Delta\tau_i})e^{-\sum_{j=1}^{i}(\Delta\tau_j)}, \tag{5.10}$$

where $\Delta\tau_i \equiv \int k_\nu(p)(dz/dp)dp$. This detailed radiative transfer model computes the emission and attenuation from the deepest level (i = 1) to the top of the atmosphere (i = N). Planck function for perfect black body radiation is used for computing emissions

from each atmospheric layer with temperature T_i.

To simplify the complex absorption and scattering calculations in the atmosphere where radiation passes through, we assume that the Jovian atmosphere above the upper troposphere could be divided into two regimes: an optically thin upper part, and an optically thick lower part. The lowest altitude level of the optically thin regime may be chosen at around optical depth unity level. The thermal emission originating from the optically thin atmosphere is simply the sum of Planck function at each layer times its abundance by assuming a transparent atmosphere. On the other hand, the emitted photons in the optically thick atmosphere may be absorbed at least once before they reach the highest level of the regime, so that the Planck function for thermal emission of the whole regime is taken at the highest level of this part. We also assume an empirical net attenuation factor f for the emission from the optically thick area. As a result, the "effective emission" for the planetary atmosphere for a specific species is thus proposed, by approximating empirically constant k_v(p) through the optically thick atmosphere.

$$I = \sum_{i=m+1}^{N} C_i B(T_i) dz + fB(T_m) \sum_{i=1}^{m} C_i dz , \qquad (5.11)$$

where C_i represents the concentration of the species at layer i, dz is the height of one specified layer, and $B(T_i)$ is the Planck function for atmospheric layer i with temperature T_i. The former item is thus for optically thin regime, and the latter item is for optically thick part. Layer m is the transition level, where optical depth may be equal to unity. Figure 5-4 shows the vertical structure of the assumed atmospheric layers by a schematic diagram. The shaded area is the optically thick regime, and the white area is optically thin.

A dashed horizontal line indicates the transition layer m.

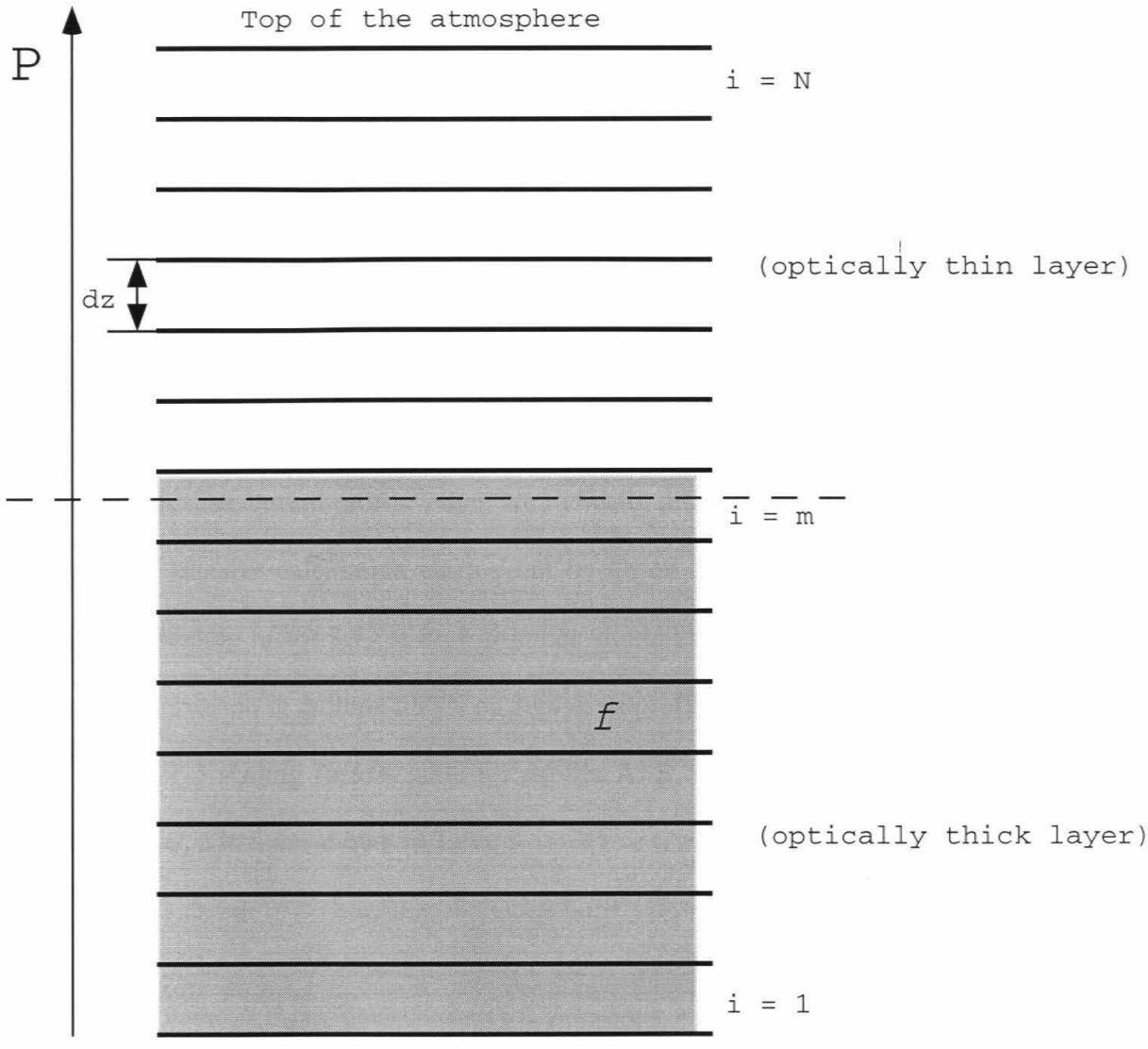

Figure 5-4. A schematic description of the two-layer simplified method described in this section. All grids included in the shaded area are assumed optically thick, and the blank area on the upper part denotes optically thin area. The dashed line represents transition level (i = m).

If the concentrations C_i and the temperature profile T_i for the atmosphere are known, the parameters for determining the effective emission I are the transition level m and the empirical attenuation factor f. For a given observation, if there are several choices for retrieval profile shapes that be scaled and equally well reproduce observation in a detailed radiative transfer model, is there a common parameter set m and f?

We first perform a typical 2-D model calculation in the lower stratosphere and upper troposphere of Jupiter, and then pick up the C_2H_6 vertical profiles (10^{-3} mbar < p < 300 mbar) for 55° N (Profile A), 1° S (Profile B), and 57° S (Profile C). Figure 5-5 shows these vertical C_2H_6 distribution profiles, they are radically different in relative shape. The detailed radiative transfer calculation carried out by Orton indicates that, for example, profile A times a scaling factor 3.73 at each altitudes would lead to an equally good fit for C_2H_6 infrared observation at latitude 55° N on Jupiter as profile B times 1.39, or profile C times 3.0. The 3 × 3 scaling factors table for profile A, B, C for observed emission at latitude 55° N, 1° S, 57° S are shown in Table 5-1.

Table 5-1. Radiative transfer model scaling factors for the profile A, B, and C at 55° N, 1° S, and 57° S

	Profile A	Profile B	Profile C
55° N	3.73	1.39	3.00
1° S	0.84	0.33	0.82
57° S	1.48	0.56	1.48

Retrieving the parameters m and f in each latitude is based on the fact that the reproduced emissions are nearly identical at specific latitude by adopting the three corresponding C_2H_6 profiles. We carried out the numerical calculations (equation 5.11) iteratively to determine a combination of m and f that yields the closest values for effective emission. For one certain latitude (55° N, 1° S, 57° S), therefore, statistical average deviation from the mean will be calculated for effective emissions by profiles A, B, and C. We thus find the smallest average deviation value among all possible combinations of m and f. The retrieved parameters m and f for latitude 55° N are m = 42 (pressure level 0.08 mbar), and f = 0.03; for 1° S, m = 43 (pressure level 0.063 mbar), and f = 0.017; and for 57° S, m = 42 (pressure level 0.08 mbar), and f = 0.018. Applying these values for m and f to the three latitudes, the effective emission for profiles A, B, and C are shown in Table 5-2. Note that the emission as modeled with equation (5.11) is independent of assumed profile with a maximum deviation of < 8%.

Table 5-2. The effective emission (ergs cm^{-2} s^{-1}) calculated by adopting the statistically best m and f for the profile A, B, and C at 55° N, 1° S, and 57° S.

	Profile A	Profile B	Profile C	average deviation from the mean
55° N	1.22×10^{13}	1.03×10^{13}	1.13×10^{13}	5.48%
1° S	2.15×10^{12}	1.89×10^{12}	2.02×10^{12}	4.23%
57° S	4.38×10^{12}	3.46×10^{12}	3.92×10^{12}	7.81%

In the absence of doing full detailed radiative transfer computations for every 2-D model run output, the advantage of our simplified radiative transfer approach is that it provides a quick evaluation for the 2-D model result. We will calculate the effective emissions via equation (5.11) at the three latitudes for each 2-D model run by providing its C*i* abundance profile and using m = 42 (0.126 mbar level), f = 0.03 at 55° N, m = 43 (0.063 mbar level), f = 0.017 at 1° S, and m = 42 (0.126 mbar level), f = 0.018 at 57° S. We will then compare the resulting effective emissions I_s with the corresponding average of A, B, and C cases for each latitude. If a 2-D model yields close effective emissions at 55° N, 1° S, and 57° S to the "observed" values in Table 5-1, we wish to claim that the model matches the observations.

5.4. Model Results

The first case will test the advection-only 2-D dynamical transport. We set the "normal" stream function, which is the non-adjusted stream function introduced by West *et al.* [1992], but with zero diffusion terms, K_{yy} and K_{zz}. The boundary downward C_2H_6 fluxes are -1.4×10^9 cm^{-2} sec^{-1} at around low latitude region maximum, and decrease by cosine angle to the high latitude region. In Table 5-3, we describe all these dynamical processes as "Case 1". The values shown for rows of "stream function", "K_{yy}", and "K_{zz}" are scaling factors time their "normal" values. As mentioned above, we adopt the West *et al.*'s [1992] stream function as normal stream function, the Friedson *et al.*'s [1999] K_{yy} coefficient as normal K_{yy} values, and the 1/10 of Gladstone *et al.*'s [1996] 1-D vertical eddy diffusion coefficients as normal K_{zz} values. The zeros in both K_{yy} and K_{zz} represent ignoring meridional and vertical eddy diffusions in this case.

Table 5-3: 2-D Model Cases

Latitude	-82.5°	-62.5°	-37.5°	-7.5°	7.5°	37.5°	62.5°	82.5°
Case 1								
Stream function[1]	1.0	1.0	1.0	1.0	1.0	1.0	1.0	1.0
K_{yy} (× Normal[2])	0	0	0	0	0	0	0	0
K_{zz} (× Normal[3])	0	0	0	0	0	0	0	0
Boundary flux[4]	-4.3×10^{7}	-4.6×10^{8}	-7.9×10^{8}	-1.4×10^{9}	-1.4×10^{9}	-7.9×10^{8}	-4.6×10^{8}	-4.3×10^{7}
Case 2								
Stream function[1]	1.0	1.0	1.0	1.0	1.0	1.0	1.0	1.0
K_{yy} (× Normal[2])	1.0	1.0	1.0	1.0	1.0	1.0	1.0	1.0
K_{zz} (× Normal[3])	1.0	1.0	1.0	1.0	1.0	1.0	1.0	1.0
Boundary flux[4]	-4.3×10^{7}	-4.6×10^{8}	-7.9×10^{8}	-1.4×10^{9}	-1.4×10^{9}	-7.9×10^{8}	-4.6×10^{8}	-4.3×10^{7}
Case 2-2								
Stream function[1]	1.0	1.0	1.0	1.0	1.0	1.0	1.0	1.0
K_{yy} (× Normal[2])	1.0	1.0	1.0	1.0	1.0	1.0	1.0	1.0
K_{zz} (× Normal[3])	0	0	0	0	0	0	0	0
Boundary flux[4]	-4.3×10^{7}	-4.6×10^{8}	-7.9×10^{8}	-1.4×10^{9}	-1.4×10^{9}	-7.9×10^{8}	-4.6×10^{8}	-4.3×10^{7}
Case 3								
Stream function[1]	1.0	1.0	1.0	1.0	1.0	1.0	1.0	1.0
K_{yy} (× Normal[2])	1.0	1.0	1.0	1.0	1.0	1.0	1.0	1.0
K_{zz} (× Normal[3])	1.0	1.0	1.0	1.0	1.0	1.0	1.0	1.0
Boundary flux[4]	-1.0×10^{8}	-1.0×10^{10}	-2.0×10^{9}	-1.4×10^{9}	-1.4×10^{9}	-2.0×10^{9}	-5.0×10^{10}	-1.0×10^{8}
Case 4								
Stream function[1]	1.0	1.0	1.0	1.0	1.0	1.0	1.0	1.0
K_{yy} (× Normal[2])	1.0	1.0	1.0	1.0	1.0	1.0	1.0	1.0
K_{zz} (× Normal[3])	0.5	0.5	0.5	0.5	0.5	0.5	0.5	0.5
Boundary flux[4]	-1.0×10^{8}	-4.0×10^{9}	-1.8×10^{9}	-1.4×10^{9}	-1.4×10^{9}	-1.8×10^{9}	-3.0×10^{10}	-1.0×10^{8}
Case 5								
Stream function[1]	0.5	0.5	0.5	0.5	0.5	0.5	0.5	0.5
K_{yy} (× Normal[2])	0.5	0.5	0.5	0.5	0.5	0.5	0.5	0.5
K_{zz} (× Normal[3])	1.0	1.0	1.0	1.0	1.0	1.0	1.0	1.0

Boundary flux[4]	-1.0×10^{8}	-4.0×10^{9}	-1.8×10^{9}	-1.4×10^{9}	-1.4×10^{9}	-1.8×10^{9}	-3.0×10^{10}	-1.0×10^{8}
Case 6								
Stream function[1]	0.1	0.1	0.1	0.1	0.1	0.1	0.1	0.1
K_{yy} (× Normal[2])	0.1	0.1	0.1	0.1	0.1	0.1	0.1	0.1
K_{zz} (× Normal[3])	1.0	1.0	1.0	1.0	1.0	1.0	1.0	1.0
Boundary flux[4]	-1.0×10^{8}	-2.0×10^{9}	-1.8×10^{9}	-1.4×10^{9}	-1.4×10^{9}	-1.8×10^{9}	-1.0×10^{10}	-1.0×10^{8}

[1]The "Normal" stream function is derived from *West et al.* (1992); see text.

[2]The "Normal" K_{yy} map is derived from *Friedson et al.* (1999); see text.

[3]The "Normal" K_{zz} vertical profile is 0.1 × eddy diffusion coefficient used in 1-D photochemical model (*Gladstone et al.* 1996); see text

[4]The boundary flux is the C_2H_6 flux at 0.1 mbar pressure level, with unit of $cm^{-2}sec^{-1}$. The minus sign denotes downward fluxes.

The 2-D model is composed of 36 horizontal grids for latitudes from –87.5° to +87.5°, and 33 vertical grids for pressure levels from 270 mbar to 0.1 mbar. Photochemical sources or sinks for C_2H_6 are ignored in this model. The total time run for every model is ~ 2×10^{10} seconds, roughly equal to 4 Jovian years, to reach a dynamically steady state. The model result for case 1 is shown in Figure 5-5.

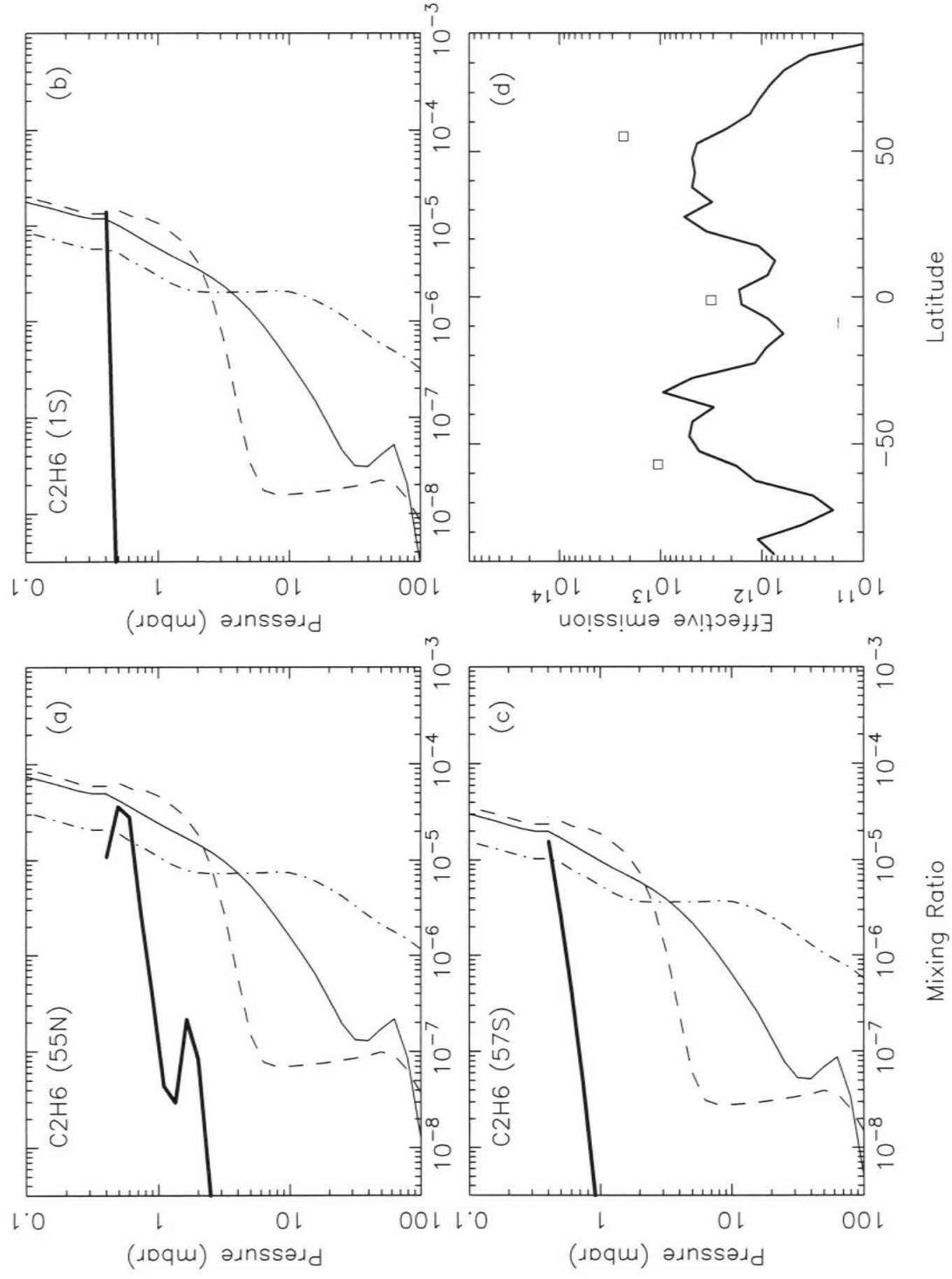

Figure 5-5. Model result for Case 1. See text for details of the figure.

There are four panels shown in each case's result figure. The top-left (a), top-right (b), and bottom-left (c) panels show C_2H_6 vertical mixing ratio profiles at 55° N, 1° S, and 57° S, respectively. The thin-solid line, thin-dashed line, and thin-dash-dot lines in the panels represent the scaled profiles A, B, and C described in the last section, respectively. All three thin line profiles agree with the infrared observation at the specific latitude. The thick line in each panel represents our model results at the specific location. The three panels are chosen to represent C_2H_6 mixing ratios at northern high latitudes, low latitudes, and southern high latitudes.

In the bottom-right (d) panel, we present the result calculated by the simplified radiative transfer method. The three square points are taken from Table 5-2 with average values for profiles A, B, and C. The line in this panel represents the latitudinal distribution of the effective emission for our model's resultant C_2H_6 concentrations calculated by the same radiative transfer method. Note that the y-axis is represented by logarithm scale, so the average deviation < 10% for the three profiles is almost as small as the area covered by square symbols. Therefore, the good fit to observations should be close enough to the open squares shown in this panel.

Case 1 is obviously not a good fit because it ignores all diffusion terms in the 2-D model. The second experiment is proposed to use all "normal" parameters, including the stream function, K_{yy}, and K_{zz}, as mentioned above. The boundary fluxes of C_2H_6 are also assumed the same cosine angle dependent values as we adopted in Case 1. This "normal" 2-D model (Case 2 as shown in Table 5-3) shows totally different results compared with Case 1 (Figure 5-6).

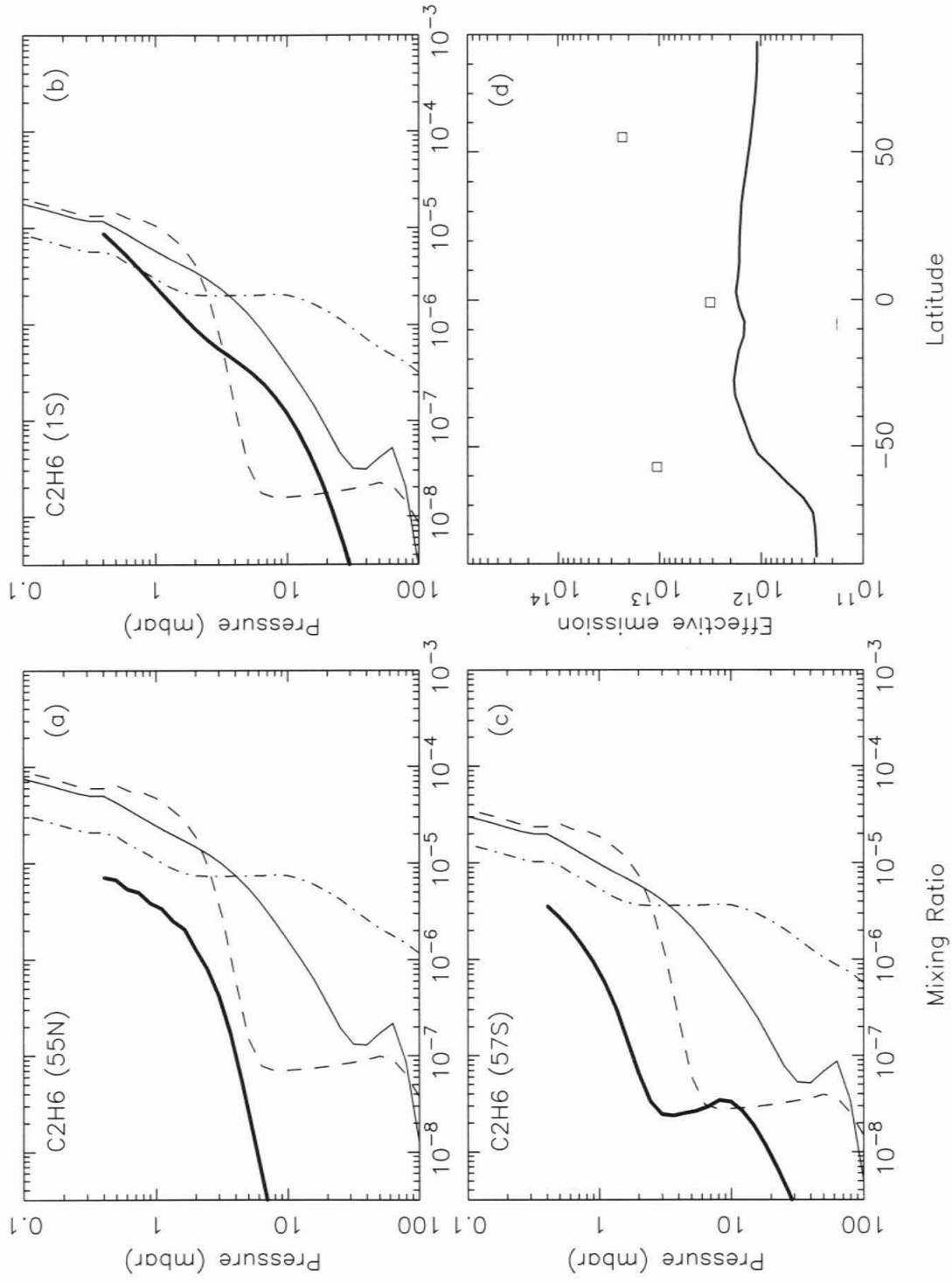

Figure 5-6. Model result for Case 2. See text for details of the figure and the model.

Figure 5-6 has an identical layout as Figure 5-5. The result of Case 2 differs largely to Case 1. The bottom-right panel of Figure 5-6 shows a much more smooth latitudinal distribution comparing to Figure 5-5, and the vertical C_2H_6 mixing ratio profiles shown in the other three panels have obviously different patterns. However, Case 2, the "standard" dynamical case, is unlikely to explain the observation. The effective emissions calculated at 57° S, 7° S, and 55° N are obviously missing the fit.

The significant difference between Case 1 and Case 2 basically originated from the introduction of K_{zz}. The vertical eddy diffusion coefficient influences the model by faster mixing between different altitude levels. We test this effect by removing K_{zz} from Case 2 in Case 2-2. Figure 5-7 shows that C_2H_6 are much more abundant above 1 mbar than the lower altitude levels at each latitude without K_{zz} in the model.

As mentioned above, we must confirm the result by computing the "real" emission by detailed radiative transfer model. Figure 5-8 shows the comparisons between the observed spectra (dashed lines) and the synthetic spectra (solid lines) generated by radiative transfer model at three latitudes. The mismatch in brightness temperatures at two peaks (814.4 cm^{-1}, 815.7 cm^{-1}) support our calculations (Figure 5-6).

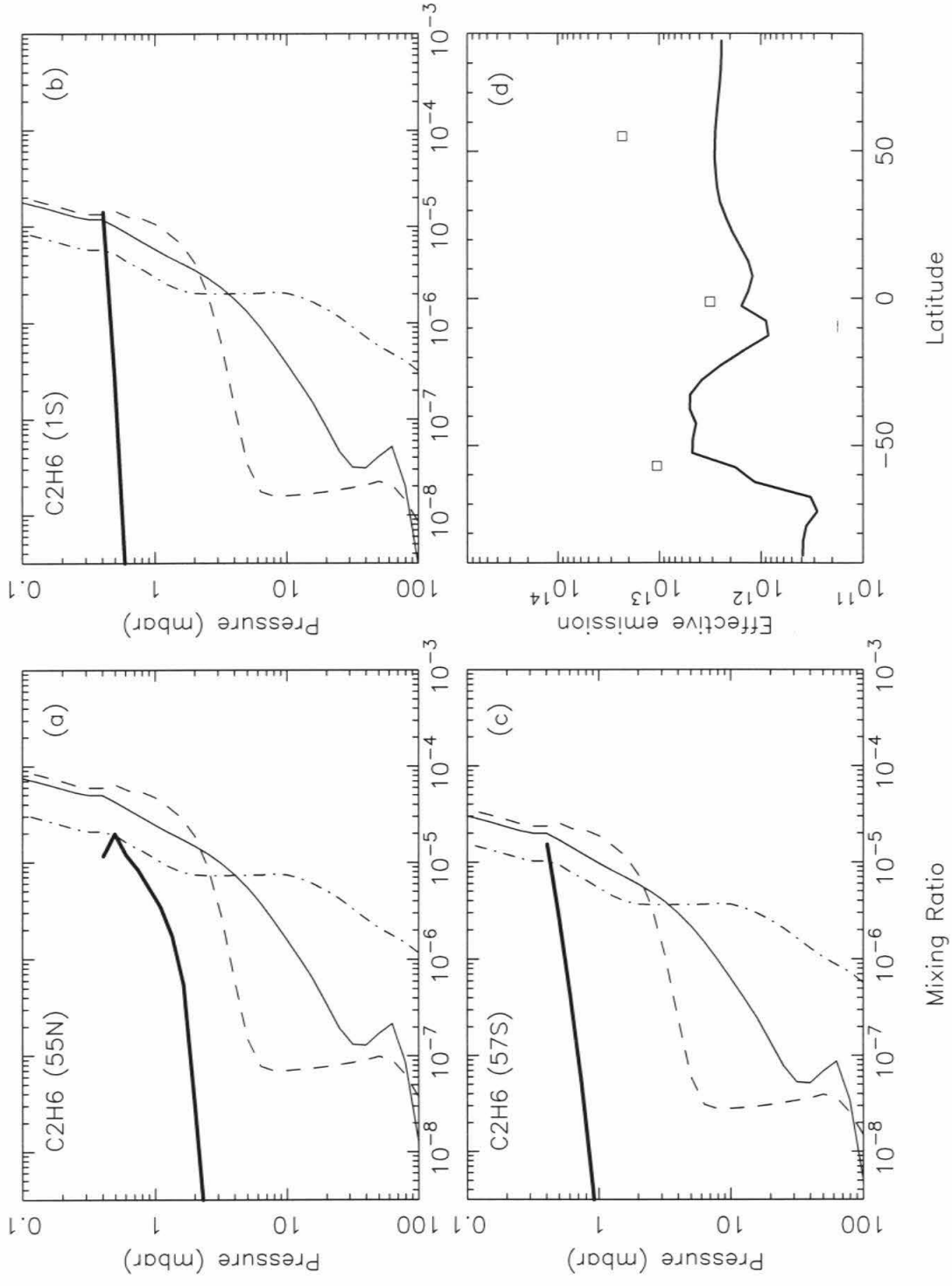

Figure 5-7. Model result for Case 2-2. See text for details of the figure and the model.

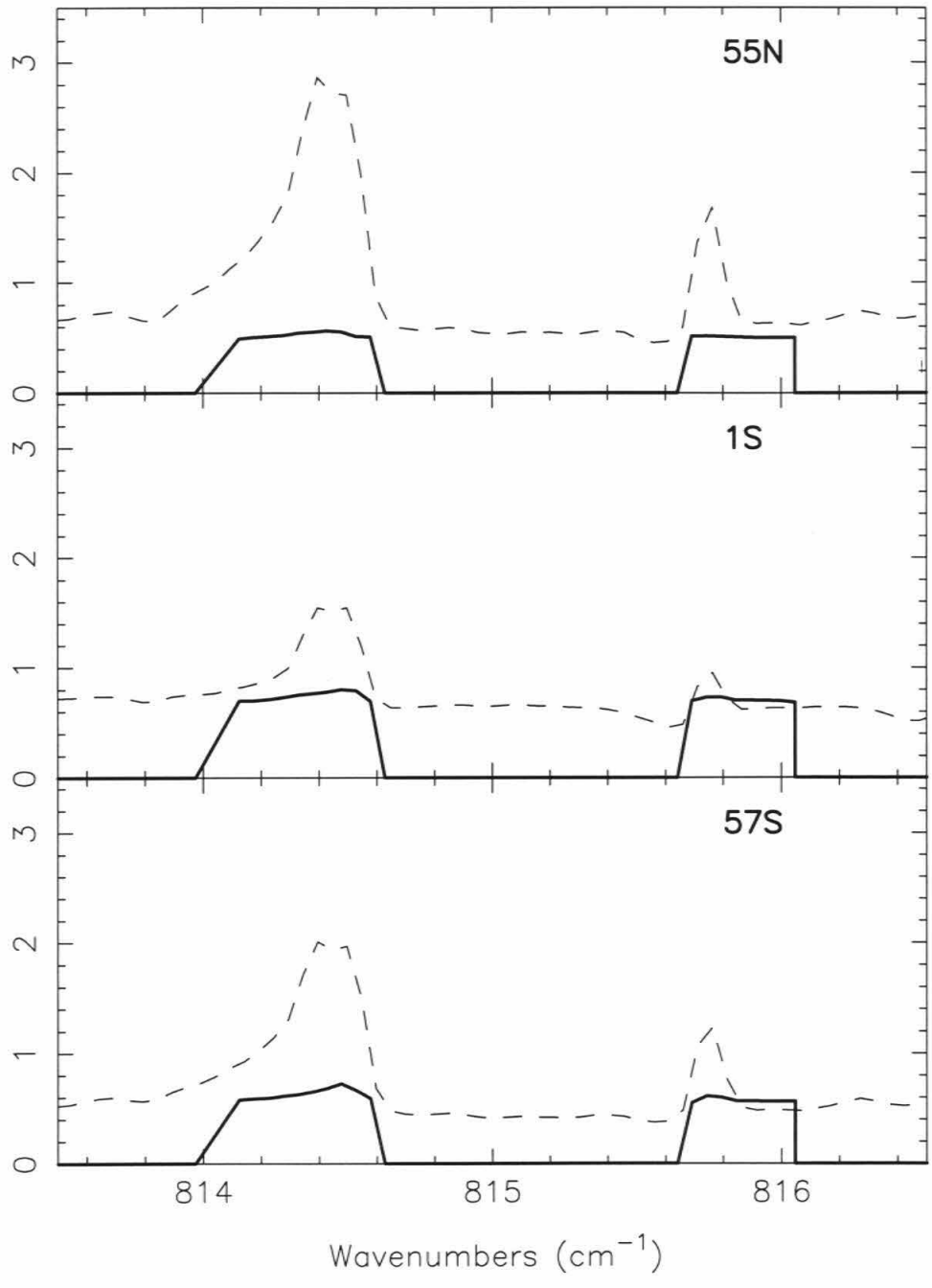

Figure 5-8. Comparisons for the observed spectra and the synthetic spectra computed by radiative transfer model. These panels show results of Case 2 (Figure 5-6) at 55° N, 1° S, and 57° S, respectively. The dashed line denotes the observed spectrum by Orton *et al.* [1989]; The solid line is for model synthetic spectrum.

The enhanced emissions by C_2H_6 at high latitudes strongly suggest larger C_2H_6 productions than at low latitudes, which imply some other sources of the hydrocarbons near polar region. Assuming that these possible sources occur at upper stratosphere, we thus expect enhanced C_2H_6 downward fluxes may provide a solution. We tried to maintain all the "normal" dynamical processes unchanged in our model, and seek for boundary fluxes that can match the observation. In Case 3, maximum C_2H_6 downward fluxes around ±60° latitude are assumed almost two orders of magnitude larger than the fluxes in Case 2. We set the maximum fluxes -5.0×10^{10} cm^{-2} sec^{-1} for northern high-latitude region, and -1.0×10^{10} cm^{-2} sec^{-1} for southern high-latitude region. The 2-D model result of Case 3 is shown in Figure 5-9. The comparison between the synthetic thermal emission spectra and the observed spectra at three specific latitudes is also shown in Figure 5-10. The simplified radiative transfer result (right-bottom panel in Figure 5-9) and the synthetic spectra around 814.4 cm^{-1} and 815.7 cm^{-1} peaks reveal that this case fit well to the observation. The simplified radiative transfer method is thus proved to be a useful tool for fast evaluating the 2-D model result.

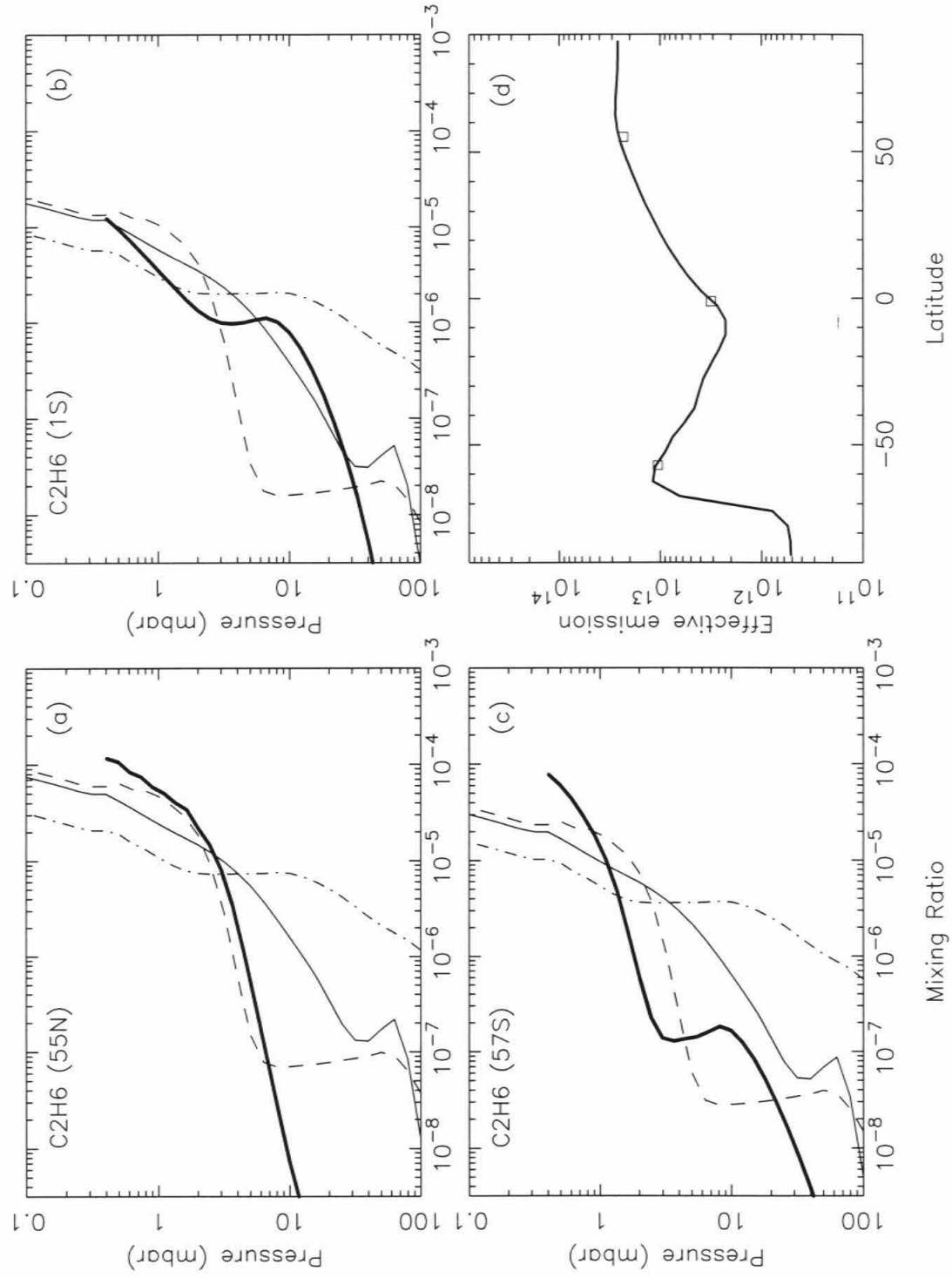

Figure 5-9. Model result for Case 3. See text for details of the figure and the model.

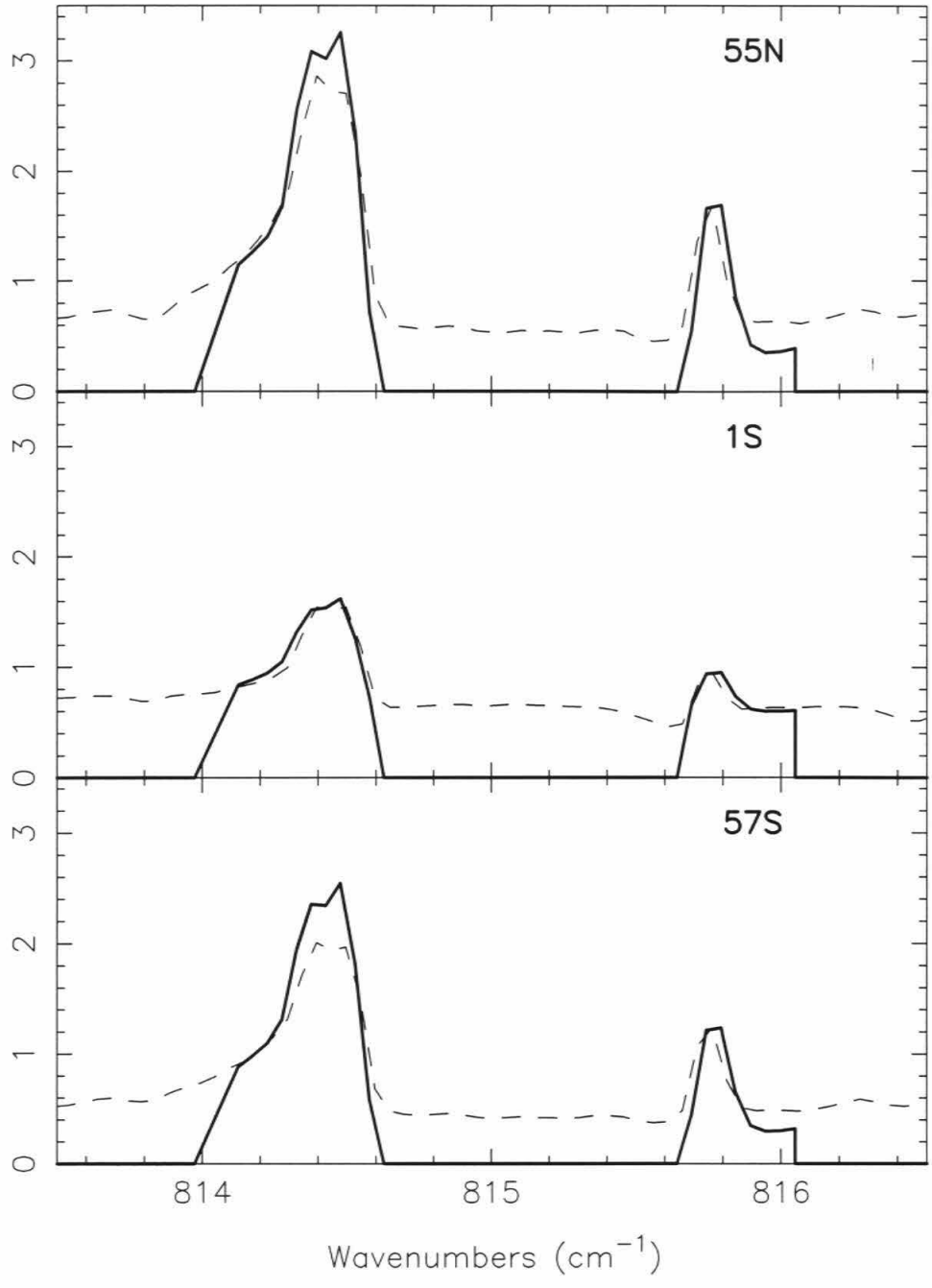

Figure 5-10. Comparisons for the observed spectra and the synthetic spectra computed by radiative transfer model. These panels show results of Case 3 (Figure 5-9) at 55° N, 1° S, and 57° S, respectively. The dashed line denotes the observed spectrum by Orton *et al.* [1989]; The solid line is for model synthetic spectrum.

Case 3 is the model that we can derive the best fit by using all the "normal" dynamical processes. However, the maximum C_2H_6 downward fluxes up to -5.0×10^{10} cm^{-2} sec^{-1} at high latitudes is unlikely since it requires two orders of magnitude larger hydrocarbon productions in the weaker insolation area. High-energy electrons precipitation in the polar region provides the power of aurorae ~20 times the solar EUV power from the Sun [Perry *et al.* 1999]. It is still at least a factor of 2 short for explaining the large C_2H_6 downward flux. Therefore, we proposed to test lower boundary flux models by adjusting their dynamical parameters. In Case 4, we set the maximum fluxes -3.0×10^{10} cm^{-2} sec^{-1} for northern high-latitude region, and -4.0×10^{9} cm^{-2} sec^{-1} for southern high-latitude region. These values were chosen to reduce the C_2H_6 boundary flux for matching in the range of aurorae estimate. If stream function and K_{yy} are kept the values as those used in previous cases, K_{zz} must be decreased to obtain the fitted curve. The 2-D model result of Case 4 is shown in Figure 5-11, and the corresponding radiative transfer spectra are shown in Figure 5-12.

The other option for adjusting dynamical processes is to change the stream function and/or the horizontal eddy diffusion coefficient K_{yy}. Case 5 is obtained by reducing the stream function and K_{yy} to half their normal values, keeping K_{zz} its normal value as in Case 2 and Case 3. Both Case 4 and Case 5 use the same boundary fluxes. The C_2H_6 profiles of Case 5 are shown in Figure 5-13.

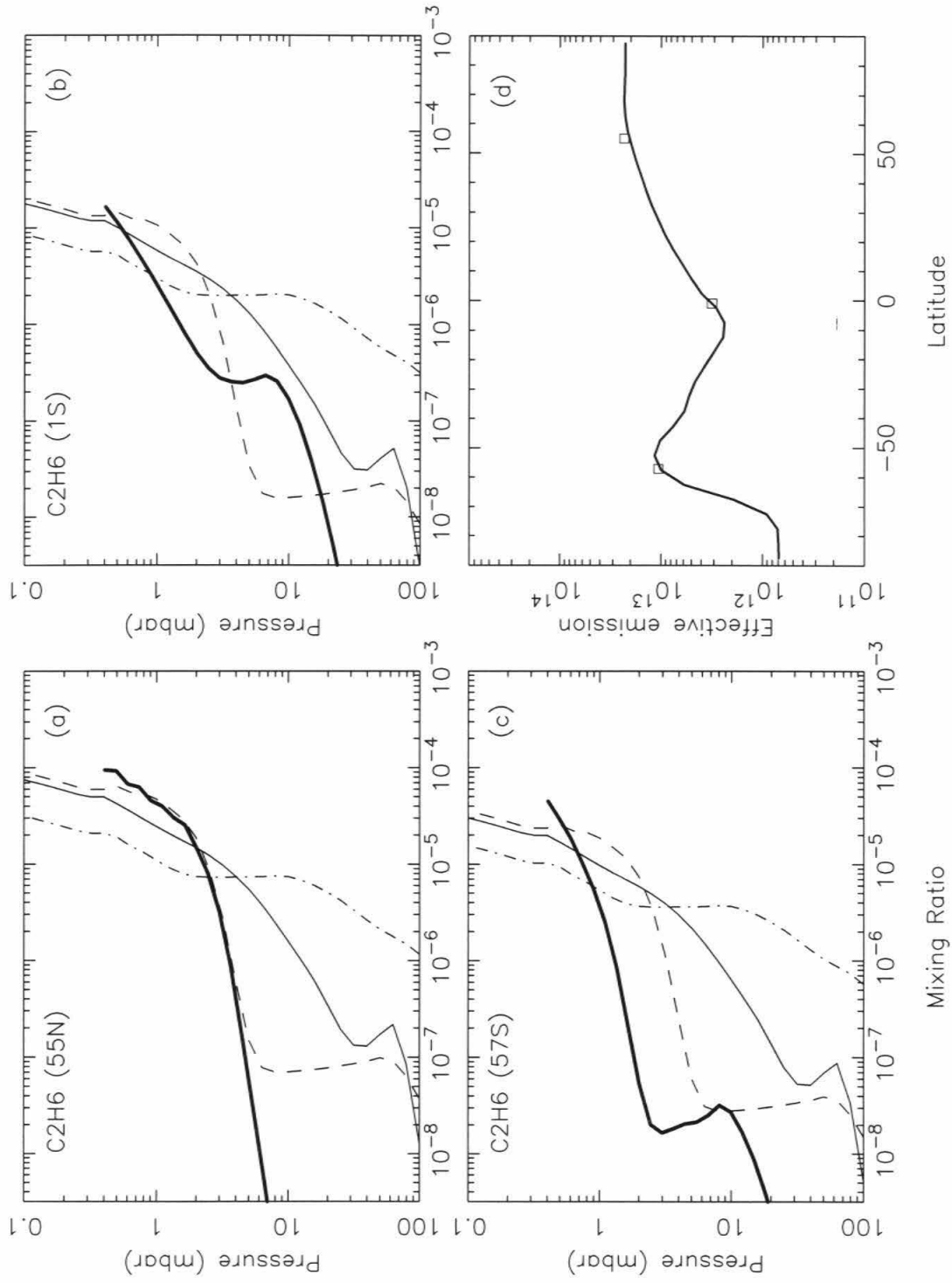

Figure 5-11. Model result for Case 4. See text for details of the figure and the model.

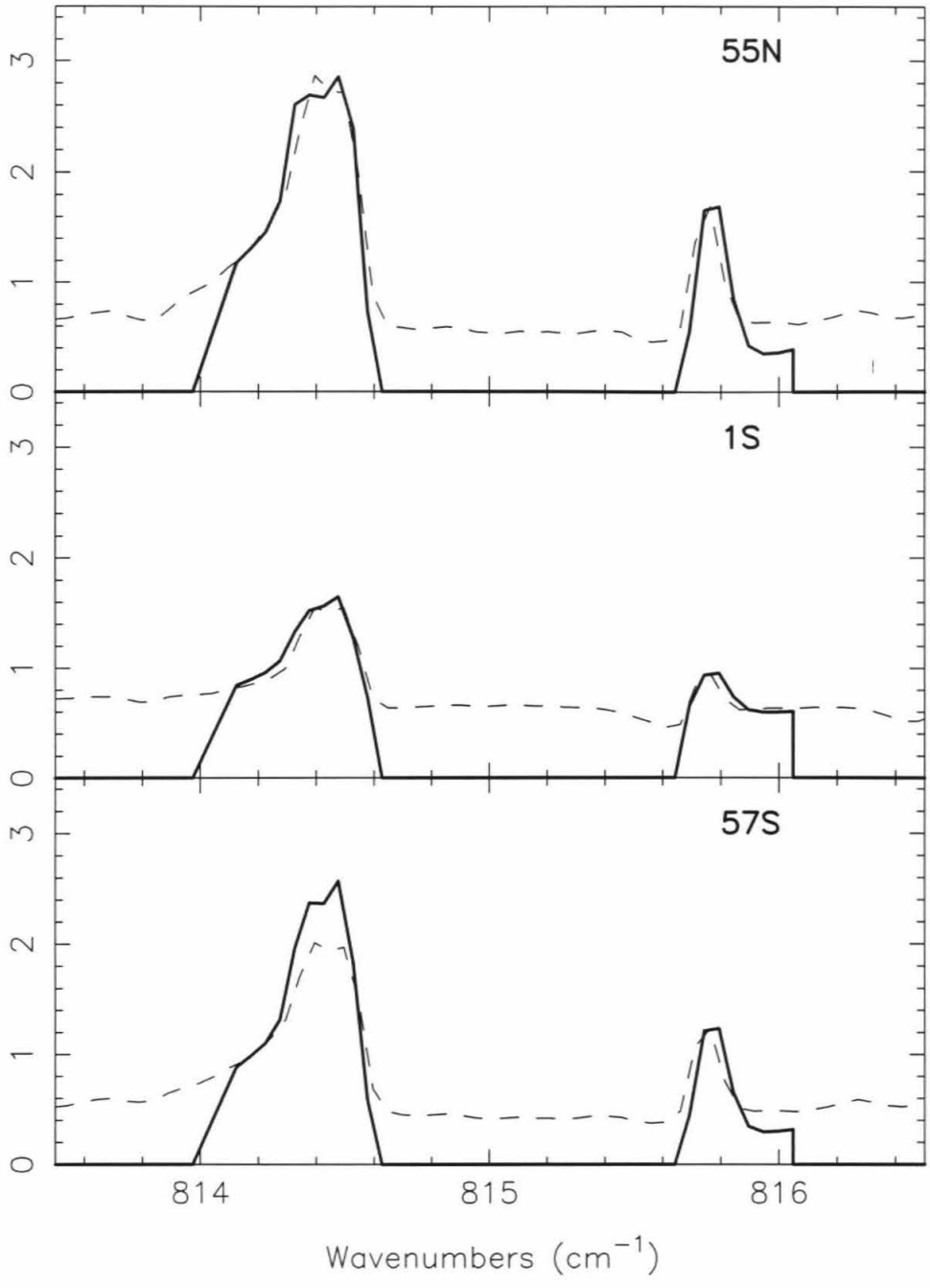

Figure 5-12. Comparisons for the observed spectra and the synthetic spectra computed by radiative transfer model. These panels show results of Case 4 (Figure 5-11) at 55° N, 1° S, and 57° S, respectively. The dashed line denotes the observed spectrum by Orton *et al.* [1989]; The solid line is for model synthetic spectrum.

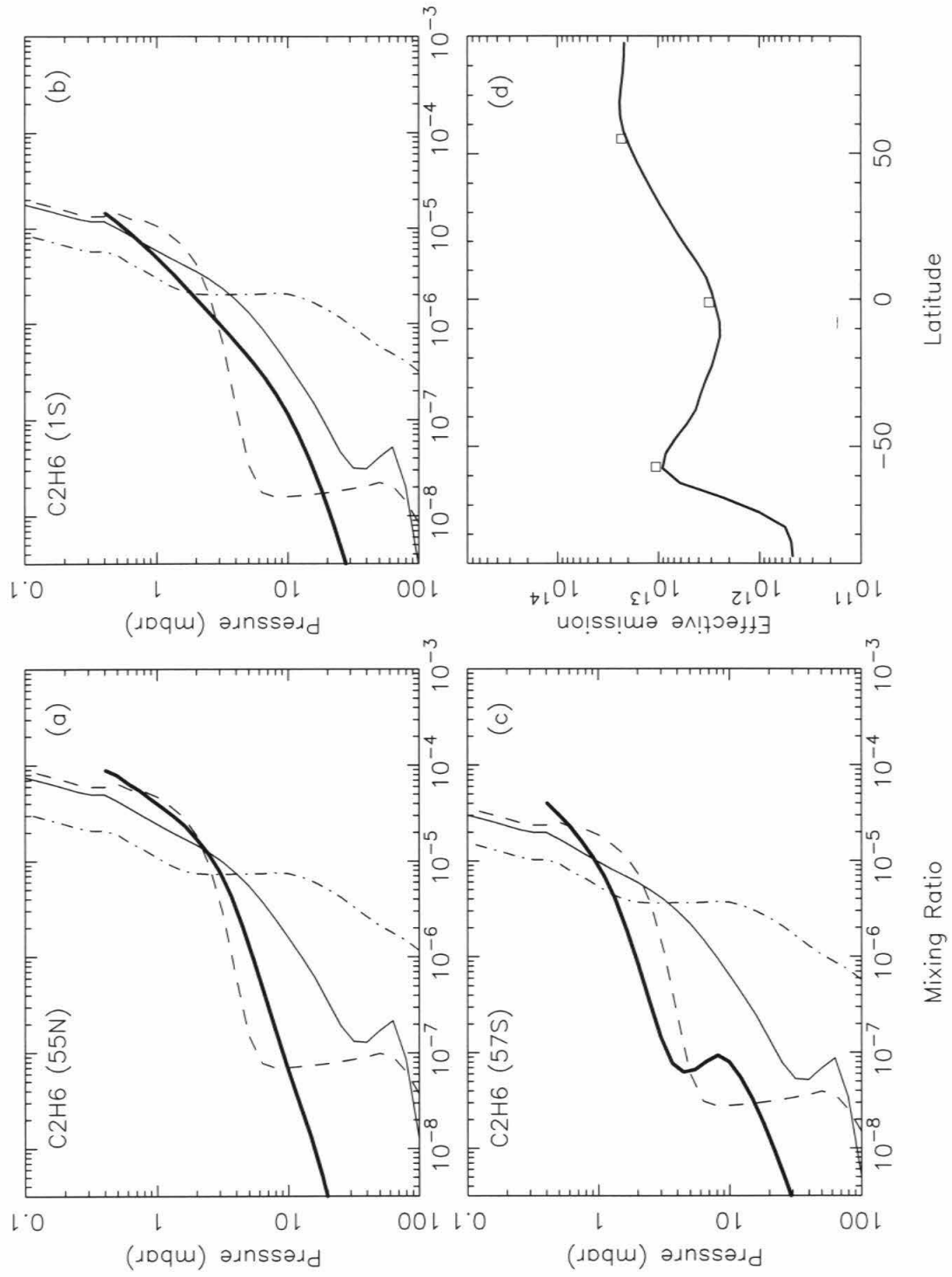

Figure 5-13. Model result for Case 5. See text for details of the figure and the model.

Decreasing C_2H_6 boundary flux leads to slower dynamical motion processes to fit the observation. We test the further smaller flux in our 2-D model. The parameters that are adopted for Case 6 are shown in Table 5-3. The maximum C_2H_6 downward fluxes in the northern hemisphere is -2.0×10^9 cm^{-2} sec^{-1}, and the value in the southern hemisphere is -1.0×10^9 cm^{-2} sec^{-1}. Figure 5-14 shows that even very small stream functions and K_{yy} values fail to fit the points by using the simplified calculations.

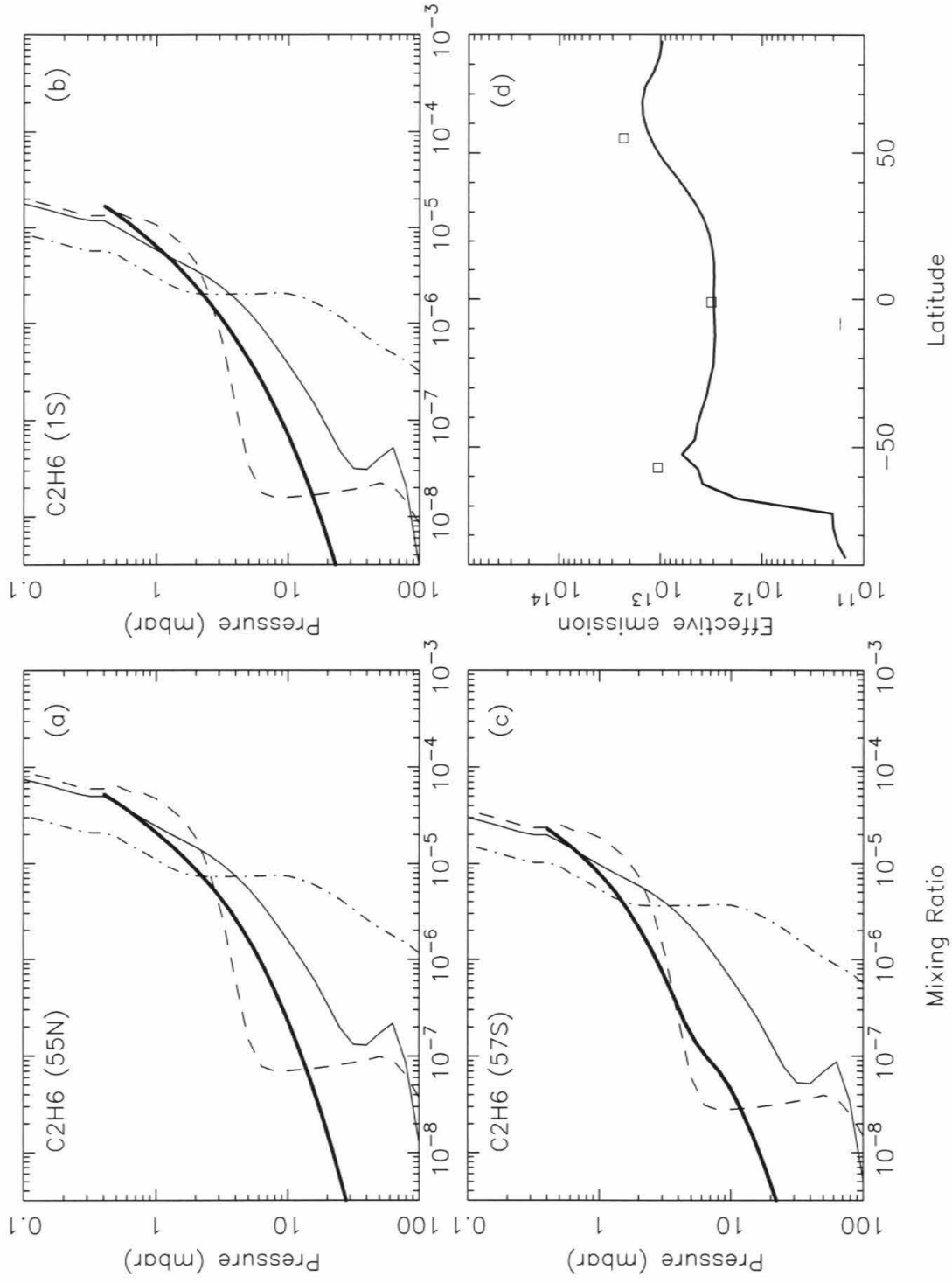

Figure 5-14. Model result for Case 6. See text for details of the figure and the model.

5.5. Discussions and Conclusions

We have carried out a series of C_2H_6 2-D modeling studies in the lower stratosphere and upper troposphere (270 mbar – 0.1 mbar) of Jupiter. There are four major dynamical processes considered in our model: advection (represented by stream functions), horizontal eddy diffusion (K_{yy}), vertical eddy diffusion coefficient (K_{zz}), and downward flux at the upper boundary of our model. The model results are constrained by infrared observations [Orton *et al.* 1989]. We also developed a simplified radiative transfer calculation model for more efficient evaluation of the results.

Vertical eddy diffusion has been included in our model, and we found that it has significant impact for the C_2H_6 vertical distribution by mixing between different altitude levels. We estimate the magnitude of K_{zz} to be one tenth of the bulk vertical motion derived from the typical 1-D model for Jupiter. However, quantification of diffusion in the Jovian atmospheric dynamical processes is unknown and very controversial. We can only conclude that the vertical eddy diffusion term in the 2-D model is necessary.

Given the fact that the thermal emission spectrum at high latitudes of Jupiter is enhanced compared to the equatorial region, energy sources other than solar UV radiation are necessary to produce more hydrocarbons in the upper atmosphere. From our test models, at least 20 times the productions of C_2H_6 above 0.1 mbar level is required to provide enough boundary fluxes in our model. Possible energy sources at high latitudes of Jupiter include the precipitating high-energy particles along the magnetic field lines (aurorae), or lightning. A recent study of aromatic compound chemistry at high latitudes

of Jupiter by Wong *et al.* [2000] confirms the occurrence of ion-induced chemical activities near the polar region. However, the relatively large C_2H_6 downward fluxes derived from our 2-D models need to be verified by other observations.

The model needs a very large input of C_2H_6 at high latitudes to fit the observation if we adopted the stream function derived from West *et al.* [1992], and the horizontal eddy diffusion coefficient suggested by Friedson *et al.* [1999], without changing their original values. Our test models show that these processes should be reduced to some extent in accordance with a reasonable estimate of the boundary fluxes. Reducing K_{zz} to a very small value is unlikely because this results in too large concentration difference between 1 mbar and 10 mbar pressure levels that contradict the Voyager IRIS observations [Sada *et al.* 1998]. Slower motions of advection and horizontal eddy diffusion, incorporated with moderate C_2H_6 downward fluxes, are required for explaining the observation.

References

Chapter 1

Bézard, B., H. Feuchtgruber, and Th. Encrenaz 1998, Detection of methyl radicals (CH_3) on Saturn, *Astron. Astrophys.*, **334**, L41-L44.

Bézard, B., P. N. Romani, H. Feuchtgruber, and Th. Encrenaz 1999, Detection of the methyl radical on Neptune, *Astrophys. J.*, **515,** 868-872.

Friedson, A. J., R. A. West, A. K. Hronek, N. A. Larsen, and N. Dalal 1999. Transport and Mixing in Jupiter's Stratosphere Inferred from Comet S-L9 Dust Migration. *Icarus.* **138**, 141 – 156.

Lee, A. Y. T., Y. L. Yung, and J. Moses 2000, Photochemical modeling of CH_3 abundances in the outer solar system, *J. Geophys. Res.*, **105**, E8,20,207-20,225.

Weisstein, E. W. and E. Serabyn 1996. Submillimeter line search in Jupiter and Saturn. *Icarus* **123**, 23 - 36.

West, R. A., A. J. Friedson, and J. F. Appleby 1992. Jovian Large-Scale Stratospheric Circulation. *Icarus.* **100**, 245 - 259.

Chapter 2

Ajello, J. M. 1990, Solar minimum Lyman α sky background observations from Pioneer Venus orbiter ultraviolet spectrometer: Solar wind latitude variation, *J. Geophys. Res., 95*, 14,855-14,861.

Allen, M., Y. L. Yung, and J. W. Waters 1981. Vertical transport and photochemistry in the terrestrial mesosphere and lower thermosphere (50 – 120 km). *J. Geophys. Res.* **86**, 3617 - 3627.

DeMore, W. B., S. P. Sander, D. M. Golden, R. F. Hampson, M. J. Kurylo, C. J. Howard, A. R. Ravishankara, C. E. Kolb, and M. J. Molina 1992, Chemical Kinetics and Photochemical Data for Use in Stratospheric Modeling. *Evaluation Number 10*, JPL Publication 92-20, Jet Propulsion Laboratory.

Marrero, T. R., and E. A. Mason 1972, Gaseous diffusion coefficients, *J. Phys. Chem. Ref. Data,* **1**, 3-118.

Strobel, D. F. 1973, The photochemistry of methane in the Jovian atmosphere, *J. Atmos. Sci.,* **26**, 906-911.

Strobel, D. F. 1975, Aeronomy of the major planets: Photochemistry of ammonia and hydrocarbons, *Rev. Geophys.,* **13**, 372-382.

Torr, M. R. and D. G. Torr, J. 1985, Ionization frequencies for solar cycle 21: Revised, *J. Geophys. Res.*, **90**, 6675-6678.

Troe, J. 1977a, Theory of thermal unimolecular reactions at low pressure, I, Solutions of the master equation, *J. Chem. Phys.*, **66**, 4745-4757.

Troe, J. 1977b, Theory of thermal unimolecular reactions at low pressure, II, Strong collision rate constants, applications, *J. Chem. Phys.*, **66**, 4758-4775.

Yung, Y. L., M. Allen, and J. P. Pinto 1984, Photochemistry of the atmosphere of Titan: Comparison between model and observations, *Astrophys. J. Suppl. Ser.,* **55**, 465-506.

Chapter 3

Ajello, J. M. 1990, Solar minimum Lyman α sky background observations from Pioneer Venus orbiter ultraviolet spectrometer: Solar wind latitude variation, *J. Geophys. Res.*, **95**, 14,855-14,861.

Allen, M. 1989, Chemical kinetics: A planetary review, *First International Conference on Laboratory Research for Planetary Atmospheres, NASA Conf. Publ., CP-3077*, 443-450.

Ashfold, M. N. R., I. R. Lambert, D. H. Mordaunt, G. P. Morley, and C. M. Western 1992, Photofragment translational spectroscopy, *J. Phys. Chem.*, **96**, 2938-2949.

Atreya, S. K., S. G. Edgington, Th. Encrenaz, and H. Feuchtgruber 1998, Observations of C_2H_2 on Uranus and CH_3 on Saturn: Implications for atmospheric vertical mixing in the Voyager and ISO epochs, and a call for relevant laboratory measurements; *The Universe as Seen by ISO, Eur. Space Agency Spec. Publ., ESA SP-427.*

Baulch, D. L., et al., Warnatz 1992, Evaluated kinetic data for combustion modeling, *J. Phys. Chem. Ref. Data,* **21**, 411-734.

Bézard, B., P. N. Romani, and B. J. Conrath 1991, Hydrocarbons in Neptune stratosphere from Voyager infrared observations, *J. Geophys. Res.*, **96**, 18,961-18,975.

Bézard, B., H. Feuchtgruber, and Th. Encrenaz 1998, Detection of methyl radicals (CH_3) on Saturn, *Astron. Astrophys.*, **334**, L41-L44.

Bézard, B., P. N. Romani, H. Feuchtgruber, and Th. Encrenaz 1999, Detection of the methyl radical on Neptune, *Astrophys. J.*, **515,** 868-872.

Bishop, J., S. K. Atreya, F. Herbert, and P. N. Romani 1990, Reanalysis of Voyager 2 UVS occultations at Uranus: Hydrocarbon mixing ratios in the equatorial stratosphere, *Icarus,* **88**, 448-464.

Bishop, J., P. N. Romani, and S. K. Atreya 1998, Voyager 2 ultraviolet spectrometer solar occultations at Neptune: Photochemical modeling of the 125-165 nm lightcurves, *Planet. Space Sci.*, **46**, 1-20.

Broadfoot, A. L. et al. 1989, Ultraviolet spectrometer observations of Neptune and Triton, *Science,* **246**, 1459-1466.

Brouard, M., M. T. MacPherson, and M. J. Pilling 1989, Experimental and RRKM

modeling study of the CH_3 + H and CH_3 + D reactions, *J. Phys. Chem.,* **93**, 4047-4059.

Caldwell, J., R. Wagner, and K. H. Fricke 1988, Observations of Neptune and Uranus below 2000 A with the IUE, *Icarus,* **74**, 133-140.

Courtin, R., D. Gautier, A. Marten, B. Bézard, and R. Hanel 1984, The composition of Saturn's atmosphere at northern temperate latitudes from Voyager IRIS spectra: NH_3, PH_3, C_2H_2, C_2H_6, CH_3D, CH_4, and the Saturnian D/H isotopic ratio, *Astrophys. J.,* **287**, 899-916.

Coustenis, A., B. Bézard, and D. Gautier 1989, Titan's atmosphere from Voyager infrared observations, 1, The gas-composition of Titan's equatorial region, *Icarus,* **80**, 54-76.

Coustenis, A., B. Bézard, D. Gautier, A. Marten, and R. Samuelson 1991, Titan's atmosphere from Voyager infrared observations, 3, Vertical distributions of hydrocarbons and nitriles near Titan's north pole, *Icarus,* **89**, 152-167.

de Graauw, T., et al. 1997, First results of ISO-SWS observations of Saturn: Detection of CO_2, CH_3C_2H, C_4H_2 and tropospheric H_2O, *Astron. Astrophys.,* **321**, L13-L16.

Du, H., J. P. Hessler, and P. J. Ogren 1996, Recombination of methyl radicals, 1, New Data between 1175 and 1750 K in the falloff region, *J. Phys. Chem.,* **100**, 974-983.

Forst, W. 1991, Microcanonical variational theory of radical recombination by inversion of interpolated partition function, with examples: CH_3 + H, CH_3 + CH_3, *J. Phys. Chem.,* **95**, 3612-3620.

Gladstone, G. R. 1993, Photochemistry in the primitive solar nebula, *Science,* **261**, 1058.

Gladstone, G. R., M. Allen, and Y. L. Yung 1996, Hydrocarbon photochemistry in the atmosphere of Jupiter, *Icarus,* **119**, 1-52.

Heck, A. J. R., R. N. Zare, and D. W. Chandler 1996, Photofragment imaging of methane, *J. Chem. Phys.,* **104**, 4019-4030.

Heinemann, P., R. Hofmann-Sievert, and K. Hoyermann 1986, Direct study of the reactions of vinyl radicals with hydrogen and oxygen atoms, *Symp. Int. Combust., 21st,* 5-873.

Herbert, F., B. R. Sandel, and R. V. Yelle 1987, The upper atmosphere of Uranus–EUV occultations observed by Voyager 2, *J. Geophys. Res.,* **92**, 15,093-15,109.

Hole, K. J., and M. F. R. Mulcahy 1969, The photolysis of biacetyl and the third-body

effect on the combination of methyl radicals, *J. Phys. Chem.*, **73**, 177-185.

Klippenstein, J. K., and L. B. Harding 1999, A direct transition state theory based study of methyl radical recombination kinetics, *J. Phys. Chem.*, **103**, 9388-9398.

Kostiuk, T. P., N. Romani, and F. Espenak 1992, Stratospheric ethane on Neptune: Comparison of groundbased and Voyager IRIS retrievals, *Icarus*, **99**, 353-362.

Langford, A. O., H. Petek, and C. B. Moore 1983, Collisional removal of $CH_2(^1A_1)$: Absolute rate constants for atomic and molecular collisional partners at 295 K, *J. Chem. Phys.*, **78**, 6650-6659.

Lara, L. M., E. Lellouch, J. J. LopezMoreno, and R. Rodrigo 1996, Vertical distribution of Titan's atmospheric neutral constituents, *J. Geophys. Res.*, **101**, 23,261-23,283.

Laufer, A. H., E. P. Gardner, T. L. Kwok, and Y. L. Yung 1983, Computations and estimates of rate coefficients for hydrocarbon reactions of interest to the atmospheres of the outer solar system, *Icarus*, **56**, 560-567.

Lee, A. Y. T., Y. L. Yung, and J. Moses 2000, Photochemical modeling of CH_3 abundances in the outer solar system, *J. Geophys. Res.*, **105**, E8,20,207-20,225.

Lindal, G. F., D. N. Sweetnam, and V. R. Eshleman 1985, The atmosphere of Saturn: An analysis of the Voyager radio occultation measurements, *Astron. J.*, **90**, 1136-1146.

Lindal, G. F. 1992, The atmosphere of Neptune: An analysis of radio occultation data acquired with Voyager 2, *Astron. J.*, **103**, 967-982.

MacPherson, M. T., M. J. Pilling, and M. J. C. Smith 1983, The pressure and temperature dependence of the rate constant for methyl radical recombination over the temperature range 296-577 K, *Chem. Phys. Lett.*, **94**, 430-433.

MacPherson, M. T., M. J. Pilling, and M. J. C. Smith 1985, Determination of the absorption cross section for CH_3 at 216.36 nm and the absolute rate constant for methyl radical recombination over the temperature range 296-577 K, *J. Phys. Chem.*, **89**, 2268-2274.

Monks, P. S., F. L. Nesbitt, W. A. Payne, M. Scanlon, and L. J. Stief 1995, Absolute rate constant and product branching ratios for the reaction between H and C_2H_3 at T=213 and 298 K, *J. Phys. Chem.*, **99**, 17,151-17,159.

Mordaunt, D. H., I. R. Lambert, G. P. Morley, M. N. R. Ashford, R. N. Dixon, and C. M. Western 1993, Primary product channels in the photodissociation of methane at

121.6 nm, *J. Chem. Phys.*, **98**, 2054-2065.

Moses, J. I. 1991, Photochemistry and aerosol formation in Neptune's atmosphere, Ph.D. thesis, Calif. Inst. of Technol., Pasadena.

Moses, J. I., B. Bézard, E. Lellouch, G. R. Gladstone, H. Feuchtgruber, and M. Allen 2000a, Photochemistry of the upper atmosphere of Saturn, I, Hydrocarbon chemistry and comparisons with ISO observations, *Icarus,* **143**, 244-298.

Moses, J. I., B. Bézard, E. Lellouch, G. R. Gladstone, H. Feuchtgruber, and M. Allen 2000b, Photochemistry of the upper atmosphere of Saturn, II, Effects of an external oxygen influx, *Icarus,* in press.

Pilling M. J., and J. A. Robertson 1977, Flash photolysis of ketene, photolysis mechanism and rate constants for singlet and triplet methylene, *J. Chem. Soc. Faraday Trans. 1,* **73**, 968-984.

Robertson, S. H., M. J. Pilling, D. L. Baulch, and N. J. B. Green 1995, Fitting of pressure-dependent kinetic rate data by master equation/inverse Laplace transform analysis, *J. Phys. Chem.*, **99**, 13,452-13,460.

Romani, P. N. 1996, Recent rate constant and product measurements of the reactions $C_2H_3 + H_2$ and $C_2H_3 + H$ – Importance for photochemical modeling of hydrocarbons on Jupiter, *Icarus,* **122**, 233-241.

Romani, P. N., J. Bishop, B. Bézard, and S. K. Atreya 1993, Methane photochemistry on Neptune: Ethane and acetylene mixing ratios and haze production, *Icarus,* **106**, 442-463.

Sada, P. V., G. L. Bjoraker, D. E. Jennings, G. H. McCabe, and P. N. Romani 1998, Observations of CH_4, C_2H_6, and C_2H_2 in the stratosphere of Jupiter, *Icarus,* **136**, 192-201.

Sillesen, A., E. Ratajczak, and P. Pagsberg 1993, Kinetics of the reactions $H + C_2H_4 \rightarrow C_2H_5$, $H + C_2H_5 \rightarrow 2CH_3$, and $CH_3 + C_2H_5 \rightarrow$ Products studied by pulse radiolysis combined with infrared diode laser spectroscopy, *Chem. Phys. Lett.*, **201**, 171-177.

Slagle, I. R., D. Gutman, J. W. Davies, and M. J. Pilling 1988, Study of the recombination reaction $CH_3 + CH_3 \rightarrow C_2H_6$, 1, Experiment, *J. Phys. Chem.*, **92**, 2455-2462.

Slanger, T. G., and G. Black 1982, Photodissociation channels of 1216 A for H_2O, NH_3, and CH_4, *J. Chem. Phys.*, **77**, 2432-2437.

Smith, N. S., and F. Raulin 1999, Modeling of methane photolysis in the reducing atmospheres of the outer solar system, *J. Geophys. Res.*, **104**, 1873-1876.

Strobel, D. F. 1973, The photochemistry of methane in the Jovian atmosphere, *J. Atmos. Sci.*, **26**, 906-911.

Strobel, D. F. 1975, Aeronomy of the major planets: Photochemistry of ammonia and hydrocarbons, *Rev. Geophys.*, **13**, 372-382.

Strobel, D. F. 1983, Photochemistry of the reducing atmospheres of Jupiter, Saturn, and Titan, *Int. Rev. Phys. Chem.*, **3**, 145-176.

Summers, M. E., and D. F. Strobel 1989, Photochemistry of the atmosphere of Uranus, *Astrophys. J.*, **346**, 495-508.

Toublanc, D., J. P. Parisot, J. Brillet, D. Gautier, F. Raulin, and C. P. McKay 1995, Photochemical modeling of Titan's atmosphere, *Icarus*, **113**, 2-26.

Troe, J. 1977a, Theory of thermal unimolecular reactions at low pressure, I, Solutions of the master equation, *J. Chem. Phys.*, **66**, 4745-4757.

Troe, J. 1977b, Theory of thermal unimolecular reactions at low pressure, II, Strong collision rate constants, applications, *J. Chem. Phys.*, **66**, 4758-4775.

Van den Bergh, H. E. 1976, The recombination of methyl radicals in the low pressure limit, *Chem. Phys. Lett.*, **43,** 201-204.

Wagner, A. F., and D. M. Wardlaw 1988, Study of the recombination reaction $CH_3 + CH_3 \rightarrow C_2H_6$, 2, Theory, *J. Phys. Chem.*, **92**, 2462-2471.

Yung, Y. L., and W. B. DeMore 1999, *Photochemistry of Planetary Atmospheres*, Oxford Univ. Press, New York.

Yung, Y. L., M. Allen, and J. P. Pinto 1984, Photochemistry of the atmosphere of Titan: Comparison between model and observations, *Astrophys. J. Suppl. Ser.*, **55**, 465-506.

Chapter 4

Allen, M., Y. L. Yung, and G. R. Gladstone 1992. The relative abundance of ethane to acetylene in the Jovian stratosphere. *Icarus.* **100**, 527 - 533.

Allen, M., Y. L. Yung, and J. W. Waters 1981. Vertical transport and photochemistry in the terrestrial mesosphere and lower thermosphere (50 – 120 km). *J. Geophys. Res.* **86**, 3617 - 3627.

Anders, E. and N. Grevesse 1989. Abundances of the elements: Meteoritic and solar. *Geochim. Cosmochim. Acta* **53**, 197 - 214.

Appleby, J. F. and J. S. Hogan 1984. Radiative-convective equilibrium models of Jupiter and Saturn. *Icarus.* **59**, 336 - 366.

Arthur, N. L. and I. A. Cooper 1997. Arrhenius parameters for the reactions of H atoms with PH_3 and AsH_3. *J. Chem. Soc. Faraday Trans.* **93**, 521 - 524.

Atreya, S. K., 1986. The relative abundance of ethane to acetylene in the Jovian stratosphere. *Icarus.* **100**, 527 - 533.

Baulch, D. L., C. J. Cobos, R. A. Cox, C. Esser, P. Frank, Th. Just, J. A. Kerr, M. J. Pilling, J. Troe, R. W. Walker, and J. Warnatz 1992. Evaluated kinetic data for combustion modeling. *J. Phys. Chem. Ref. Data* **21**, 411 - 734.

Becker, K. H., B. Engelhardt, H. Geiger, R. Kurtenbach, and P. Wiesen 1993. Temperature dependence of the reactions of CH radicals with NO, NH_3 and N_2O in the range 200-1300 K. *Chem. Phys. Lett.* **210**, 135 - 140.

Bjoraker, G. L., H. P. Larson, and V. G. Kunde 1986. The gas composition of Jupiter derived from 5-μm airborne spectroscopic observations. *Icarus.* **66**, 579 - 609.

Borunov, S., V. Dorofeeva, I. Khodakovsky, P. Drossart, E. Lellouch, and T. Encrenaz 1995. Phosphorus chemistry in the atmosphere of Jupiter: A reassessment. *Icarus.* **113**, 460 - 464.

Bosco, S. R., W. D. Brobst, D. F. Nava, and L. J. Stief 1983. The reaction $NH_2 + PH_3 \rightarrow NH_3 + PH_2$: Absolute rate constant measurement and implication for NH_3 and PH_3 photochemistry in the atmosphere of Jupiter. *J. Geophys. Res.* **88,** 8543 - 8549.

Bregman, J. D., D. F. Lester, and D. M. Rank 1975. Observation of the ν2 band of PH_3 in the atmosphere of Saturn. *Astrophys. J. Lett.* **202**, L55 – L56.

Chen, F., D. L. Judge, R. C. Y. Wu, J. Caldwell, P. White, and R. Wagener 1991. High-resolution, low-temperature photoabsorption cross sections of C_2H_2, PH_3, AsH_3, and GeH_4, with application to Saturn's atmosphere. *J. Geophys. Res.* **96**, 17519 - 17527.

Conrath, B. P. and P. J. Gierasch 1984. Global variation of the para hydrogen fraction in Jupiter's atmosphere and implications for dynamics of the outer planets. *Icarus.* **57**, 184 - 204.

Drossart, P., T. Encrenaz, V. Kunde, R. Hanel, and M. Combess 1982. An estimate of the PH_3, CH_3D, and GeH_4 abundances on Jupiter from the Voyager IRIS data at 4.5 μm. *Icarus.* **49**, 416 - 426.

Drossart, P., T. Encrenaz, and A. Tokunaga 1984. Variability of phosphine on Jupiter from 5-μm spectroscopy. *Icarus.* **60**, 613 - 620.

Drossart, P., E. Lellouch, B. Bézard, J. P. Maillard, and G. Tarrago 1990. Jupiter: Evidence for a phosphine enhancement at high northern latitudes. *Icarus.* **83**, 248 - 253.

Davidson, D. F., K. Kohse-Hoinghaus, A. Y. Chang, and R. K. Hanson 1990. A pyrolysis mechanism for ammonia. *Int. J. Chem. Kinet.* **22**, 513 - 535.

Dove, J. E. and W. S. Nip 1979. A shock-tube study of ammonia pyrolysis. *Can. J. Chem.* **57**,689 - 701.

Edgington, S. G., S. K. Atreya, and L. M. Trafton 1998. On the latitude variation of ammonia, acetylene, and phosphine altitude profiles on Jupiter from HST faint object spectrograph observations. *Icarus* **133**, 192 - 209.

Encrenaz, T., M. Combess, and Y. Zeau 1978. The spectrum of Jupiter between 10 and 13 μ: An estimate of the Jovian $^{15}N/^{14}N$ ratio. *Astron. Astrophys.* **70**, 29 - 36.

Encrenaz, T., M. Combess, and Y. Zeau 1980. The spectrum of Jupiter between 8 and 9 μ: Estimates of the Jovian C/H and D/H ratios. *Astron. Astrophys.* **84**, 148 - 153.

Encrenaz, T., E. Serabyn, and E. W. Weisstein 1996. Millimeter spectroscopy of Uranus

and Neptune: Constraints on the CO and PH3 tropospheric abundances. *Icarus* **124**, 616 - 624.

Fegley, B. Jr. and K. Lodders 1994. Chemical models of the deep atmospheres of Jupiter and Saturn. *Icarus* **110**, 117 - 154.

Gehring, Von M., K. Hoyermann, H. Wagner, and J. Wolfrum 1971. Die reaktion von atomarem wasserstoff mit hydrazine. *Ber. Bunsenges. Phys. Chem.* **75**, 1287 - 1294.

Gladstone, G. R., M. Allen, and Y. L. Yung 1996. Hydrocarbon photochemistry in the upper atmosphere of Jupiter. *Icarus* **119**, 1 - 52.

Griffith, C. A., B. Bézard, T. Owen, and D. Gautier 1992. The tropospheric abundances of NH_3 and PH_3 in Jupiter's Great Red Spot from Voyager IRIS observations. *Icarus* **98**, 82 - 93.

Grodon, S., W. Mulac, and P. Nangia 1971. Pulse radiolysis of ammonia gas. II. Rate of disappearance of the $NH_2(X^2B_1)$ radical. *J. Phys. Chem.* **75**, 2087 - 2093.

Hack, W., P. Rouveirolles, and H. G. Wagner 1986. Direct measurements of the reactions $NH_2 + H_2 = NH_3 + H$ at temperatures from 670 to 1000 K. *J. Phys. Chem.* **90**, 2505 - 2511.

Ham, D. O., D. W. Trainor, and F. Kaufman 1970. Gas phase kinetics of $H + H + H_2 \rightarrow 2H_2$. *J. Chem. Phys.* **53**, 4395 - 4396.

Hanel, R. A., B. J. Conrath, L. W. Herath, V. G. Kunde, and J. A. Pirraglia 1981. Albedo, internal heat, and energy balance of Jupiter: Preliminary results of the Voyager infrared investigation. *J. Geophys. Res.* **86**, 8705 - 8712.

Husain, D., and P. E. Norris 1977. Reactions of phosphorus atoms, $P(^{34}S_{3/2})$, studied by attenuation of atomic resonance radiation in the vacuum ultraviolet. *J. Chem. Soc. Faraday Trans.* 2. **73**, 1107 - 1115.

Kaye, J. A. and D. F. Strobel 1984. Phosphine photochemistry in the atmosphere of Saturn. *Icarus* **59**, 314 - 335.

Knacke, R. F., S. J. Kim, S. T. Ridgway, and A. T. Tokunaga 1982. The abundances of CH_4, CH_3D, NH_3, and PH_3 in the troposphere of Jupiter derived from high-resolution 1100 – 1200 cm^{-1} spectra. *Astrophys. J.* **262**, 388 - 395.

Ko, T., P. Marshall, and A. Fontijn 1990. Rate coefficients for the H + NH_3 reaction over a wide temperature range. *J. Phys. Chem.* **94**, 1401 - 1404.

Koshi, M., M. Yoshimura, K. Fukuda, and H. Matsui 1990. Reactions of $N(^4S)$ atoms with NO and H_2. *J. Chem. Phys.* **93**, 8703 - 8708.

Kunde, V., R. Hanel, W. Maguire, D. Gautier, J. Baluteau, A. Marten, A. Chedin, N. Husson, and N. Scott 1982. The tropospheric gas composition of Jupiter's north equatorial belt (NH_3, PH_3, CH_3D, GeH_4, H_2O) and the Jovian D/H isotopic ratio. *Astrophys. J.* **263**, 443 - 467.

Landry, B., M. Allen, and Y. L. Yung 1991. Troposphere-stratosphere interactions in a one-dimensional model of Jovian photochemistry. *Icarus* **89**, 377 - 383.

Larson, H. P., U. Fink, and R. R. Treffers 1977. Phosphine in Jupiter's atmosphere: The evidence from high-altitude observations at 5 micrometers. *Astrophys. J.* **211**, 972 - 979.

Lee, A. Y. T., Y. L. Yung, and J. Moses 2000. Photochemical modeling of CH_3 abundances in the outer solar system. *J. Geophys. Res.* In press.

Lee, J. H., J. V. Michael, W. A. Payne, D. A. Whystock, L. J. Stief 1976. Absolute rate constant for the reaction of atomic hydrogen with phosphine over the temperature range 209 to 495 K. *J. Chem. Phys.* **65**, 3280 – 3283.

Lellouch, E., F. Combess, and T. Encrenaz 1984. Microwave observations of Jupiter and Saturn. *Astron. Astrophys.* **140**, 216 - 219.

Leroy, G., M. Sana, and A. Tinant 1985. Etude theorique des reactions d'abstraction d'hydrogene RH + X = R + HX, avec R, X≡H, CH3, NH2, OH et F. *Can. J. Chem.* **63**, 1447 - 1456.

Levy, A., N. Lacome, and G. Tarrago 1994. Temperature-dependence of collision-broadened lines of phosphine. *J. Molec. Spectrosc.* **166**, 20 - 31.

Lewis, J. S. and R. G. Prinn 1970. Jupiter's clouds: Structure and compositions. *Science* **169**, 472 - 473.

Lindal, G. F., G. E. Wood, G. S. Levy, J. D. Anderson, D. N. Sweetnam, H. B. Hotz, V. R. Eshlemann, and G. L. Tyler 1981. The atmosphere of Jupiter: An analysis of the

Voyager radio occultation measurements. *J. Geophys. Res.* **86,** 8721 - 8727.

Massie, S. T. and D. M. Hunten 1982. Conversions of para and ortho hydrogen in the Jovian planets. *Icarus* **49**, 213 - 226.

Mayer, S. W., and L. Schieler 1966. Computed high-temperature rate constants for hydrogen-atom transfers involving light atoms. *J. Chem. Phys.* **45,** 385 - 391.

Moses, J. I., G. R. Gladstone, H. Feuchtgruber, and M. Allen 2000. Photochemistry of the upper atmosphere of Saturn. I. Hydrocarbon chemistry and comparisons with ISO observations. *Icarus*. **143,** 244 - 298.

Mount, G. H. and G. J. Rottman 1981. The solar irradiance 1200 – 3184 Å near solar maximum: July 15, 1980. *J. Geophys. Res.* **86,** 9193 - 9198.

Mulenko, S. A., 1987. The application of an intracavity laser spectroscopy method for elementary processes study in gas-phase reactions. *Rev. Roum. Phys.* **32**, 173 - 178.

Pagsberg, P. B., J. Eriksen, and H. C. Christensen 1979. Pulse radiolysis of gaseous ammonia-oxygen mixtures. *J. Phys. Chem.* **83,** 582 - 590.

Pickett, H. M., R. L. Poynter, and E. A. Cohen 1981. Pressure broadening of phosphine by hydrogen and helium. *J. Quant. Spectrosc. Radiat. Transfer* **26,** 197 - 198.

Prinn, R. G. and J. S. Lewis 1975. Phosphine on Jupiter and implications for the Great Red Spot. *Science* **190**, 274 - 276.

Ridgway S. T., L. Wallace, and G. R. Smith 1976. The 800 – 1200 inverse centimeter absorption spectrum of Jupiter. *Astrophys. J.* **207**, 1002 - 1006.

Roose, T. R., R. K. Hanson, and C. H. Kruger 1978. Decomposition of NO in the Presence of NH_3. *Symp. Int. Shock Tubes Waves Proc.* **11**, 245.

Serabyn, E. and E. W. Weisstein 1995. Fourier transform spectroscopy of the Orion molecular cloud core. *Astrophys. J.* **451**, 238 - 251.

Serabyn, E. and E. W. Weisstein 1996. Calibration of planetary brightness temperature spectra at near-millimeter and submillimeter wavelengths with a Fourier-transform spectrometer. *Appl. Opt.* **35**, 2752 - 2763.

Stief, L. J., and W. A. Payne 1976. Absolute rate parameter for the reaction of hydrogen

with hydrazine. *J. Chem. Phys.* **64**, 4892 - 4896.

Strobel D. F 1977. NH_3 and PH_3 photochemistry in the Jovian atmosphere. *Astrophys. J. Lett.* **214**, L97 – L99.

Tokunaga A. T., R. F. Knacke, S. T. Ridgway, and L. Wallace 1979. High-resolution spectra of Jupiter in the 744 – 980 inverse centimeter spectral range. *Astrophys. J.* **232**, 603 - 615.

Tomasko M. G 1974. Ammonia absorption relevant to the albedo Jupiter. II. Interpretation. *Astrophys. J.* **187**, 641 - 650.

Weisstein, E. W. and E. Serabyn 1994. Detection of the 267 GHz J=1-0 rotational transition of PH_3 in Saturn with a new Fourier transform spectroscopy. *Icarus* **109**, 367 - 381.

Weisstein, E. W. and E. Serabyn 1996. Submillimeter line search in Jupiter and Saturn. *Icarus* **123**, 23 - 36.

Chapter 5

Allen, M., Y. L. Yung, and G. R. Gladstone 1992. The relative abundance of ethane to acetylene in the Jovian stratosphere. *Icarus.* **100**, 527 - 533.

Andrews, D. G., J. R. Holton, and C. B. Leovy 1987. *Middle Atmospheric Dynamics*, pp. 371 – 375. Academic Press, Orlando.

Conrath, B. J., P. J. Gierasch, and S. S. Leroy 1990. Temperature and Circulation in the Stratosphere of the Outer Planets. *Icarus.* **83**, 255 – 281.

Dunkerton, T. 1978. On the Mean Meridional Mass Motions of the Stratosphere and Mesosphere. *J. Atmos. Sci.* **35**, 2325 – 2333.

Fernando, M, and J. Sedano 1997. Radiative Balance and Dynamics in the Stratosphere of Jupiter: Results from a Latitude-Dependent Aerosol Heating Model. *Icarus.* **130**, 36 – 48.

Friedson, A. J., R. A. West, A. K. Hronek, N. A. Larsen, and N. Dalal 1999. Transport and Mixing in Jupiter's Stratosphere Inferred from Comet S-L9 Dust Migration. *Icarus.* **138**, 141 – 156.

Gierasch, P. J., B. J. Conrath, and J. A. Magalhaes 1986. Zonal Mean Properties of Jupiter's Upper Troposphere from Voyager Infrared Observations. *Icarus.* **67**, 456 – 483.

Gladstone, G. R., M. Allen, and Y. L. Yung 1996. Hydrocarbon photochemistry in the upper atmosphere of Jupiter. *Icarus* **119**, 1 - 52.

Landry, B., M. Allen, and Y. L. Yung 1991. Troposphere-Stratosphere Interactions in a One-Dimensional Model of Jovian Photochemistry. *Icarus.* **89**, 377 – 383.

Moreno, F., and J. Sedano 1997. Radiative Balance and Dynamics in the Stratosphere of Jupiter: Results from a Latitude-Dependent Aerosol Heating Model. *Icarus.* **130**, 36 - 48.

Orton G. *et al.* 1994. Spatial Organization and Time Dependence of Jupiter's Tropospheric Temperatures. *Science.* **265**, 625 – 631.

Perry, J. R. *et al.* 1999. *J. Geophys. Res.* **104**, 16541.

Sada, P. V., G. L. Bjoraker, D. E. Jennings, G. H. McCabe, and P. N. Romani 1998, Observations of CH_4, C_2H_6, and C_2H_2 in the stratosphere of Jupiter, *Icarus,* **136**, 192-201.

West, R. A., and P. H. Smith 1991. Evidence for Aggregate Particles in the Atmospheres of Titan and Jupiter. *Icarus.* **90**, 330 - 333.

West, R. A., A. J. Friedson, and J. F. Appleby 1992. Jovian Large-Scale Stratospheric Circulation. *Icarus.* **100**, 245 - 259.

Wong, A. S., A. Y. T. Lee, Y. L. Yung, and J. M. Ajello 2000. Jupiter: Aerosol Chemistry in the Polar Atmosphere. *Astrophys. J.* **534**, L215 - L217.